



UNSW
A U S T R A L I A

Optimised 3D Deployment of Wi-Fi HaLow FANETs for Terrain-Constrained Search and Rescue

MMAN4953 Final report

Author: Lachlan Wallbridge
Student ID: z5359327
Supervisor: James Stevens

Abstract

In search and rescue operations, reliable communication is critical, yet current communication methods including handheld radios and deployable cellular systems are often limited by terrain, low-bandwidth, infrastructure loss, or range. This thesis investigates the use of Wi-Fi HaLow in Flying Ad Hoc Networks to extend communication coverage in such environments. Real ground-to-ground and ground-to-air measurements with Morse Micro HaLowLink kits are used to characterise real world links, providing calibration for a terrain-aware propagation and throughput model. This model is integrated into an NSGA-II multi-objective optimiser that uses digital elevation data to place UAV relays and evaluate multi-hop routes. Results show that small UAV fleets can provide multi-megabit coverage across rugged terrain with modest throughput–coverage trade offs.

¹contact email: z5359327@ad.unsw.edu.au

ORIGINALITY STATEMENT

'I hereby declare that this submission is my own work and to the best of my knowledge it contains no materials previously published or written by another person, or substantial proportions of material which have been accepted for the award of any other degree or diploma at UNSW or any other educational institution, except where due acknowledgement is made in the thesis. Any contribution made to the research by others, with whom I have worked at UNSW or elsewhere, is explicitly acknowledged in the thesis. I also declare that the intellectual content of this thesis is the product of my own work, except to the extent that assistance from others in the project's design and conception or in style, presentation and linguistic expression is acknowledged.'

Signed: Lachlan Wallbridge



Date: 21/11/2025

Contents

Nomenclature	vii
1 Introduction	1
2 Literature Review	3
2.1 Project Background	3
2.1.1 Overview of Disaster Relief Operations	3
2.1.2 Time Sensitive Nature of Disaster Response	3
2.1.3 Importance of Accessible Communication for First Responders	4
2.2 Current Methods of Communication and their Limitations	5
2.2.1 Current Communication Methods and Technology	5
2.3 Emerging Technology for Disaster Recovery and Search and Rescue Networks	7
2.3.1 Satellite Communication technologies	7
2.3.2 Air Deployed IoT Solutions	9
2.3.3 Unmanned Aerial Vehicles (UAV) Ad-hoc Networks	11
2.3.4 Single UAV Systems	12
2.3.5 Multi-UAV Networks	12
2.3.6 Multi UAV Network Topology Technologies	13
2.3.7 Multi UAV Deployment Algorithms	14
2.3.8 Multi UAV Mobility Models	15
2.3.9 Data Routing Schemes	16
2.3.10 Security and Regulatory Requirements	19
2.4 Network Technologies for Multi-media Data Transmission	20
2.4.1 LoRaWAN	20
2.4.2 Wi-Fi 802.11	21
2.5 Knowledge Gaps and Future Research Directions	24
2.5.1 Field Testing and real world Validation of Wi-Fi HaLow	24
2.5.2 Drone Deployment Algorithm Purpose Built for SAR	24
3 Methodology	25
3.1 Wi-Fi HaLow Testing Methodology	25
3.1.1 Purpose and Scope	25
3.1.2 Equipment and Configuration	26
3.1.3 Test Sites and Layout	27
3.1.4 Experimental Factors and Test Matrix	27
3.1.5 Procedures	27
3.1.6 Measurements and Data Recording	29
3.1.7 HaLowLink 1 Range-Test Tool	29
3.1.8 Controls, Safety, and Limitations	30
3.2 Algorithm Methodology	32
3.2.1 Node Definitions and Network Structure	32
3.2.2 Terrain Data Fetching from ELVIS Database	33
3.2.3 Signal Modelling	34

3.2.4	Wi-Fi HaLow Modelling	36
3.2.5	Optimisation Algorithm	42
3.2.6	Visualisation Overview	46
4	Results and Discussion	47
4.1	Wi-Fi HaLow Testing Results	47
4.1.1	Ground-to-Ground Testing	48
4.1.2	Drone interference at fixed range	54
4.1.3	Ground-to-air testing	55
4.2	Algorithm Results	61
4.2.1	Scenario configuration	61
4.2.2	Experimental Setup	61
4.2.3	NSGA-II Convergence Behaviour	61
4.2.4	Pareto Front and Trade-off Analysis	63
4.2.5	Representative Optimised Deployments	64
4.2.6	Stability across optimisation runs	65
4.3	Discussion and Implications for UAV relay design	66
5	Conclusion	68
6	Appendix	
6.1	Raw Testing Results : Longreef	
6.2	Raw Testing Results : Centennial	

List of Figures

1	Activity of post disaster response phases over time [76]	4
2	Susceptibility of Handheld Radio to line of sight changes [69]	5
3	Example incident report using the FireMapper dashboard [33]	6
4	Illustration of the possible use cases of the Dandelion Gyrochute [25]	9
5	Using a GPS + Wi-Fi payload to locate lost persons in national parks [26] . .	10
6	UAV deployed network within a disaster scenario [16]	11
7	UAV communication architectures a Single UAV system, b multi-UAV ad-hoc network, c multi-group ad-hoc network, d multi-layer adhoc network [16]	13
8	UAV mobility patterns [2]	16
9	Regional Centre nodes in post-disaster DTN environments [31]	17
10	Drone regulations in Australia by CASA [64]	19
11	Morse Micro 3km urban range test [59]	23
12	HaLowLink 1 range-test tool showing configuration and protocol selection. .	29
13	HaLowLink 1 range-test output showing example line-of-sight (LoS) test results.	30
14	System model overview of ground nodes (GN), UAVs, and BH(s) over a search area.	33
15	Spatial coverage of ELVIS (Elevation and Depth Information System) DEM data.	33
16	Illustration of LoS and Fresnel-zone evaluation between a UAV and ground node.	35
17	Provided MCS table showing modulation and coding scheme (MCS) index, corresponding PHY data rates, and empirically derived receiver sensitivities.	37
18	Shannon capacity and MCS-limited PHY ceilings for different channel widths.	39
19	Discrete MCS steps versus smoothed exponential ceiling \tilde{C}_{MCS}	41
20	Dynamic bandwidth selection showing active channel width versus RSSI. .	42
21	Example of interactive tooltips in the 3D visualisation, showing per-hop RSSI, PHY rate, and MCS details.	46
22	Status snapshot at short range, confirming configuration and noise floor. .	47
23	Ground-to-ground Wi-Fi HaLow range testing environment. (Left) Annotated map of test locations. (Right) Remote HaLow node setup at the highlighted remote point.	48
24	Measured spectrum from 900-952 MHz at the test site, showing the selected HaLow channel and weak narrowband interference around channel 32.	48
25	Measured noise floor along the Long Reef-Narrabeen test route.	49
26	RSSI versus PHY rate for all observed integer noise floors.	49
27	Measured local and remote RSSI versus range for the G2G tests, compared with the FSPL model and interference margin.	50
28	Fresnel-zone clearance ratio for the G2G tests with primary thresholds.	51
29	Measured UDP/TCP throughput and modelled PHY capacity versus RSSI for the G2G tests.	52
30	Measured UDP and TCP throughput versus range for the G2G tests.	53
31	Noise floor and RSSI measurements at 40 m for the three test configurations.	54
32	UDP and TCP throughput across the three configurations at 40 m.	55

33	Ground-to-air Wi-Fi HaLow range testing environment at Centennial Park. (Left) Annotated map of test locations. (Right) HaLowLink-1 node mounted on the airframe.	55
34	Measured noise floor at Centennial Park for the ground and drone HaLow nodes.	56
35	Measured local and remote RSSI versus range at Centennial Park.	57
36	Clearance ratio of first fresnel zone for G2G and G2A tests.	57
37	RSSI vs Bottlenecked throughput for G2G and G2A tests.	58
38	UDP and TCP Throughput vs Range for G2G and G2A tests.	59
39	MAC-layer round-trip success rate versus range for the G2G and G2A tests.	60
40	NSGA-II hypervolume convergence across 50 generations.	62
41	Objective convergence across generations: (a) throughput and (b) coverage..	63
42	Non-dominated solutions obtained by NSGA-II at the end of the optimisation.	64
43	Representative optimised UAV deployments selected from the non-dominated set for four different scenarios.	65
44	Overlay of Pareto fronts from repeated NSGA-II runs with different random seeds.	66
45	Long Reef G2G measurements: RSSI as a function of range.	
46	Long Reef G2G measurements: RSSI versus throughput.	
47	Long Reef G2G measurements: RSSI (bottleneck) versus throughput.	
48	Long Reef G2G measurements: UDP Throughput as a function of range. . .	
49	Long Reef G2G measurements: TCP Throughput as a function of range. . .	
50	Centennial Park G2A and G2G comparison: RSSI as a function of range. . .	
51	Centennial Park G2A and G2G comparison: RSSI versus throughput.	
52	Centennial Park G2A and G2G comparison: RSSI (bottleneck) versus throughput	
53	Centennial Park G2A and G2G comparison: UDP Throughput as a function of range	
54	Centennial Park G2A and G2G comparison: TCP Throughput as a function of range	

List of Tables

1	Wi-Fi HaLow test matrix.	27
2	Device and model parameters used in computation.	37
3	Description of Algorithm 1 steps.	44
4	NSGA-II configuration parameters.	45
6	Asymptotic time complexity for one NSGA-II generation.	45

List of Algorithms

1	Evaluator function <code>evaluate</code> for population X	43
---	---	----

Nomenclature

AGL Altitude Above Ground Level

BH Backhaul Node (gateway to external network)

DEM Digital Elevation Model

FANET Flying Ad hoc Network

G2A Ground-to-air link

G2G Ground-to-ground link

GN Ground Node (handheld or user device)

IoT Internet of Things

LoS Line of Sight

MAC Medium Access Control

MCS Modulation and Coding Scheme

NLoS Non Line of Sight

NSGA-II Non-dominated Sorting Genetic Algorithm II

PHY Physical layer

QoS Quality of Service

RSSI Received Signal Strength Indicator (dBm)

SAR Search and Rescue

SINR Signal-to-Interference-plus-Noise Ratio

SNR Signal-to-Noise Ratio

UAV Unmanned Aerial Vehicle

1 Introduction

Search and rescue (SAR) operations are critically dependent on the rapid exchange of information and robust communication systems, as these elements are vital for coordinating efforts and ensuring the safety of both victims and responders. Teams are often deployed into rugged or remote terrain where cellular coverage is poor, existing radio infrastructure is sparse, and damage from the incident can disrupt what little connectivity is available. In these conditions, responders must coordinate search tasks, share situational updates and request assistance. When communication links fail, search efficiency drops and the safety of both victims and responders can be affected.

Conventional methods, including handheld radios and cellular networks, often face significant challenges in non-urban settings due to terrain obstructions, line-of-sight limitations, and reliance on existing infrastructure, which can be sparse or damaged in remote areas. Radio links can be blocked by ridges, dense vegetation or canyon like environments, and base stations may be far from the search area or offline. While satellite communication can provide backhaul to the greater internet, it is still being developed and is currently prohibitive, requiring specialised equipment with setup times and stable, uninterrupted access to the sky. There is therefore, strong motivation to explore more flexible, rapidly deployable communication systems that can follow search teams into difficult terrain.

Unmanned aerial vehicles (UAVs) offer one such option. By flying at an appropriate altitude, UAVs can see over obstacles and provide line of sight paths between ground teams and a backhaul point. When several UAVs cooperate as a Flying Ad Hoc Network, or FANET, each vehicle can act as both a relay and a client, extending coverage across valleys and along trails. Existing FANET studies have explored various radio technologies and routing schemes, however, many rely on overly simplistic propagation models, focus on two-dimensional layouts, or utilise short-range Wi-Fi bands that struggle to penetrate dense terrain and foliage effectively.

Wi-Fi HaLow, based on the IEEE 802.11ah standard, is a promising alternative. Operating in the sub 1 GHz band, it is designed for long range, low power IoT applications. Compared with conventional 2.4 GHz and 5 GHz Wi-Fi, HaLow achieves better penetration through vegetation and obstacles, while still supporting IP based traffic and megabit per second data rates. Morse Micro's HaLow chipsets and HaLowLink evaluation kits demonstrate that these links can reach several kilometres in favourable conditions, and support mesh style operation that fits naturally with UAV relay networks. However, there is limited published work on how HaLow behaves in mixed ground to ground and ground to air scenarios, and how a HaLow based FANET should be placed over real terrain for SAR use.

Two main gaps follow from this. First, there is a need for field measurements of Wi-Fi HaLow links in realistic environments that resemble SAR scenarios and capture metrics such as range, signal strength, environmental interference and platform specific penalties such as interference from drone avionics. Second, there is a lack of optimisation al-

gorithms that operate using terrain data and can account for LoS, foliage loss and multi-hop.

This thesis addresses these gaps by combining experimental measurements with a terrain aware optimisation framework. The first part of the work performs controlled Wi-Fi HaLow tests using Morse Micro HaLowLink 1 kits. Ground to ground trials along the Long Reef to Narrabeen coastline measure range, RSSI, noise and throughput in a predominantly clear line of sight environment. Additional tests investigate interference from co located telemetry radios and the effect of mounting HaLow on a multi rotor UAV. Ground to air trials at Centennial Park are used to compare aerial links against ground baselines at the same site, highlighting airborne noise penalties and platform specific effects.

The second part of the work develops a propagation and throughput model that extends free space loss with Fresnel clearance, knife-edge diffraction, vegetation loss and calibrated HaLow link behaviour. The model uses measured noise floors and an empirically tuned mapping from the modulation and coding scheme to the effective data rate. This model is applied to a high resolution digital elevation model of the Katoomba region, which represents a realistic SAR environment with steep valleys, ridge lines and walking tracks.

Using this radio model and terrain data, a multi objective UAV placement algorithm is built around the NSGA-II evolutionary optimiser. Candidate solutions specify the three dimensional positions of UAV relays that connect a fixed backhaul point to multiple ground nodes representing responders. Each solution is evaluated for coverage, based on whether a ground node has a feasible route to the backhaul, and for average end to end throughput along the resulting multi hop paths. NSGA-II is then used to explore the trade off between maximising coverage and maximising throughput, producing a Pareto front of non dominated solutions and representative deployment layouts.

The central aim of the project is to evaluate the operational limits of Wi-Fi HaLow links under realistic conditions and to determine optimal positioning strategies for a small fleet of HaLow-equipped UAVs to enhance SAR team communication in difficult environments. The key contributions of this work are the characterisation of HaLow performance for both ground and aerial links, a calibrated terrain aware propagation and throughput model, and a deployment framework that uses NSGA-II to design FANET configurations over real terrain.

The remainder of this report is organised as follows. Chapter 2 provides background information on disaster response, current SAR communication methods, UAV networks and Wi-Fi HaLow, and identifies the main knowledge gaps that motivate this work. Chapter 3 describes the experimental methodology, signal and throughput modelling, and the NSGA-II based optimisation framework. Chapter 4 presents the Wi-Fi HaLow test results and the optimisation outcomes, and discusses their implications for UAV relay design. Chapter 5 concludes the thesis and outlines directions for future work.

2 Literature Review

2.1 Project Background

2.1.1 Overview of Disaster Relief Operations

Disaster relief operations are critical emergency responses designed to mitigate harm, assist affected populations, and recover individuals in distress. These operations cover a wide range of environments and disaster types, including natural disasters (earthquakes, floods, wildfires, and cyclones), technological accidents, and humanitarian crises. The effectiveness of such efforts relies on speed of the response, the use of assistive technologies and coordination between multiple agencies.

One of the primary challenges in disaster relief and Search and Rescue (SAR) operations is the vast and often inaccessible geography of affected areas. In remote terrain, limited network infrastructure and rugged environmental conditions can hinder communication and movement of search teams [46]. In addition, large scale disasters can cause widespread destruction of critical infrastructure including roads, power grids, and telecommunication networks, further complicating relief and search efforts [67].

It is estimated by the United Nations Office for Disaster Risk Reduction [1] that over the past 20 years, a recorded 7348 disasters claimed the lives of 1.23 million people worldwide, and effecting over 4 billion people. These events resulted in an accumulative cost of approximately \$2.97 trillion in economic losses. This is in contrast to the 1.19 million deaths, 3.25 billion affected and \$1.63 trillion in losses in the two decades prior [1]. In particular, the uptick in the number of major floods has more than doubled, from 1389 to 3254, with storms following a similar trend rising from 1457 to 2034 [1]. The United Nations Office additionally notes a recorded increase in other categories including wildfires, drought and extreme temperature events. With marked increases each decade, governments globally have increased their focus on post disaster initiatives [67, 76].

2.1.2 Time Sensitive Nature of Disaster Response

The time sensitive nature of disaster response presents a critical challenge for emergency personnel. The probability of survival decreases rapidly after events such as building collapses or flooding, necessitating efficient, effective and timely resource deployment [63, 67, 76].

Search and Rescue (SAR) teams are among the first responders in disaster scenarios, responsible for rapid situation assessment, risk evaluation, and the location and extraction of survivors. The prompt deployment of SAR teams, along with supporting rescue vehicles and technologies, is critical, as survival chances diminish significantly over time. SAR operations often involve collaboration between emergency services, government agencies, and volunteer organisations to maximise response efficiency [76]. Figure 1 shows the estimated activity level of post disaster response initiatives over time, highlighting the short but high activity

emergency phase that is typically followed by prolonged periods of restoration and recovery.

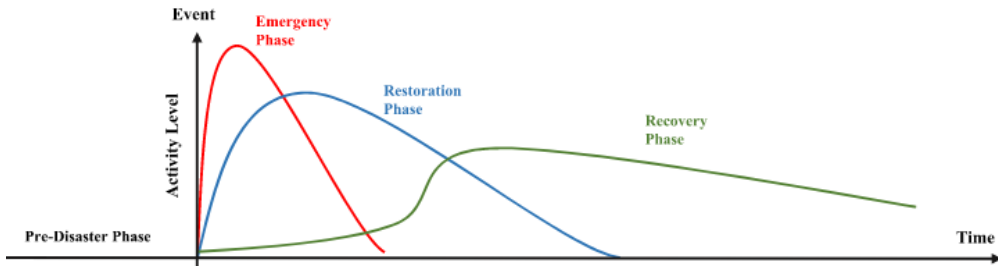


Figure 1: Activity of post disaster response phases over time [76]

Traditional SAR methods methods are highly dependent on human teams, trained canines, and aerial reconnaissance, which may be constrained by environmental conditions, visibility limitations, network access and the availability of trained personnel [57].

2.1.3 Importance of Accessible Communication for First Responders

Coordination and communication are fundamental challenges in disaster relief efforts. Response teams often operate in areas with poor or no cellular coverage, making it difficult to relay information and coordinate relief efforts effectively [3, 46]. In Australia, the average time of restoration for fault affected services is 83 hours, and can last up to 125 hours according to the 2017-2018 ACMA Communications Report [11]. A lack of infrastructure can stem from various factors, including damages from the natural disaster, system overloading, challenging geographical features such as mountains or dense vegetation, or the inherent remoteness of rural locations [3, 92].

A high data rate communication network is essential for enabling real time coordination among response teams, enabling communication with dispatch centres, and facilitating the exchange of mission critical data [3, 23]. Within response teams, the ability to share situational updates, hazard assessments, and logistical requirements without delay is a key requirement of the chosen communication medium. Similarly, communication with off site dispatchers is important as it allows for better resource allocation, operational oversight, and emergency response adjustments depending on the overarching response environment [23]. High bandwidth networks are also key in enabling internet dependent disaster response tools such as AI victim detection and computer vision algorithms [68].

Network availability and consistency are important for ensuring uninterrupted operations. A communication system supporting first responders must aim for near perfect up time when deployed and provide consistent data rates exceeding 1 Mbps to accommodate the transmission of mission critical updates. Partners in emergency services have provided us with the above minimum requirements.

2.2 Current Methods of Communication and their Limitations

2.2.1 Current Communication Methods and Technology

Digital Radio

Within regional search and rescue teams, the primary technology for communication between search ground are 5-8 W dual band 2-way radios [52, 95]. This form of communication is limited by two key factors, the range of the signal and the line of sight between users. The range is largely influenced by the transmitter's output power, operating frequency and its antenna configuration [95]. This includes antenna size, placement and modulation technology. Line of sight is effected by the terrain between the users, including obstacles such as vegetation and mountains. Signal propagation through and around terrain is highly dependent on frequency, with lower frequency signals offering better penetration due to their longer wavelengths [95].

Radio technology is used both within search groups via hand held radio units and between search clusters through larger antenna setups. Within search groups, distances between personal is relatively low. Handheld radio provides accessible and consistent verbal communication at small to medium ranges thanks to the smaller antenna being light in weight, low power and deployed in a small form factor [95]. These factors do however mean that signals from the hand held radio don't propagate far and are particularly susceptible to line of sight changes caused by elevation differences or vegetation [52] Figure 2.

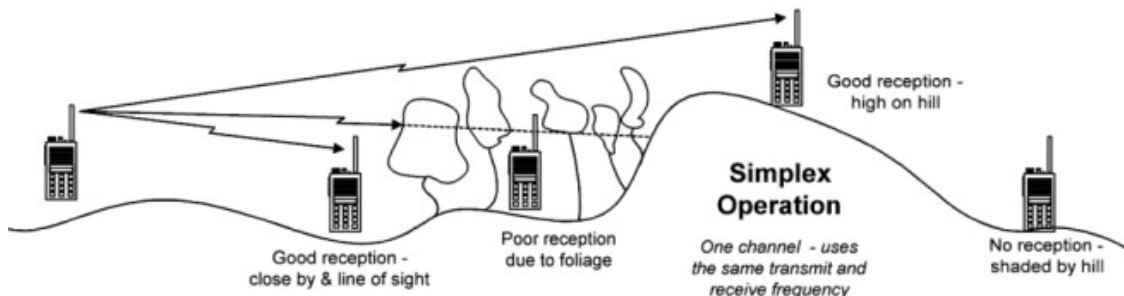


Figure 2: Susceptibility of Handheld Radio to line of sight changes [69]

For communication between search clusters, large antenna modules are deployed. These facilitate the sharing of important information between the search groups and the base station. This is key in requesting additional resources, medical aid, details relative to the victims status or emergency evacuation [52]. Pre-departure planning is crucial to this form of communication as teams need to determine communication windows such that they only need to setup the antenna when needed. Optimal setup factors include selecting a favourable geographical location, typically at higher elevations with minimal vegetation, to maximise communication range [95]. The required up time of the radio band and the setup time are also considered. The larger antenna are also heavy to carry and as such are typically only carried by one person per cluster.

Mobile Devices and Cellular Networks

Mobile devices play a critical role in search and rescue and disaster response efforts. They serve a dual purpose, in aiding emergency responders in coordination and data collection while also providing affected individuals a way to alert first responders of their situation. The widespread availability and ease of use of mobile devices make them a valuable tool in the current age of emergency response [3].

Modern disaster response efforts rely on the ability to upload images, findings, and event reports in real time. Incidents collected by first responders are collated into centralised monitoring applications, allowing dispatchers to interpret critical information and alert ground teams accordingly. Figure 3 shows the FireMapper application for a example incident.

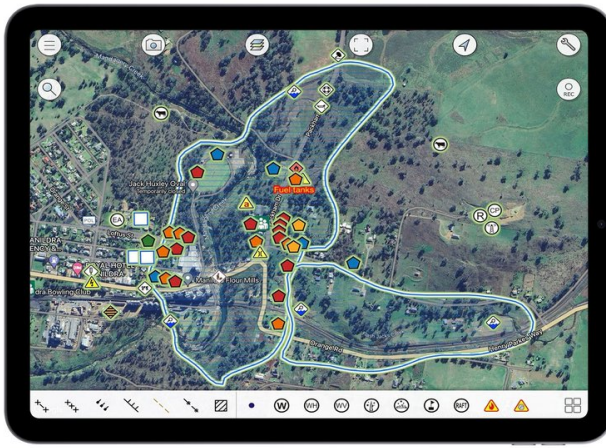


Figure 3: Example incident report using the FireMapper dashboard [33]

One of the key advantages of mobile technology is its accessibility, allowing volunteers to contribute to SAR efforts. With minimal setup, trained volunteers can use their devices to report incidents using mobile apps and share location data for coordination. This democratisation of SAR capabilities increases the number of available responders, supplementing official emergency efforts with community driven support.

The mobile communication approach does however, have a major drawback. In situations where cell coverage is unavailable due to infrastructure damage, power outages or network congestion, it may not be possible for responders to use these services. This results in emergencies being delayed in their reporting, and time critical situations potentially being missed [3, 95].

This is an issue identified by the New South Wales government, who recently committed \$5 million AUD on deployable post-disaster Wi-Fi coverage, known as satellite Cells on Wheels (CoW). [28]. The new COW units, which connect to the internet by satellite, provide free public Wi-Fi access to the area affected. Each tower is self powered (solar), providing Wi-Fi coverage up to 500 meters away, and can be linked to create a larger mesh based network [28]. This internet access will be key in supporting communities within the Restoration phase

identified in Figure 1, but may provide less value in rural search and rescue and immediate disaster response situations due to the limited signal range and required road infrastructure to set up.

2.3 Emerging Technology for Disaster Recovery and Search and Rescue Networks

2.3.1 Satellite Communication technologies

Satellite communication technology has been a significant area of study in recent years, with a focus on providing remote access to networks in the absence of critical infrastructure. This technology is found in various implementations, including satellite SIMs for mobile phones [84], compact satellite-to-ground receivers like the Starlink Mini [85], and larger deployable satellite towers [28].

A common requirement of these technologies is the need for a clear view of the sky [95] as they rely on satellite internet constellations to facilitate communication. This means that in areas of thick vegetation or notable elevation differences, such as forests and gullies, these technologies are unable to obtain stable connections. Additionally, factors such as signal latency, network congestion, and atmospheric interference also determine the performance of these systems, and must be considered when integrating them into emergency response frameworks.

Satellite SIM Technology

Satellite SIM technology is designed to provide direct-to-cellphone connectivity, eliminating the need for ground based cell towers. This approach extends mobile network coverage globally, particularly in remote and under served areas [84].

AST SpaceMobile's satellite SIM technology is compatible with existing 4G and 5G smartphones, requiring no specialised hardware. It functions as a space based cell tower rather than a broadband network like Starlink, targeting mobile users with direct to device service and enabling connectivity where traditional cell towers are unavailable. The system is supported by the BlueBird satellite constellation, which operates in Low Earth Orbit (LEO) and utilises large phased array antennas to direct the signal towards ground users. Tests in 2023 and 2024 have shown download speeds of 10 Mbps (4G) and 20 Mbps (5G) respectively [22]. The next generation of satellites, BlueBird Block 2 will deliver up to 10 times the bandwidth of the current constellation and supports transfer speeds of up to 120 Mbps over the 5G protocol [22, 84]. Unfortunately, the coverage for AST is still sparse due to the small number of satellites, however will be iteratively improved as more are launched.

Search and Rescue and Disaster Relief Benefits: The main benefit of this technology for SAR is the direct to phone service for responders, eliminating the need for additional hardware such as radio kits and antenna. This is a significant benefit as it removes the setup time required in traditional communication methods and reduces the weight carried

by first responders.

This technology is also beneficial to the affected community or individuals, as it is possible to deploy these virtual SIMs to people in the affected area for the duration of the disaster event. Personnel in the area will receive a text on their phone, allowing them to join the network given they are within range of the satellite [83]. A large draw of this technology is its ability to be deployed instantly, making particularly valuable to the time critical nature of SAR and disaster response.

Broadband Coverage (Starlink)

Starlink has the capability to provide broadband internet access to remote and under serviced areas, offering high speed, low latency connectivity. Unlike AST SpaceMobile's direct to phone service, Starlink requires a dedicated terminal to receive signals.

Starlink delivers broadband internet access for homes, businesses, vehicles, and emergency response teams. The service provides high speed, low latency connectivity, even in motion, making it particularly suitable for rescue vehicles, boats, and aircraft. The system is focused on internet connectivity over traditional mobile network services. Starlink's flagship product, the Starlink Mini, offers speeds of up to 100 Mbps [85]. This is useful in scenarios where high bandwidth communication such as media transfer and data streaming is required.

The Starlink Mini also includes a built in Wi-Fi router where users can connect like any other Wi-Fi network. The range of this router however, is limited to $112m^2$ [85] limiting the use cases of the product. A benefit of the Starlink Mini is the low DC power consumption of the device. This makes it possible to deploy using batteries which is essential in response scenarios without power infrastructure.

A further benefit of the Starlink constellations is the use of thousands of small satellites compared to the 5 larger BlueBird satellites used by AST (as of April 2025). This results in higher, more consistent coverage than the AST service and is a key factor in assessing the feasibility of satellite communications for SAR and disaster relief purposes.

Search and Rescue and Disaster Relief Benefits: Starlink provides reliable internet access for both field teams and command centres, making it well suited for tasks that require consistent connectivity, such as video streaming, mapping, and remote operations. However, it does require a dedicated Starlink terminal, which adds to the hardware burden for responders. A major drawback Starlink terminals is that they don't offer continuous up time for ground teams as the terminal must be set up each time communication is needed, and allowed enough time to establish strong up links.

The ability to deploy mobile Starlink responders in vehicles is a major benefit of this system, as it provides stable, high bandwidth connections to vehicle based rescue operations, such as by boat or car. This technology also enables high bandwidth reliant rescue technologies, such as computer vision search algorithms and monitoring [68].

2.3.2 Air Deployed IoT Solutions

Deployable Internet of Things (IoT) solutions are designed to rapidly establish communication networks in areas lacking infrastructure and be self sufficient in their deployment and operation. These solutions are particularly valuable in emergency response and remote operations, where traditional methods of network deployment such as Communication on Wheels (CoWs) [28] are impractical or too slow to deploy due to environmental constraints.

The Dandelions' Gyrochute is an example of a deployable IoT platform, capable of autonomously delivering communication nodes via air deployment. Unlike conventional mobile base stations or ground based solutions, the Gyrochute is deployed above a location and leverages autorotation for a controlled descent to the ground. The Gyrochute can be equipped with payloads such as Wi-Fi access points, UHF radio repeaters, or sensor nodes for environment monitoring. Once deployed, these systems operate independently through solar power and smart energy management [24].

Expanding Radio Infrastructure

During emergency situations, existing communication infrastructure is often compromised, leaving first responders and communities without reliable means of communication. Deployable IoT solutions address this issue by delivering on demand radio infrastructure to establish communication channels where they are most needed [24].



Figure 4: Illustration of the possible use cases of the Dandelion Gyrochute [25]

One of the primary applications is the deployment of UHF radio repeaters, which extend the range of current radio communication methods used by emergency services [24, 25]. The coverage area can be increased through the deployment of more devices. Figure 4 demonstrates potential use cases of the solution in SAR and bushfire response, in which the Gyrochute is able to extend networks by acting as an intermediary point. This increases communication range between responders (right) or allows connection to a backhaul point such as a cell tower (left).

Cell and Wi-Fi capabilities

Beyond radio communications, the deployable solutions can also serve as a rapidly deployable digital communication hubs, enabling Wi-Fi and cellular connectivity in remote or disaster affected areas. By integrating satellite back haul, these devices provide high speed internet access independent of terrestrial infrastructure [24].

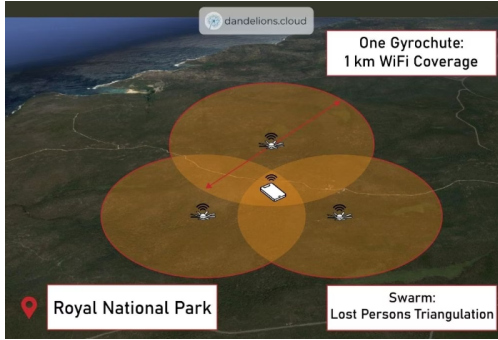


Figure 5: Using a GPS + Wi-Fi payload to locate lost persons in national parks [26]

One application is assisting lost individuals by creating Wi-Fi networks in their vicinity. When a lost person's phone detects a deployed signal, it can display a notification, even if the person is not actively connected. This provides individuals with a way to signal for help over the network. Figure 5 also outlines how multiple nodes can be deployed in order to triangulate the lost person's exact location [26].

IoT Capabilities

Beyond communications, IoT capabilities can support a wide array of sensor driven applications. Environmental monitoring payloads can collect and relay real time data on weather conditions, air quality, and fire activity. These IoT sensors enhance situational awareness, providing first responders with actionable intelligence to manage ongoing threats [24].

Challenges with Air Deployment

While air deployed IoT solutions provide rapid and flexible communication infrastructure, they also have limitations that can affect their performance and deployment feasibility.

- **Signal Propagation and Environmental Obstructions:** Like other deployed communication solutions, the air deployed methods are also affected by environmental factors such as dense vegetation, terrain elevation changes, and atmospheric conditions when landing. These obstructions can lead to lower throughput, signal attenuation, and inconsistent connectivity, particularly in forested or mountainous regions where line of sight is obstructed [95].
- **Landing Constraints:** Successful deployment of air base IOT solutions require suitable terrain for landing. Dense forests, steep slopes, or rocky surfaces may prevent proper placement, leading to misalignment of antennas or physical damage to the payload. Ideally, deployment should be conducted over open areas to maximise effectiveness.

- **Limited Power Availability in Extended Operations:** Although designed to be self sufficient with solar powered energy management, extended periods of poor weather or reduced sunlight exposure may limit its operational lifespan. In such cases, supplementary power sources or periodic maintenance may be required to sustain long term functionality.
- **Deployment Precision and Drift:** External factors such as wind conditions and altitude at deployment can impact the accuracy of placement. While methods are used for controlling descent, strong crosswinds or turbulent conditions may cause unintended drift, requiring careful pre-deployment planning to ensure accurate positioning.
- **Interference and Network Congestion:** In high demand scenarios, multiple deployed units operating on similar frequencies can lead to network congestion or interference. Pre-planning landing locations and dynamic channel switching would be necessary to ensure stable connectivity across multiple nodes within the same area [24].

2.3.3 Unmanned Aerial Vehicles (UAV) Ad-hoc Networks

With rapid advances in wireless technology, UAVs have been proposed as flexible, mobile nodes in airborne networks. This technology, called a Flying Ad-hoc Network (FANET), has been proposed as a dynamic solution for environments where network infrastructure is either unavailable or inoperative [16]. FANETs are formed dynamically and autonomously, enabling UAVs to establish and maintain communication links under varying conditions, as illustrated in Figure 6.



Figure 6: UAV deployed network within a disaster scenario [16]

Though both ad-hoc UAV networks and Internet of Things (IoT) systems operate around the idea of collaborative wireless networking, they differ in design principles and intended applications [16]. IoT networks typically consist of static or semi-static sensor nodes, such as those used by Dandelions Gyrocopter [24] explored previously, that communicate via structured and often centralised architectures. This means that nodes usually send data to a central gateway or server in a planned and organised way, relying on that central point to manage communication and processing. In contrast, ad-hoc UAV networks focus on the establishment of temporary, self organising links among mobile nodes and operate without the need for a central hub. The flexibility, reusability and rapid deployment of the UAV networks makes them especially advantageous in disaster response, and search and rescue operations [16].

2.3.4 Single UAV Systems

Single UAV systems involve the use of individual drones that operate independently rather than as part of a coordinated group. While multiple UAVs might be deployed at once, each one acts as a standalone unit and is directly controlled by a ground control station (GCS), as shown in Figure 7a. The range of each UAV is limited by how far it can reliably communicate with the GCS, which acts as the central point for issuing commands and managing the mission. This setup allows for greater control over each drone, making it especially useful for tasks that require targeted actions or isolated operations, such as servicing a specific area with a network connection [68], or acting as a link to extend an existing communication network.

However, from the perspective of disaster recovery and search and rescue networks, single UAV systems face major limitations due to their dependence on a fixed ground station. The key constraints are range and line of sight (LoS). UAVs can only operate within a certain distance from the GCS, and obstacles such as mountains or dense tree cover can severely degrade signal quality, restricting their effectiveness in difficult terrains [52].

A 2021 study [52] demonstrates how a Single UAV network solution can be used to restore and maintain radio communications during SAR operations by acting as airborne relays. By using UAVs equipped with radio repeater modules, the team was able to significantly extend communication range and improve reliability for ground personnel. This highlights the value of flexible deployment in bridging connectivity gaps, particularly in remote or obstructed environments.

2.3.5 Multi-UAV Networks

Multi-UAV networks represent an advancement in autonomous aerial systems, enabling cooperative behaviour among multiple unmanned aerial vehicles. Unlike single UAV deployments, which are often limited by line of sight, communication range, and processing capacity, multi-UAV systems benefit from scalability, redundancy, and improved spatial coverage [16].

The deployment of multi-UAV networks do present challenges related to communication reliability, topology management, drone deployment and mobility, signal routing, energy efficiency, and network security [16]. These systems must adapt to changing link conditions, intermittent connectivity, and constraints imposed by the UAVs' limited onboard resources. As such, the design of networking protocols and coordination strategies remains an active area of research and development.

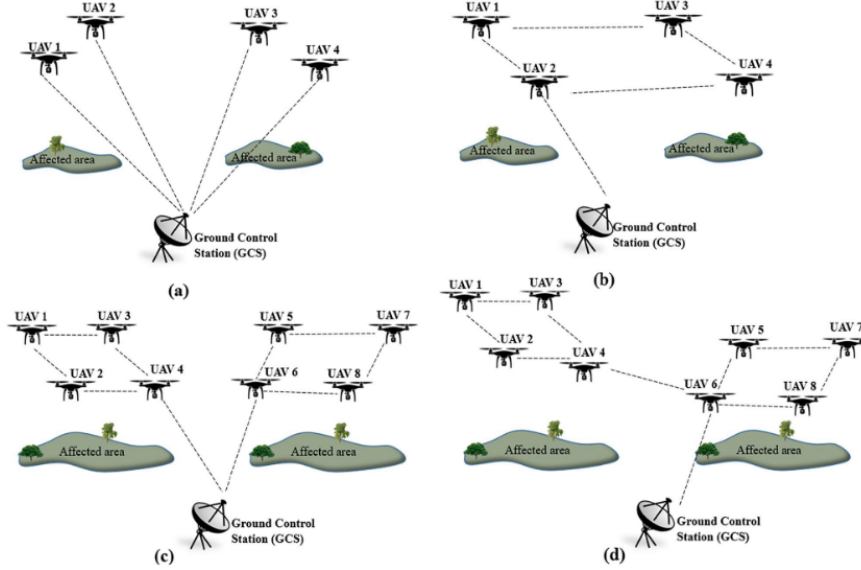


Figure 7: UAV communication architectures **a** Single UAV system, **b** multi-UAV ad-hoc network, **c** multi-group ad-hoc network, **d** multi-layer adhoc network [16]

2.3.6 Multi UAV Network Topology Technologies

Network topology refers to the way UAVs are organised and connected to communicate with each other. The choice of topology impacts the network's properties, such as its reliability, scalability, resilience to failure, and ability to adapt to dynamic environments. Figure 7 outlines the prominent multi-UAV topologies explored for disaster response contexts, each with its own notable strengths and weaknesses. These are multi-star, mesh, hierarchical mesh and cluster mesh architectures [32].

- **Multi-Star Topology:** In this structure, each UAV connects to a central node within its group, and select central nodes maintain links to a ground station. While this improves scalability compared to single UAV systems, it introduces communication bottlenecks and potential single points of failure at the central nodes. This approach is common in simple drone clusters but is less suited to dynamic disaster environments, where maintaining continuous communication is critical [16].
- **Mesh Topology (Figure 7.b):** UAVs communicate in a fully interconnected or partially connected mesh, relaying data through neighbouring nodes. This topology offers high resilience due to its self forming capabilities. Mesh networks support dynamic re-configuration as UAVs move or exit the network, making them ideal for rapidly changing disaster conditions. Several studies have implemented mesh networks for disaster communication, demonstrating improvements in network coverage and availability [29, 34, 32].
- **Hierarchical Mesh Topology:** Hierarchical mesh networks arrange UAVs in layered tiers, where each tier plays a specific role in communication and coordination. Higher level UAVs are equipped with more advanced processing and communication capabilities

and act as coordinators or relay nodes, overseeing lower tier activities and handling command distribution, data aggregation, and mission oversight [16].

This structured hierarchy enhances mission organisation, supports clear task delegation, and scales to large fleets by reducing congestion through controlled data flows. Studies such as [15, 18] demonstrate the benefits of hierarchical trees and group based formation control, showing how these systems enable efficient coordination among multiple UAV groups with less communication overhead.

A further advantage is the ability to extend communication range through multi tiered network pathways, making this topology suitable for wide area disaster networking and coordinated response efforts [16]. However, the architecture is complex to deploy and manage, often requiring additional UAVs as coordinators, relays, or cluster heads, which can be restrictive in rapid deployment scenarios and excessive for smaller scale SAR operations where simpler topologies are more practical.

- **Clustered Mesh Topology:** In a clustered mesh topology, UAVs are grouped into semi autonomous clusters, each managed by a cluster head that coordinates communication, distributes tasks locally, and manages resource allocation, while gateway UAVs handle inter cluster communication so that not all nodes must communicate directly [16].

This approach reduces communication complexity and energy consumption, as only select UAVs handle long range or high load communication tasks. Clustered mesh networks are particularly suitable for localised missions, such as providing internet access to smaller search and rescue clusters, as the structure mimics how these teams operate. The system's flexibility allows it to adapt to varying mission scopes, including multiple search areas or geographic challenges like mountain ridges, as shown in [13, 45].

However, reliance on designated cluster heads and gateway UAVs introduces single points of failure and increases hardware demands, and the initial setup and coordination of clusters is complex. These factors make clustered meshes less ideal for time critical missions and rapid response scenarios requiring immediate launch and action.

2.3.7 Multi UAV Deployment Algorithms

Effective UAV deployment is crucial in disaster scenarios to ensure optimal ground coverage and reliable communication pathways. Numerous strategies have been proposed to address challenges related to altitude selection, placement optimisation, modelling real world constraints such as obstacles, and limited information about terrain and user distribution.

Early approaches have focused on altitude optimisation to maximise radio coverage [39], and efficient placement based on circle packing theory to determine UAV positions based on fleet size [62]. Deployment has also been approached as a two dimensional problem using geometric methods such as the smallest enclosing circle and circle placement problems [6]. The derivation of optimal UAV density functions has also be attempted, using average path loss calculations to maximise ground node coverage [30].

Many existing models operate under 2D assumptions with fixed altitude and communication range, limiting their ability to adapt to complex environments. More recent research is moving towards 3D deployment strategies, which jointly consider horizontal and vertical positioning to improve coverage and signal quality [72]. These 3D approaches introduce more realistic constraints such as LoS/NLoS conditions, transmission power limitations, and energy efficiency [14], yet remain relatively underdeveloped compared to 2D frameworks.

To further enhance deployment performance, adaptive and intelligent algorithms have been proposed. Centralised and distributed control schemes [99], spiral coverage paths [49], and deep reinforcement learning techniques [48] have shown promise in maximising long-term communication coverage. However, many of these are being conducted under 2D assumptions and often overlook real world environmental conditions.

Recent trends include metaheuristic-based multi-objective optimisation algorithms such as MOPSO, NSGA-II, SPEA2, and PESA-II [36], which balance conflicting goals like user coverage, transmission quality, UAV quantity, and energy consumption. Studies have also considered mission specific objectives, such as minimising the number of UAVs while maintaining coverage and data rates [72], minimising maximum task time across UAVs [87], and optimising deployments for cost effectiveness, altitude, and communication quality [14, 50, 65]. These efforts represent a growing move toward realistic, flexible deployment models that can respond to the dynamic conditions typical in disaster affected areas.

2.3.8 Multi UAV Mobility Models

While UAV deployment refers to the initial placement and arrangement of drones, mobility models govern how UAVs move during operation. These models define the behaviour of UAVs post deployment, including real time adjustments in altitude, position, and orientation to maintain communication, avoid obstacles, or respond to changes in the environment. In the context of search and rescue (SAR) and disaster recovery, mobility is essential for sustaining network connectivity, tracking moving ground teams, and adapting to LoS changes.

The performance of UAV ad-hoc networks is strongly influenced by the underlying mobility model [16]. Conventional models used in Mobile Ad-hoc Networks (MANETs) such as the Random Waypoint, Random Walk, and Random Direction models shown in Figure 8a fail to capture the unique dynamics of aerial networks in disaster scenarios [98]. These models often produce unrealistic motion patterns, poor spatial distribution, or overlook 3D considerations unique to UAVs.

As a result, alternative UAV specific mobility models have been developed. As shown in Figure 8b, the Semi-Random Circular Movement (SRCM) model [93] allows drones to follow curved paths while hovering at designated locations, resulting in a more uniform node distribution. This model is particularly important for missions requiring consistent coverage over a specific area, as it provides better Quality of Service (QoS) to ground responders.



(a) UAV mobility patterns: (a) WayPoint; (b) Stay-At; (c) scan; (d) eight and (e) oval

Figure 8: UAV mobility patterns [2]

To improve environmental awareness, a 3D extension of SRCM termed 3DSRCM was proposed, incorporating orbit switching, pheromone guided tracking, and trajectory smoothing to reduce collision risks and improve scanning performance [54]. In comparison, the distributed mobility model discussed in [53] uses the UAVs' energy levels, area coverage, and connectivity to guide its flight path. By including these criteria into the decision model, this approach enables more efficient path planning and dynamic coordination, improving flight times and network performance.

In comparison, mobility models based on survivor or responder movement have been explored. Since SAR personnel do not move randomly but instead follow paths shaped by terrain, debris, and objectives, traditional models are inefficient [77]. The Disaster Area (DA) model [8] attempts to simulate human movement by dividing the mission space into sub-zones (e.g., hospital, command centre, search area), but still relies on random way point behaviour in key regions. More advanced options like the Composite Mobility (CoM) model [66] combine group dynamics with obstacle aware navigation using geographic maps and Dijkstra's algorithm, though they require accurate pre-disaster mapping. The Human Behaviour for Disaster Areas (HBDA) model [20] addresses these limitations by using force vectors to simulate human search patterns, aiming for high coverage and reduced search time.

Despite ongoing improvements, many models still simplify movement into two dimensions. Efforts to extend SAR mobility into 3D space have introduced new models that account for varying environments [91]. These frameworks aim to reflect real world responder behaviour, improving UAV coordination, network resilience, and situational awareness.

2.3.9 Data Routing Schemes

Reliable data routing is a fundamental challenge in multi-UAV networks, particularly in dynamic and intermittently connected contexts such as SAR. UAVs must coordinate to maintain data flow between nodes, frequently acting as relays to extend the communication range between peers or to a base station. The mobility of UAVs, changing topology, energy constraints and link instability render traditional Mobile Ad Hoc Network (MANET) routing protocols unsuitable for these scenarios, due to their high overhead and convergence time [7].

To address these limitations, many routing paradigms have been designed to suit the unique properties of UAV networks and utilise factors including their mobility patterns and internal access to GPS. These protocols are generally classified into four major categories: Reactive, Opportunistic, Delay Tolerant Networks (DTN), and Wireless Mesh Networks (WMN) [16].

- **Reactive Routing Protocols** establish routes only when needed, reducing control overhead at the expense of initial delay. Protocols such as Ad-hoc On-demand Distance Vector (AODV), Location Aided Routing (LAR), Temporally Ordered Routing Algorithm (TORA), and Associativity Based Routing (ABR) fall into this category [16]. While efficient in static or moderately mobile networks, their convergence time becomes a bottleneck in fast changing UAV topologies [7].
- **Opportunistic Routing Protocols** exploit the broadcast nature of wireless communication, using mobility induced communication windows to forward packets. Protocols such as Opportunistic Routing Protocol (ORP), Multi-copy Opportunistic Routing (MCOR), Cooperative Communication Based Opportunistic Routing (CCOR), Geographic and Opportunistic Routing (GEAR), and Spray and Wait (SnW) fall into this category and utilise brief encounters between UAVs to forward data [16]. These protocols use packet replication to enhance delivery success, however this results in increased bandwidth consumption and buffer usage [10].

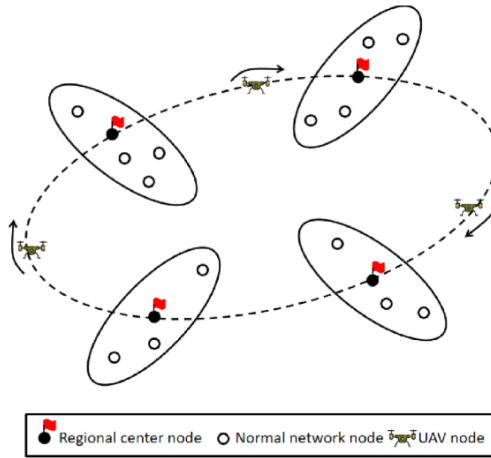


Figure 9: Regional Centre nodes in post-disaster DTN environments [31]

- **Delay Tolerant Network (DTN) Routing Protocols** DTNs use a store–carry–forward approach, where nodes hold messages during disconnection and forward them once a link becomes available. This makes them well suited to sparse or highly dynamic networks. Common DTN protocols include Epidemic Routing, Spray and Wait, PRoPHET, MaxProp, and Message Ferry Routing.

The OPWP algorithm in [12] uses UAVs (ferries) that follow planned waypoint routes with specified wait times, as shown in Figure 9. This enables efficient message delivery

without real time coordination and allows the network to function reliably in sparse and disconnected environments.

While DTNs are robust, many rely on packet replication to improve delivery rates, which creates storage and bandwidth overhead in more stable or well connected networks [70]. Hybrid MANET–DTN schemes aim to combine MANET responsiveness with DTN resilience. The method in [70] uses local packet buffers that hold data when no path is available and resume forwarding when connectivity is restored, though delays still occur without mechanisms to actively move data forward.

More recent work, such as [10], introduces adaptive routing that switches between cooperative forwarding and reactive store–carry–forward based on network conditions. These approaches are effective in disaster relief settings with limited UAV availability and sparse ground coverage, where periodic asynchronous communication is sufficient for large search areas.

- **Wireless Mesh Network (WMN) Protocols** WMN protocols aim to create reliable, scalable multi hop communication between UAVs. They typically use proactive or hybrid routing strategies and perform well in relatively stable clusters. Common WMN protocols include Hybrid Wireless Mesh Protocol (HWMP), Better Approach to Mobile Adhoc Networking (BATMAN), Optimised Link State Routing (OLSR), Multi-Gateway Routing (MGR), Proactive Routing Protocol for Mesh Networks (BMF), and Distance Routing Effect Algorithm for Mobility (DREAM) [16].

Compared to MANET routing, WMN protocols such as HWMPv2 use dynamic root election and improved link metrics to better handle UAV mobility. By selecting paths based on link stability and motion, they achieve higher throughput and fewer dropped packets in dynamic aerial mesh networks [81, 73].

Recent work proposes routing techniques tailored to highly dynamic and dense UAV networks. TARRAQ [21] uses adaptive Q-learning to enable autonomous routing decisions based on topology changes, while PARRoT [82] combines reinforcement learning with UAV trajectory prediction to proactively adjust routes before disruptions occur, reducing delay and improving efficiency.

More broadly, AI-based routing protocols apply machine learning to predict changes in topology, traffic patterns, and link quality using throughput data [74]. These schemes offer improved adaptability and reliability but introduce additional computational overhead and may be unnecessary in simpler, less dynamic networks.

Overall, WMN protocols provide reliable, multi hop connectivity for UAV-based communication in disaster response, supporting real time coordination in search and rescue and offering widespread network access to affected individuals.

SAR focused routing

There are multiple papers which have looked at routing protocols through the lense of Search and Resuce. The Location aware Message Delivery (LMD) protocol [40] enables short message exchange without the need for infrastructure or continuous end to end connectivity.

It performs well when node density is sufficiently high, as it can avoid energy intensive multi-copy or network flooding strategies through its reliance on location aware forwarding. Study has also been conducted into how routing specific protocols can be used to maintain consistent quality of service (QoS) in post-disaster settings. [96] introduces a dynamic priority scheduling system that adjusts based on current and predicted network conditions, such as the connection of additional users. It incorporates mobility patterns, signal quality, and expected future traffic, using the Gauss–Markov Mobility Model to better mirror real world UAV behaviour.

2.3.10 Security and Regulatory Requirements

In disaster response scenarios, the reliability of UAV networks is critical but so too is their resilience to security threats and compliance with operational regulations. Due to the nature of wireless communications, UAV systems are inherently vulnerable to risks such as eavesdropping, jamming, spoofing, intrusion attacks, and even physical capture [16]. These threats can compromise mission critical data, disrupt coordination, or result in loss of control over UAV units or swarms. While traditional encryption standards such as the Advanced Encryption Standard (AES) offer strong protection, they can be an expensive overhead for UAVs with limited onboard resources, especially during real time operations [38].

To enhance protection, lightweight cryptographic methods, authentication schemes, and physical layer security techniques have been proposed [5, 79]. These include asymmetric encryption(such as Elliptic Curve Cryptography (ECC), trust based protocols, and even blockchain based frameworks for data validation and traceability [94, 89]. Other work explores physically unclonable functions (PUFs) to prevent tampering, and machine learning models to detect abnormal behaviour or intrusion attempts [4, 19].

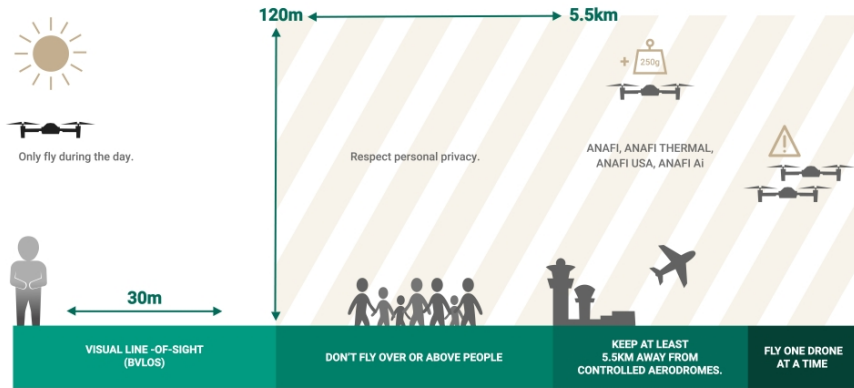


Figure 10: Drone regulations in Australia by CASA [64]

In parallel with network security, UAV operations are also subject to regulatory constraints, particularly around airspace access, flight beyond visual line of sight, and data privacy as shown in Figure 10. Disaster situations often require temporary exceptions or emergency authorisations, but operators must still ensure compliance with relevant civil aviation and

privacy regulations. As UAV deployments scale in complexity and autonomy, coordination with authorities becomes essential. This includes factors such as managing frequency usage, available flight zones, and identity authentication.

Network Lifetime, Energy Management and Self Deployment

Maintaining network availability in UAV based systems requires both initial deployment and continuous energy aware coordination to ensure long term operation. Network lifetime is a key aspect in this, and is defined by the ability of UAVs to sustain communication coverage and mission tasks over extended periods despite their limited battery capacity [17, 16].

To address this, modern multi-UAV systems incorporate self deployment mechanisms that allow drones to autonomously rotate in and out of a network. When a UAV reaches a low energy threshold, it must be capable of disengaging from the network, navigating to a charging station or return base, and being replaced by a new UAV without disrupting the network's structure or communication links. This requires scheduling, efficient handoff coordination, and real time monitoring of energy levels across the fleet, and is explored in works [78, 17, 47].

Autonomous substitution is important in disaster zones, where continuous coverage is essential for ongoing search, monitoring, or relay tasks. In reality, this is challenging due to differences within UAV fleets, where drones may have varying flight endurance, payload capacities, and energy consumption rates. Effective self deployment strategies must account for these differences, ensuring that UAVs with sufficient energy and capability assume the most demanding roles, while lower capacity units are cycled out appropriately [78, 47].

While some existing control algorithms incorporate energy metrics into task scheduling, there is still a need for frameworks that balance network integrity with energy aware role assignment. Future directions have been proposed and include distributed energy aware decision making, energy forecasting, and cooperative recharging. This research will be key in enabling UAV swarms to maintain continuous operation in the field with minimal human interference [16].

2.4 Network Technologies for Multi-media Data Transmission

2.4.1 LoRaWAN

LoRaWAN (Long Range Wide Area Network) is a communication protocol built on LoRa modulation, operating in sub-GHz ISM frequency bands, depending on the region in which it is deployed [9]. In Australia, this includes the 915- and 923-MHz ranges. Low frequency operation enables high signal penetration through obstacles like buildings, foliage, and varied terrain, making it particularly valuable in the complex environments encountered during disaster response efforts.

LoRaWAN is characterised by its low power consumption and long communication ranges, often exceeding 10 km in rural or open areas [90]. This makes LoRaWAN well suited

for connecting distributed low power IoT sensors deployed on the ground. In search and rescue (SAR) operations, UAVs can act as aerial gateways, collecting data from ground sensor nodes and forwarding it to command centres. This is shown in studies [86] and [80] which demonstrate how gathering positional and environmental data is key in increasing situational awareness in the absence of infrastructure.

However, the advantages of LoRaWAN come with trade offs. Its low data rate often only a few kilobits per second [9, 16] and strict payload limitations make it unsuitable for real time communication, large scale UAV telemetry exchange, or swarm coordination. LoRaWAN also typically follows a multi-star network topology, which limits the potential for true multi-hop or mesh-style communication between UAVs [16]. As a result, while LoRaWAN can extend ground coverage and support passive sensor nodes, it lacks the throughput, responsiveness, and flexibility required to deploy and sustain a UAV network independently.

2.4.2 Wi-Fi 802.11

Wi-Fi technologies, based on the IEEE 802.11 family of standards are widely used in FANETs due to their high data throughput, compatibility, and availability in consumer grade hardware such as phones or laptops. In disaster recovery and SAR scenarios, Wi-Fi is often deployed to enable direct control, real time video streaming, and data exchange between ground personal and ground stations, or among UAVs themselves. While several variations of Wi-Fi exist each offering different trade offs in speed, range, and power consumption, traditional high frequency Wi-Fi standards and newer sub-GHz variants such as Wi-Fi HaLow have their own unique roles in SAR operations.

Conventional Wi-Fi Standards

Traditional Wi-Fi technologies operating at 2.4 GHz and 5 GHz frequencies, such as IEEE 802.11n/ac (Wi-Fi 4 and Wi-Fi 5), are commonly used in UAVs for high bandwidth applications. These standards offer high data rates, making them suitable for transmitting live video feeds, images, sensor payloads, and large data files. Their popularity is also driven by their ability to connect with widely available consumer devices, such as smartphones, laptops, and tablets, which can serve as ground control interfaces or user endpoints [16].

However, these benefits come with limitations. Wi-Fi in the 2.4 GHz and 5 GHz bands suffers from relatively short effective ranges, high susceptibility to interference, and limited penetration through obstacles such as walls, trees, or terrain [97]. These drawbacks can be problematic in disaster environments, where line of sight conditions may be poor and connectivity must be maintained over wide, obstructed areas. Furthermore, high frequency Wi-Fi tends to consume more power, reducing the UAV flight times or requiring extra battery weight.

Despite these trade offs, conventional Wi-Fi remains a well researched option for short range, high throughput communication in UAV networks. It is particularly useful where existing Wi-Fi infrastructure is intact or where relays can be placed to ensure line of sight connections. In multi-UAV deployments, the coverage limitations of high frequency Wi-Fi

can be addressed by deploying swarms of UAVs, to extend the network's effective range. By carefully spacing UAVs, these systems can maintain consistent data links across complex terrains while preserving bandwidth intensive services [16].

A major draw of the Wi-Fi 802.11n/ac standard is their capability of simultaneously servicing a large number of users, making them especially effective where connectivity must be provided to both SAR personal and the affected population. This includes situations such as during large scale evacuations or temporary aid setups [16]. Recent work has also explored the use of directional antennas and mechanical heading control on UAVs to extend Wi-Fi range in field deployments [35], showing promise in scenarios requiring temporary high bandwidth connectivity.

Wi-Fi Mesh Networking (IEEE 802.11s)

While conventional Wi-Fi technologies offer strong data throughput, their limited range and reliance on infrastructure can hinder their utility in wide area or obstructed environments. IEEE 802.11s addresses this by enabling mesh networking capabilities over standard Wi-Fi channels. In a mesh network, each UAV acts as both a communication endpoint and a relay, allowing data to hop between drones and dynamically route around obstructions or failed nodes [16].

Mesh networking allows coverage to be extended over large areas without drastically having to upscale the number of ground stations. This also helps to ensure reliable communication even when the ground station is out of LoS. Research has shown that operating UAV mesh nodes at elevated altitudes can reduce urban interference and improve signal propagation between nodes [58].

Wi-Fi HaLow (IEEE 802.11ah)

Wi-Fi HaLow, based on the IEEE 802.11ah standard, is a low power, sub-1 GHz wireless communication protocol specifically designed for long range, low bandwidth IoT applications. Operating primarily in the 850–950 MHz band, varying on region, Wi-Fi HaLow achieves better terrain penetration and obstacle avoidance compared to conventional 2.4/5 GHz Wi-Fi technologies [51, 90]. This makes it particularly well suited for use in disaster environments, where communication must be maintained through areas with vegetation, buildings, or rugged terrain.

In contrast to LoRaWAN, which also operates in the sub-GHz band but is limited by low data rates and payload capacity, Wi-Fi HaLow supports higher throughput reaching tens of megabits per second depending on conditions and native IP connectivity [90]. This enables more complex interactions, such as UAV telemetry, low resolution imagery and video, and command/control messaging, while still maintaining a low power profile ideal for battery powered drones [97].

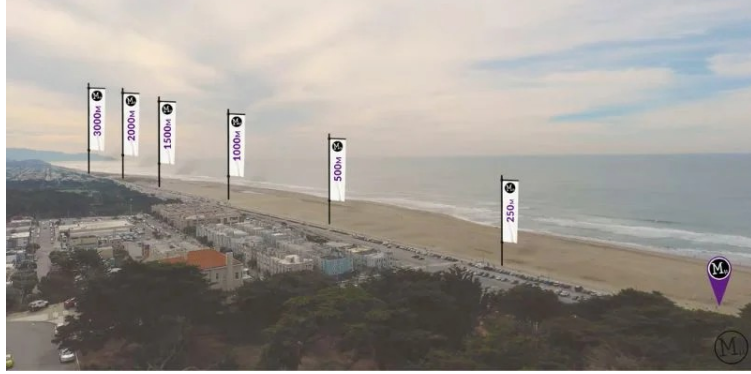


Figure 11: Morse Micro 3km urban range test [59]

Morse Micro, a leading developer of Wi-Fi HaLow solutions, has demonstrated PHY rates of up to 43.3 Mbps on its newest HaLow chip sets [55]. These performance levels are achieved through the integration of the radio, PHY, and MAC layers into a single, compact SoC designed for ultra low power and long range communication [56]. The platform is specifically designed for applications that require reliable connectivity over extended distances with minimal energy consumption making it suitable for UAV deployments in disaster response and IoT sensor networks. Recent field tests with Morse Micro's development kits have shown high coverage capabilities, achieving video throughput at ranges of up to 3 km in near line of sight (LoS) urban environments Figure 11 [59] and up to 16 km in rural settings [41, 60].

A key advantage of Wi-Fi HaLow is its support for mesh networking, large scale device connectivity (up to thousands of nodes), and Quality of Service (QoS) features that come with the IEEE802.11 standard. These capabilities make it a good option for multi UAV mesh networks, particularly in search and rescue operations where UAVs must communicate with each other and with dispersed ground teams. Unlike conventional Wi-Fi, HaLow is designed for longer ranges, often exceeding 1 km in open environments [90], allowing for greater spacing between UAVs [97] and greatly reducing the number of UAVs needed to cover an area.

However, Wi-Fi HaLow adoption remains limited because most consumer devices, including smartphones and tablets, do not yet support 802.11ah, making HaLow networks less accessible for direct users [90]. Still, for UAV-to-UAV and UAV-to-ground links within closed system mesh networks, HaLow offers a good balance of range, energy efficiency, and IP-level compatibility, making it a practical choice for UAV communication in disaster response scenarios. Additionally, the low adoption rate is beneficial as it results in lower channel congestion in populated areas.

There's growing interest in exploring how Wi-Fi HaLow could be used in real world SAR missions and drone deployed networks, but more research is still needed to understand its practical effectiveness.

2.5 Knowledge Gaps and Future Research Directions

2.5.1 Field Testing and real world Validation of Wi-Fi HaLow

While sub-1 GHz wireless technologies have been previously explored for UAV applications [97], the use of IEEE 802.11ah (Wi-Fi HaLow) specifically in UAV based search and rescue (SAR) networks remains largely unexamined. Existing literature on 802.11ah tends to focus on IoT and smart infrastructure applications. This research has shown the need for performance validation in a mix of urban, rural and complex terrain environments. The protocol's ability to support long range, IP compatible, low power communication along with native support for mesh networking via 802.11s makes it a promising candidate for resilient UAV mesh deployments in SAR operations.

Recent demonstrations of Morse Micro's 802.11ah development kits suggest that real world performance may exceed that reported in earlier academic studies, particularly in terms of range and signal stability. These kits, when mounted to UAV platforms and tested in the field, could offer critical insights into the practical viability of Wi-Fi HaLow for UAV mesh networks.

2.5.2 Drone Deployment Algorithm Purpose Built for SAR

Current UAV deployment algorithms for network coverage and coordination often operate in two-dimensional space and rely heavily on probabilistic mobility models. While these models are useful for general communication scenarios, they often fall short when applied to the complex terrains encountered in Search and Rescue (SAR) operations. There is a clear need for a specialised deployment algorithm that takes into account the unique behavioural and environmental constraints of SAR missions, particularly the impact of Line of Sight (LoS) on signal quality and clustering nature of search teams.

Verification remains another major limitation. Many proposed systems are assessed only through simulation and are not checked against real signal behaviour, leaving uncertainty about how well their assumptions hold in practice. This work addresses part of that gap by validating the underlying HaLow link-quality and propagation models against empirical measurements, rather than performing full UAV deployment trials. By confirming that the signal and throughput models remain accurate in the presence of noise, interference, and environmental loss, the study strengthens confidence in the optimisation framework, while full end-to-end field validation of deployment strategies is left for future work.

3 Methodology

This thesis combines experimental measurements with modelling to develop a terrain aware UAV deployment framework for search and rescue communication. The methodology is presented in two parts. The first, consists of controlled Wi-Fi HaLow ground to ground and ground to air tests that characterise real link behaviour, including RSSI, noise, interference and throughput. These tests provide the data needed to validate and calibrate the propagation and throughput models used later in the optimisation.

The second, develops a multi objective UAV placement algorithm that uses a high resolution Digital Elevation Model, terrain aware signal attenuation model, and throughput calculations. The algorithm uses NSGA-II to generate UAV placements that balance end to end throughput and coverage of ground nodes. An interactive 3D visualisation tool is also used to inspect solutions and evaluate network topology and multi hop backhaul routes.

Together, these experimental and modelling components provide a basis for evaluating UAV network performance in realistic search and rescue environments. The following subsections describe the testing procedures, modelling assumptions and optimisation workflow used in this study.

3.1 Wi-Fi HaLow Testing Methodology

This subsection details the experimental methodology used to evaluate Wi-Fi HaLow (IEEE 802.11ah) for search and rescue communication scenarios. We consider both ground-to-ground (G2G) and ground-to-air (G2A) links using a pair of HaLowLink 1 evaluation kits and a multi-rotor UAV capable of carrying the Wi-Fi and battery payload. Procedures, instrumentation, variables and data management are documented so that results can be reproduced and compared across sites and days.

3.1.1 Purpose and Scope

The objectives of the testing campaign are to:

1. Measure RSSI, noise floor, and throughput for G2A links across controlled altitudes and lateral offsets to calibrate the HaLow propagation model.
2. Establish a G2G baseline over the same ranges to isolate altitude, airframe, and antenna-orientation effects.
3. Quantify interference from motors and onboard avionics during hover by comparing against a stationary control at equivalent geometry.
4. Validate data to confirm the accuracy of the propagation and throughput models.

3.1.2 Equipment and Configuration

Wi-Fi Halow and firmware:

Two Morse Micro HaLowLink 1 kits are used as the local and remote endpoints, paired following the Morse Micro setup guide [55]. The 4.3 V VFEM option is enabled to give the front-end module additional voltage headroom, providing slightly higher and cleaner transmit power than the default 3.3 V setting without affecting receiver noise figure or sensitivity.

Country code AU is used to match the test location. Channel 44 (925 MHz) is selected based on the locally permitted operating range, with an 8 MHz channel width chosen for its higher PHY rates at the expected ranges and noise conditions. Dynamic channel switching is disabled to minimise variability between runs, although the HaLowLink firmware supports adaptive channel selection using EWMA or Sample-and-Hold algorithms. Security is configured consistently across all tests using WPA3-SAE (CCMP).

Air platform

The quadcopter used was a custom 10" ArduPilot-based platform with the HaLow module mounted underneath, facing vertically down. The airframe used was a Tarot 650 fitted with 10"×4.5" bi-blade propellers, driven by four EMAX 2814-730Kv motors and a 4-in-1 45A ESC. A Pixhawk Pro-based flight controller running ArduPilot provided stabilised flight and waypoint navigation, supported by an M10 GPS and compass module. Power was supplied by a 4S 5500 mAh LiPo battery, enabling up to 30 minutes of flight. Vehicle control and telemetry were handled by a 2.4 GHz ELRS link and a 915 MHz MAVLink link.

This configuration offers stable, repeatable flight performance suitable for controlled G2A link testing. While the onboard compute is sufficient for these tests, future autonomous deployment of the optimisation framework would benefit from an additional companion computer.

Positioning and timing

GPS coordinates are entered for both endpoints and great-circle distances are computed to determine the range for each test condition. Each iperf3 run uses a fixed duration of 10 s, repeated three times per condition to capture short-term variability in throughput and noise floor measurements.

Auxiliary

Ground nodes are mounted on 1.0 m tripods to minimise ground reflection and attenuation. Test locations are selected to maximise local elevation where possible, reducing obstructions and improving Fresnel-zone clearance. These measures aim to standardise the geometry across runs and reduce environmental variability between G2G and G2A measurements.

3.1.3 Test Sites and Layout

Sites are selected to provide clear line of sight for the required ranges, predominantly concave terrain with minimal elevation gain to avoid unintended Fresnel obstruction, safe and accessible launch and landing zones, and moderate to low RF noise. All tests comply with local operating rules and permissions.

3.1.4 Experimental Factors and Test Matrix

Table 1 summarises the planned test campaigns. G2A altitudes are chosen to keep the first Fresnel zone clear while remaining within site constraints.

Table 1: Wi-Fi HaLow test matrix.

Test	Geometry	Range set	Notes
T1	G2G baseline	Equal range increments	Ground tripods, no airframe present
T2	UAV interference	Fixed range (40 m)	Fixed distance between receivers.
T3	G2A range sweep	Equal range increments	10 m AGL. Paired with G2G

3.1.5 Procedures

Common setup Before each test block, the following steps are performed to ensure consistent configuration and environmental conditions:

1. Verify both HaLowLink kits are configured as described in Section 3.1.2.
2. Mount and power the remote kit (airframe or tripod), ensuring antenna orientation matches the ground unit.
3. Mount the local kit on a ground tripod at the designated reference point and confirm antenna alignment.
4. Perform a 900 MHz spectrum scan using the Morse analyser to check for interference or overlapping transmissions.
5. Measure and record the ambient noise floor and note any identifiable interference sources.
6. Confirm successful association between the units, verifying channel, bandwidth, and link stability.
7. Observe a stable idle RSSI for at least 10 s before beginning throughput testing.
8. Enter or confirm GPS coordinates for both endpoints and assign a unique dataset label to the run block.

G2G baseline (T1)

The baseline characterises the link without airborne effects.

1. Place both radios on tripods at 1.0 m AGL.
2. Perform a range sweep across the planned test distances.
3. At each distance, run the MorseMicro range tool outlined in Section 3.1.7.
4. Repeat each condition three times.

UAV interference (T2)

This test evaluates the effect of platform avionics on HaLow link performance.

1. Perform a G2G reference measurement at a fixed lateral distance of 40 m, using the standard protocol sequence.
2. Position the airframe at approximately 5 m AGL at the same 40 m lateral separation and allow the link to stabilise.
3. Repeat the G2A measurements under two conditions:
 - (a) **Telemetry off:** the 915 MHz MAVLink radio disabled.
 - (b) **Telemetry on:** the 915 MHz MAVLink radio enabled to assess co-channel and harmonic interference.
4. Perform three trials per condition and compare the resulting noise floor, RSSI, and throughput against the G2G baseline.

G2A range sweep (T3)

This test measures airborne link performance across altitude and lateral separation.

1. Position the airframe at the target altitude (10 m AGL) in Loiter mode. Due to wind, small drift of approximately ± 2 m is expected. Allow 10 s for the link to stabilise.
2. Run the standard protocol sequence using the MorseMicro range tool outlined in Section 3.1.7.
3. Repeat the measurement two times for each distance (due to flight time constraints).
4. If packet loss exceeds a predefined threshold or the link drops, note the condition and rerun the test or proceed to the next closer range.

3.1.6 Measurements and Data Recording

Each run records both link-quality metrics and protocol-level throughput results. The primary measurements are:

- Received power (RSSI, dBm) and noise floor at both endpoints.
- UDP goodput, jitter, packet count, and loss ratio. TCP goodput, retransmissions, and congestion statistics. Collected using iperf3.
- MAC-layer indicators including retry counts, TX ACK timeouts, and round-trip success, used to infer link stability.
- Device temperature and supply voltage as indicators of thermal and power stability.
- Endpoint coordinates and the computed range value.
- Test metadata such as timestamp, channel, bandwidth, and transmit power.

Each run produces a structured JSON record containing these fields along with the assigned test label, allowing multiple trials at each distance to support averaging, dispersion estimates, and outlier handling.

3.1.7 HaLowLink 1 Range-Test Tool

The built-in range-test interface standardises data entry and acquisition. Figure 12 shows the main screen.

Remote device **Discover** (button)

The remote device which this test will be conducted against

Password *

Remote device password

Description

Optional: short description of the test conditions

Local device coordinates

Optional: Must be provided in Decimal Degrees (DD) format, used by Google Maps

Remote device coordinates

Optional: Must be provided in Decimal Degrees (DD) format, used by Google Maps

Range (m)

The distance between devices under test

Protocol	<input checked="" type="radio" value="UDP"/> UDP	<input type="radio" value="TCP"/> TCP	▼
Data Direction	<input type="radio" value="Send"/> Send	<input type="radio" value="Receive"/> Receive	▼

(a) HaLowLink 1 range-test interface.
(b) UDP/TCP test mode selector.

Figure 12: HaLowLink 1 range-test tool showing configuration and protocol selection.

The range test fields are as follows:

1. **Remote device selection:** A list of the paired devices by hostname and IP. The interface validates reachability before tests start.
2. **Coordinates:** The latitude and longitude for local and remote nodes. Points were sourced from Google Maps using an external mobile device.
3. **Range:** Auto computed using great-circle range from the local and remote device coordinates.
4. **Description:** A free-text identifier used to tag runs. Labels encode the scenario and condition (for example, `drone_los_3.0`, `beach_los_1.1`). These tags are used by the parsing scripts to group and filter records in the results section.
5. **Protocol and direction:** Allows for changing iperf3 settings. Fields include UDP, TCP, send and receive. A test duration of 10 s per run is used.

The tool exports one JSON record per run containing the data outlined in Section 3.1.6. This structure enables reproducible post-processing without manual transcription. Optionally, all data can be downloaded into a single JSON file if required.

Time	Remote Host	Description	Distance (m)	Location	Bandwidth (MHz)	Channel	UDP Throughput (Mbps) (Send/Receive)	TCP Throughput (Mbps) (Send/Receive)	Signal Strength (dBm)	Data
10/5/2025, 4:28:45 PM	halowlink1-4ffb (192.168.12.121)	los1	67	map view	8	44(924 MHz)	21.53 / 19.95	17.08 / 17.08	-54	<button>Download</button> trash
10/5/2025, 4:29:56 PM	halowlink1-4ffb (192.168.12.121)	los1.1	67	map view	8	44(924 MHz)	18.84 / 20.48	16.39 / 16.88	-55	<button>Download</button> trash

Figure 13: HaLowLink 1 range-test output showing example line-of-sight (LoS) test results.

3.1.8 Controls, Safety, and Limitations

Controls and Internal Validity

To maintain consistency across runs:

- Identical hardware, firmware, security settings, and radio configuration are used for all tests.
- Antenna orientation, height, and mounting geometry are kept fixed between repetitions.
- A short interference scan is performed where feasible, and congested or noisy sub-bands are avoided.
- Coordinates and metadata are recorded for every run to support data analysis.

Operational Constraints and safety

Flight operations follow local UAV regulations, including restrictions on maximum altitude, separation from people, and visual line-of-sight requirements. Wind limits, light rain, and attachment issues are managed through contingencies. These include increasing sampling density at shorter ranges when long corridors are not available, protecting HaLow kits from drizzle, and switching to alternative mounts if EMI or sensor conflicts are suspected. Testing is paused if sudden environmental changes affect link quality. For G2A trials, repetitions were reduced from three to two at each location to preserve battery life and maximise the number of distinct range points collected.

Methodological Limitations

Several practical limitations influenced the generality and completeness of the dataset:

- **Battery and endurance constraints:** Limited flight time restricts repetitions at each distance and prevents longer-range sweeps at higher altitudes.
- **Fresnel-zone clearance:** Not all sites permitted full Fresnel-zone clearance. Ground based diffraction and partial obstruction were unavoidable at longer test ranges.
- **Range estimation:** Distance is computed from GPS coordinates, which do not account for vertical separation; true 3D range must be corrected using DEM data.
- **Environmental variability:** Terrain, foliage density, and multipath behaviour differ between test sites and across days, introducing temporal variability in noise floor and RSSI.
- **Platform constraints:** Limited UAV availability prevented air-to-air (A2A) measurements and constrained testing to G2G and G2A scenarios.
- **Network topology limitations:** With two HaLow kits, full end-to-end tests (G2A2G), meshing and multi-hop relaying could not be tested.
- **Regulatory constraints:** UAV altitude limits and available frequencies in the AU 915–928 MHz band restrict the test envelope compared to what might be achievable in unrestricted airspace.

Despite these limitations, the dataset provides a robust foundation for validating the signal and throughput models used in the optimisation framework, particularly for G2A links over realistic terrain profiles.

3.2 Algorithm Methodology

This section describes the methodology used to optimise multi-UAV placement over real terrain for Wi-Fi HaLow mesh networking. The approach builds on an NSGA-II baseline [75] and incorporates high-resolution terrain data together with an extended signal model that accounts for line of sight, Fresnel effects, vegetation loss and calibrated HaLow throughput. A throughput based multi-hop backhaul model is also included so that UAV placement can be evaluated under realistic search and rescue conditions.

The following subsections outline the main stages of the algorithm, the supporting tools and the models used in the implementation.

3.2.1 Node Definitions and Network Structure

We consider a wireless network consisting of three kinds of nodes, BHs, GNs and UAVs, which are represented by the sets \mathcal{B} , \mathcal{G} and \mathcal{U} , respectively. These nodes are defined as follows:

Ground Nodes (GNs)

Ground nodes represent personnel, sensors, or devices requiring connectivity. Their positions are defined in the same coordinate frame as the DEM and represented as fixed 3D coordinates (x, y, z_0) , where z_0 is obtained from the DEM plus any device-specific height offset. GNs act as points whose uplink throughput to the backhaul must be maximised.

UAVs and Constraints

Each optimisation variable is a UAV position (x, y, h) , where h is altitude above ground level (AGL). The search space is horizontally bounded by the DEM extent and vertically bounded by mission and regulatory limits. Hard constraints applied in the optimiser include:

- Minimum altitude above terrain for collision avoidance.
- Maximum altitude (120 m regulatory limit, unless otherwise permitted).
- Horizontal bounds defined by the DEM coverage area.

Altitudes can be fixed to specific hover levels or be part of the optimisation variables depending on the setup.

Backhaul (BHs)

A single fixed backhaul node acts as the gateway to the wider network (e.g., a command vehicle or a satellite uplink). UAVs must form a communication path to the backhaul, either directly or through UAV–UAV relays. The optimiser evaluates end-to-end throughput from each GN to the BH, incorporating link-level throughput estimates and a per-hop throughput reduction factor.

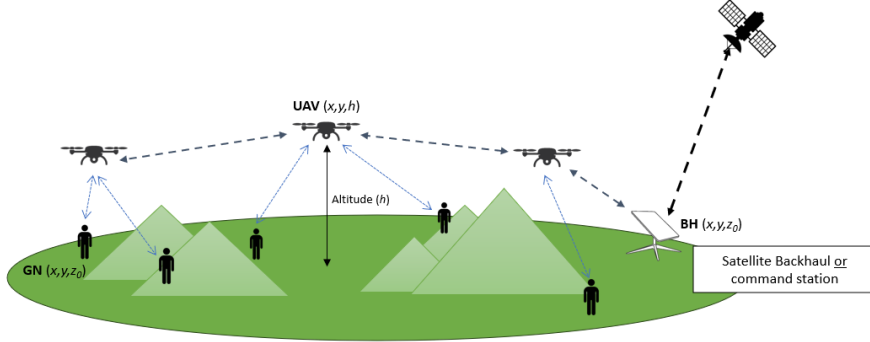


Figure 14: System model overview of ground nodes (GN), UAVs, and BH(s) over a search area.

All nodes operate within a rectangular region \mathcal{A} defined by the DEM bounds. Nodes are assumed to be equipped with omnidirectional transceivers and GPS, enabling them to determine their position and communicate in all directions within the network graph.

3.2.2 Terrain Data Fetching from ELVIS Database

Terrain elevation data is obtained from the ELVIS (Elevation Information System) database [42] to generate a Digital Elevation Model (DEM) of the target search area. The DEM provides the topographical context required for terrain-aware UAV placement, enabling line-of-sight checks, and Fresnel and knife-edge diffraction calculations. Elevation data is processed using the `rasterio` and `numpy` libraries in Python to extract height values and compute surface gradients.

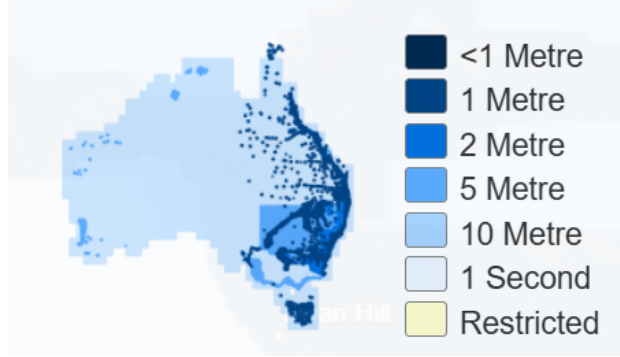


Figure 15: Spatial coverage of ELVIS (Elevation and Depth Information System) DEM data.

ELVIS provides DEMs at multiple resolutions (sub-metre, 1 m, 2 m, 5 m, 10 m, and 1 arc-second), as shown in Figure 15. Higher-resolution models improve the fidelity of LoS and diffraction checks but increase computational cost. The implementation therefore supports configurable down-sampling to balance accuracy and runtime. For optimisation, the highest-resolution model available for the site is used to preserve fine topographic detail, whereas for interactive visualisation the DEM is down-sampled to enable real-time rendering on lower-powered hardware.

3.2.3 Signal Modelling

The link budget is evaluated using a deterministic, dB-domain model that combines free-space path loss with attenuation from terrain, vegetation, and other environmental factors. This follows the standard format for wireless propagation, with distance and obstruction dependent losses, and an environment margin. The received power at distance d is

$$P_{\text{rx}}(d) = P_{\text{tx}} + G_{\text{tx}} + G_{\text{rx}} - L_{\text{FSPL}}(d) - L_{\text{foliage}} - L_{\text{diff}} - M_{\text{env}}, \quad (1)$$

where

- P_{tx} : Conducted transmit power (dBm),
- $G_{\text{tx}}, G_{\text{rx}}$: Antenna gains (dBi),
- $L_{\text{FSPL}}(d)$: Free-space path loss (dB),
- L_{foliage} : Vegetation attenuation (dB),
- L_{diff} : Knife-edge diffraction loss (dB),
- M_{env} : Empirical environment margin (dB).

The interference margin consolidates implementation-specific effects, including platform EMI, receiver desensitisation, and residual environmental variability. This value is derived from the HaLow measurements in Section 4.1.

Free-Space Path Loss (FSPL)

The FSPL term represents the attenuation due solely to geometric spreading in an unobstructed environment. It is computed using the standard logarithmic model

$$L_{\text{FSPL}}(d) = 20 \log_{10} \left(\frac{4\pi d f}{c} \right), \quad (2)$$

where d is the link distance (m), f is the carrier frequency (Hz), and c is the speed of light. This can also be expressed as

$$L_{\text{FSPL}}(d) = 20 \log_{10}(d) + 20 \log_{10}(f) - 147.55, \quad (3)$$

which is the algebraically equivalent form used the algorithms link-budget calculation.

Line-of-Sight (LoS) Checking

LoS between two nodes is determined using a ray-tracing approach over the DEM. The direct path is discretised into uniformly spaced samples, and each sample is compared against the terrain elevation. An obstruction is declared if any terrain point exceeds the height of the straight-line path. Each segment is also classified as either open air or vegetation, allowing the foliage attenuation model to be applied only where appropriate.

Vegetation Modelling (Weissberger MED)

Foliage attenuation is estimated using Weissberger's Modified Exponential Decay (MED) model [71], which is valid for $230 \text{ MHz} \leq f \leq 95 \text{ GHz}$. The model expresses foliage loss as a function of frequency f (in GHz) and foliage path length d_f (in m).

$$L_{\text{foliage}}(f, d_f) = \begin{cases} 0.45 f^{0.284} d_f, & 0 \leq d_f \leq 14 \text{ m}, \\ 1.33 f^{0.284} d_f^{0.588}, & 14 < d_f \leq 400 \text{ m}. \end{cases} \quad (4)$$

Here, d_f is obtained directly from the line-of-sight sampling routine as the cumulative distance of all path segments classified as vegetation. This model was selected based on guidance from a Morse Micro engineer, who noted that internal Wi-Fi HaLow propagation testing showed close agreement with Weissberger's predictions [88].

Fresnel Zone Clearance

Fresnel zone clearance is evaluated along each link to determine whether terrain or vegetation interferes with propagation. The radius of the n^{th} Fresnel zone at any point is

$$r_n = \sqrt{\frac{n\lambda d_1 d_2}{d_1 + d_2}}, \quad (5)$$

where λ is the wavelength, and d_1 and d_2 are the distances from the point of interest to the transmitter and receiver, respectively. This work uses the first Fresnel zone ($n = 1$).

The Fresnel zone can be considered obstructed when less than 60% of its radius is clear [44]. Paths failing this criterion are treated as obstructed, and the corresponding knife-edge diffraction model is applied. This includes non-LoS conditions where communication is only possible through diffraction mechanisms.

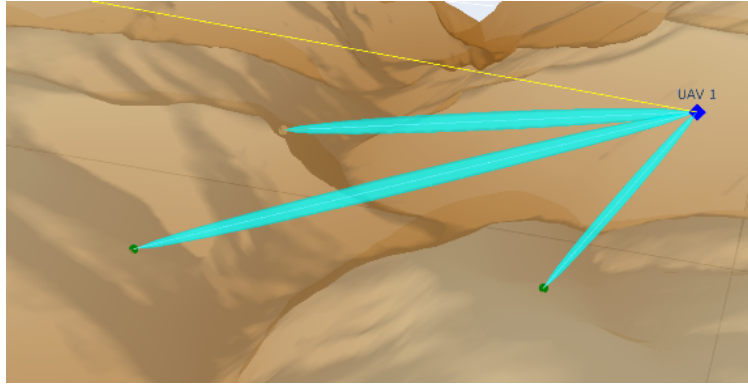


Figure 16: Illustration of LoS and Fresnel-zone evaluation between a UAV and ground node.

Knife-Edge Diffraction

When the first Fresnel zone is obstructed, additional attenuation is estimated using the standard knife-edge diffraction model. The Fresnel–Kirchhoff diffraction parameter v is

$$v = h \sqrt{\frac{2(d_1 + d_2)}{\lambda d_1 d_2}}, \quad (6)$$

$$L_{\text{diff}}(v) = \begin{cases} 0, & v \leq -0.78, \\ 6.9 + 20 \log_{10} \left(\sqrt{(v - 0.1)^2 + 1} + v - 0.1 \right), & v > -0.78, \end{cases} \quad (7)$$

where:

v : Fresnel–Kirchhoff diffraction parameter (unitless),

h : Height of the obstacle above the direct line-of-sight (m),

d_1 : Distance from the transmitter to the obstacle (m),

d_2 : Distance from the obstacle to the receiver (m),

λ : Wavelength of the signal (m),

L_{diff} : Knife-edge diffraction loss (dB).

This loss term accounts for the additional attenuation caused when the direct path is partially obstructed by terrain features such as ridge-lines or escarpment, forcing the signal to diffract over the obstacle rather than propagate in free space. Including diffraction effects is important in the optimisation model, as UAVs links often encounter near-line-of-sight conditions where modest diffraction loss may still permit connectivity.

By modelling this behaviour, the optimiser can distinguish between viable but attenuated links and completely blocked paths, leading to more realistic placement over terrain.

3.2.4 Wi-Fi HaLow Modelling

The physical layer is modelled using IEEE 802.11ah (Wi-Fi HaLow) with parameters matched to the HaLowLink 1 platform [55]. The model estimates effective end-to-end throughput from received signal strength (RSSI), with support for multi-hop paths, hop-division penalties, and multiple channel bandwidths.

Device and model parameters

Table 2 lists the fixed constants and device-specific parameters used across all experiments and optimisation runs. Threshold vectors for MCS selection follow the vendor-provided HaLowLink 1 tables and are embedded directly into the model for the 1 MHz, 2 MHz, 4 MHz, and 8 MHz bandwidths.

Table 2: Device and model parameters used in computation.

Quantity	Symbol / Code	Value
Physical constants:		
Thermal noise density	N_0	-174 dBm/Hz
Useful symbol period	T_u	32 μ s
Guard interval (short)	T_{GI}	4 μ s
OFDM efficiency	η_{OFDM}	{0.66, 0.72, 0.75, 0.8125} for $B = \{1, 2, 4, 8\}$
Dual BPSK factor (MCS10)	η_{DBPSK}	0.50
Device parameters:		
Receiver noise figure	NF	7 dB
Supported bandwidths	B	{1, 2, 4, 8} MHz
Model parameters:		
MAC+IP efficiency	$\eta_{MAC/IP}$	0.70 (default)
Residual packet error rate	PER	0.02 (default, configurable)
Hops (half-duplex penalty)	H	≥ 1 (rate divided by H)
Environmental assumptions:		
Noise floor (measured site average)	N_{floor}	-95 dBm

MCS parameters and sensitivity thresholds

The modulation and coding scheme (MCS) parameters and receiver sensitivity thresholds follow the vendor-provided HaLowLink 1 specifications, derived from the IEEE 802.11ah physical-layer definitions. Each MCS index specifies a modulation order m_i , code rate r_i , and a sensitivity threshold corresponding to the minimum RSSI required to achieve a 10% packet error rate for 1000-byte packets. These values are stored in lookup tables and used directly by the optimiser during throughput estimation.

MCS index	Modulation scheme	Coding rate	Phy rate (kbps) per BW				Minimum Receive sensitivity (dBm) per BW			
			1 MHz	2 MHz	4 MHz	8 MHz	1 MHz	2 MHz	4 MHz	8 MHz
0	BPSK	1/2	333	722	1500	3250	-105	-103	-101	-97
1	QPSK	1/2	667	1444	3000	6500	-102	-100	-97	-93
2	QPSK	3/4	1000	2167	4500	9750	-99	-97	-95	-91
3	16-QAM	1/2	1333	2889	6000	13000	-96	-94	-91	-88
4	16-QAM	3/4	2000	4333	9000	19500	-93	-90	-88	-85
5	64-QAM	2/3	2667	5778	12000	26000	-89	-87	-84	-80
6	64-QAM	3/4	3000	6500	13500	29250	-88	-85	-83	-79
7	64-QAM	5/6	3333	7222	15000	32500	-87	-84	-81	-77
10	BPSK	1/2 x 2	167	N/A			-107	N/A		

Figure 17: Provided MCS table showing modulation and coding scheme (MCS) index, corresponding PHY data rates, and empirically derived receiver sensitivities.

MCS mapping, Shannon capacity, and PHY ceiling

This stage maps a received signal strength value (RSSI) to an achievable PHY data rate by combining two components: (i) the continuous Shannon capacity derived from the measured SINR, and (ii) the discrete MCS limits imposed by the HaLowLink 1 hardware. Shannon capacity provides the theoretical upper bound, while the MCS thresholds determine the practical ceilings that can be sustained in real 802.11ah links.

1) Signal-to-noise ratio and Shannon capacity

For a bandwidth B (Hz), receiver noise figure NF (dB), and optional interference power I (dBm), the total noise power is

$$N_{\text{dBm}} = N_0 + 10 \log_{10}(B) + \text{NF}. \quad (8)$$

When interference is present, it is summed in linear power:

$$N_I = 10 \log_{10}(10^{N_{\text{dBm}}/10} + 10^{I/10}). \quad (9)$$

In this work, the effective noise floor N_{floor} is taken directly from the device measurements and used in place of the theoretical noise-interference term N_I . This reflects the total noise observed by the receiver, including thermal noise, receiver noise figure, ambient interference, and platform-induced effects. Using the measured floor provides a consistent and empirically grounded baseline for SINR estimation across tests and optimisation runs.

The resulting signal-to-interference-plus-noise ratio (SINR) is

$$\text{SINR}_{\text{dB}} = \text{RSSI}_{\text{dBm}} - N_{\text{floor}}, \quad (10)$$

and is converted to linear scale for the Shannon capacity:

$$C_{\text{Shannon}} = B \log_2(1 + \text{SINR}) \quad [\text{bps}]. \quad (11)$$

2) MCS-based spectral-efficiency ceiling

The discrete MCS levels in IEEE 802.11ah place practical limits on the achievable PHY rate. Each MCS index i defines the modulation order m_i (bits per symbol), coding rate r_i , and an OFDM efficiency factor η_{OFDM} that accounts for subcarrier usage and guard-interval overhead.

The OFDM efficiency is computed as

$$\eta_{\text{OFDM}} = \frac{N_{\text{sd}}}{N_{\text{FFT}}} \times \frac{T_u}{T_u + T_{\text{GI}}}, \quad (12)$$

where N_{sd} is the number of data subcarriers, N_{FFT} is the FFT size, and T_u and T_{GI} are the useful symbol period and guard interval as defined in the 802.11ah S1G specification [43].

The resulting spectral efficiency for MCS i is

$$\text{SE}_i = m_i r_i \eta_{\text{OFDM}} (\times \eta_{\text{DBPSK}} \text{ for MCS10}), \quad (13)$$

with the corresponding PHY-rate ceiling

$$C_{\text{MCS},i} = \text{SE}_i B. \quad (14)$$

This provides the maximum achievable rate for each modulation level and channel bandwidth. These calculations align with the rates in the HaLowLink 1 MCS table shown in Figure 17. Although the numerical values follow the 802.11ah S1G parameters, the formulation itself is generic to all OFDM-based 802.11 PHYs and can be altered for different hardware.

3) Combined PHY-domain capacity bound

For each RSSI value, the model first determines the admissible MCS by comparing the RSSI against the vendor sensitivity thresholds in Figure 17. The highest MCS whose sensitivity requirement is satisfied provides the ceiling rate C_{MCS} .

The final achievable PHY rate is then the minimum of the Shannon capacity and the selected MCS ceiling:

$$C_{\text{PHY}} = \min(C_{\text{Shannon}}, C_{\text{MCS}}), \quad (15)$$

ensuring that predictions remain physically realistic even when the SINR would permit a higher rate than the discrete modulation levels support.

4) Behaviour across bandwidths

Figure 18 illustrates how the continuous Shannon limits compare with the discrete MCS ceilings across different channel bandwidths with a noise floor of -95dBm . The Shannon curves increase smoothly with SINR, whereas the MCS curves rise in stepwise increments determined by the sensitivity thresholds. Wider channels provide higher peak rates, while narrower channels remain usable at lower RSSI values due to their reduced bandwidth and correspondingly lower sensitivity requirements.

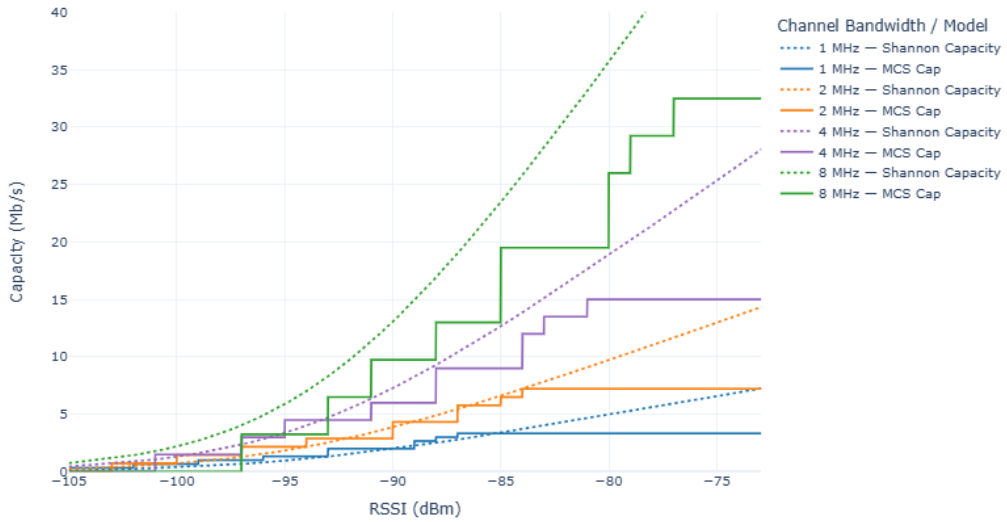


Figure 18: Shannon capacity and MCS-limited PHY ceilings for different channel widths.

Non-continuous PHY rate problem

The discrete Modulation and Coding Scheme (MCS) table yields stepwise changes in spectral efficiency as the received signal strength (RSSI) crosses sensitivity thresholds. This behaviour is physically accurate but problematic for multi-objective optimisation. Small UAV position changes can cause abrupt throughput jumps, and wide plateaus can drive many solutions to identical fitness despite differing average RSSI. These discontinuities matter when the link is MCS-limited rather than Shannon-limited, since the effective PHY rate is the minimum of the two. To stabilise the optimisation landscape while retaining physical realism, a one-sided exponential smoothing is applied to the MCS ceiling before taking the minimum, producing a continuous throughput curve.

Although NSGA-II does not require gradients, smoothing improves selection diversity. Where the MCS index is constant, populations may otherwise stagnate because small RSSI gains do not change fitness. The smoothed model provides differentiation within plateaus, maintaining evolutionary pressure toward stronger links.

Smoothing rationale: Each MCS step is replaced by a monotone ramp that starts at zero at its lower threshold T_i and rises continuously to one at the next threshold T_{i+1} . This preserves ordering and differentiates individuals within the same MCS step while avoiding artificial overshoot. Beyond T_{i+1} the ramp is clamped to one. The last step ramps to a fixed right edge P_{\max} .

Mathematical formulation: Let $\mathbf{T} = \{T_0, T_1, \dots, T_n\}$ be the ordered MCS sensitivity thresholds for bandwidth B , and define $T_{n+1} = P_{\max}$. Let $S_i = m_i r_i \eta_{\text{OFDM}}$ denote the spectral efficiency for MCS i and set $S_{-1} = 0$. Define the increments $\Delta S_i = S_i - S_{i-1}$. The smoothed spectral-efficiency curve is the cumulative sum

$$\tilde{S}(x) = \sum_{i=0}^n \Delta S_i R_i(x), \quad (16)$$

with one-sided exponential ramps

$$R_i(x) = \begin{cases} 0, & x < T_i, \\ \frac{1 - \exp[-k \frac{x-T_i}{T_{i+1}-T_i}]}{1 - \exp(-k)}, & T_i \leq x \leq T_{i+1}, \\ 1, & x > T_{i+1}, \end{cases} \quad (17)$$

where $k > 0$ controls ramp steepness and $P_{\max} = -50$ dBm bounds the final step. A value of $k = 8$ was chosen as it gives a smooth yet tight approximation to measured transitions for the HalowLink1's MCS table.

The smoothed MCS ceiling is

$$\tilde{C}_{\text{MCS}}(x) = \tilde{S}(x) B, \quad (18)$$

clipped for physical validity by

$$\tilde{C}_{\text{MCS}}(x) \leq C_{\text{MCS}}(x), \quad \tilde{C}_{\text{PHY}}(x) = \min(C_{\text{Shannon}}(x), \tilde{C}_{\text{MCS}}(x)). \quad (19)$$

Effect: Figure 19 shows how smoothing removes discontinuities while preserving the stepped character of Wi-Fi HaLow’s MCS thresholds. It maintains diversity under NSGA-II by introducing small but meaningful fitness differences within plateaus. Smoothing is used only inside the optimiser, with all experimental comparisons and reported figures use the discrete MCS tables.

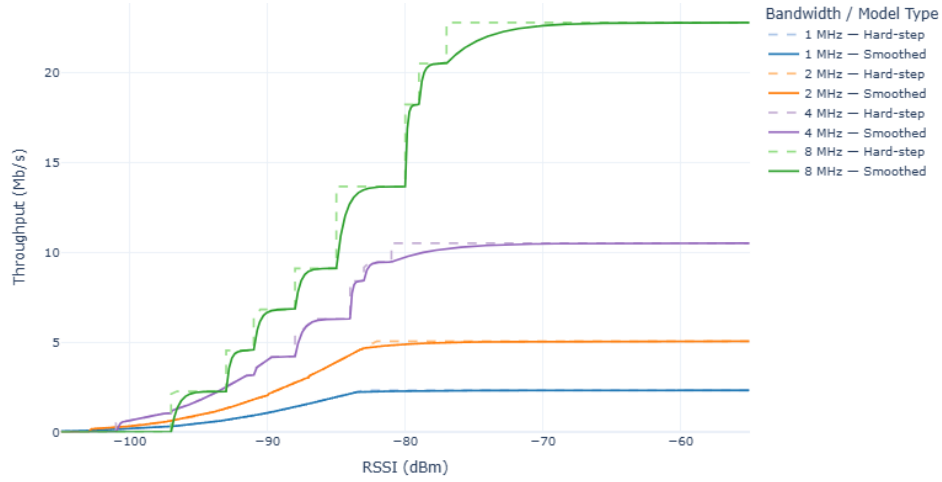


Figure 19: Discrete MCS steps versus smoothed exponential ceiling \tilde{C}_{MCS} .

Bandwidth selection and dynamic adaptation

Wi-Fi HaLow supports multiple bandwidth modes (1 MHz, 2 MHz, 4 MHz and 8 MHz), each offering a trade-off between range and throughput. Narrower channels improve receiver sensitivity by lowering the effective noise power, while wider channels achieve higher peak data rates at the expense of robustness as seen in Figure 19. The HaLowLink 1 platform supports automatic bandwidth switching, using internal decision logic such as EWMA-based averaging and sample-and-hold filters to determine when a change in channel width is required.

In this work, bandwidth adaptation was approximated by evaluating all supported channel widths for each link and selecting the one that produced the highest predicted throughput. This provides an idealised upper bound on performance without depending on a specific adaptation algorithm, while still capturing the trade-off between link margin and data rate.



Figure 20: Dynamic bandwidth selection showing active channel width versus RSSI.

PHY rate to Realistic Throughput

The physical-layer rate C_{PHY} , defined previously in Eq. (15), represents the maximum achievable bit rate at the modulation level but not the actual payload throughput available to the user. Protocol overheads, retransmissions, and multi-hop forwarding reduce the effective rate delivered to applications. These effects are modelled collectively using a set of system-level efficiency terms applied to the PHY rate.

$$T_{\text{eff}} = C_{\text{PHY}} \times \eta_{\text{MAC/IP}} \times (1 - \text{PER}) \times \frac{1}{H}. \quad (20)$$

The MAC/IP efficiency $\eta_{\text{MAC/IP}}$ represents framing, contention, and protocol overhead losses between the PHY layer and user payload. A value of 0.70 was used, consistent with measured UDP throughput on HaLowLink 1 devices under low-loss conditions and advertised by MorseMicro [61]. The packet error rate (PER) term accounts for residual link-layer losses not captured in the MCS sensitivity model. The hop term H represents the number of half-duplex relays in the end-to-end path, with each additional hop dividing throughput proportionally due to sequential transmission. This formulation provides a realistic mapping between the theoretical PHY ceiling and the usable link throughput.

3.2.5 Optimisation Algorithm

We optimise the 3-D placement of the UAV set \mathcal{G} over the terrain to serve ground nodes \mathcal{G} via a backhaul set \mathcal{B} as defined in Section 3.2.1. Each candidate $\mathbf{x} \in \mathbb{R}^{3|\mathcal{U}|}$ contains $(x_i, y_i, h_i^{\text{rel}})$ per UAV. Absolute altitude is $h_i = h_i^{\text{rel}} + \mathcal{T}(x_i, y_i)$, where \mathcal{T} is the terrain height from the digital elevation model [42].

End-to-end Throughput Model

Within the optimisation loop, each candidate placement \mathbf{x} must be evaluated in terms of the achievable data rate between every ground node and the backhaul. To couple the physical and network layer effects, the end-to-end throughput is defined as the minimum of the ground link and the UAV backhaul link throughput.

For any GN $g \in \mathcal{G}$ associated through UAV $u \in \mathcal{U}$, the GN link throughput $T_{g \leftarrow u}^{\text{GN}}$ is computed from the received power in Eq. (1) and used to get the PHY ceiling in Eq. (15), adjusted by the system efficiency in Eq. (20). The UAV backhaul throughput T_u^{BH} is computed by exploring all feasible routes from each UAV to the backhaul node \mathcal{B} using a breadth-first search (BFS). For each discovered path, the bottleneck RSSI is evaluated and mapped to a PHY rate, with the hop factor H applied to account for half-duplex relays (Section 3.2.4). The resulting end-to-end throughput for g is

$$T_g(\mathbf{x}) = \min(T_{g \leftarrow u}^{\text{GN}}, T_u^{\text{BH}}). \quad (21)$$

Objectives and Constraints

Let $\mathcal{S}(\mathbf{x}) = \{ g \in \mathcal{G} \mid T_g(\mathbf{x}) > 0 \}$ be the covered GN set. We solve a bi-objective minimisation for NSGA-II:

$$f_1(\mathbf{x}) = -|\mathcal{S}(\mathbf{x})| \quad (\text{maximise coverage}), \quad (22)$$

$$f_2(\mathbf{x}) = -\frac{1}{\max(1, |\mathcal{S}(\mathbf{x})|)} \sum_{g \in \mathcal{S}(\mathbf{x})} T_g(\mathbf{x}) \quad (\text{maximise average end-to-end throughput}). \quad (23)$$

A feasibility constraint enforces a minimum covered count C_{\min} :

$$g(\mathbf{x}) = C_{\min} - |\mathcal{S}(\mathbf{x})| \leq 0, \quad \text{with } C_{\min} = 2.$$

Evaluator

Distances are computed using the 3D Euclidean separation

$$d = \sqrt{(x_u - x_v)^2 + (y_u - y_v)^2 + (z_u - z_v)^2},$$

while LoS checks and attenuation terms follow the signal modelling stack in Section 3.2.3. Bandwidth is selected per-link by evaluating all supported $B \in \{1, 2, 4, 8\}$ MHz and taking the highest T . The full evaluation procedure is shown in Algorithm 1.

Algorithm 1: Evaluator function `_evaluate` for population X

Input : Population matrix X ($\text{pop_size} \times 3N_{\text{uav}}$), terrain heights \mathcal{T} , GN set \mathcal{G} , BH set \mathcal{B} , constants N_{uav} , MIN_COVERAGE

Output: Objective matrix $F \in \mathbb{R}^{\text{pop_size} \times 2}$, constraint vector $G \in \mathbb{R}^{\text{pop_size}}$

```

1 Initialise arrays coverage, avg_score, and G to zero
2 for each candidate i in population X do
3   Reshape X[i] into ( $N_{\text{uav}} \times 3$ ) matrix of  $(x, y, h_{\text{rel}})$ 
4   uav_abs  $\leftarrow$  COMPUTEABSOLUTEPOSITIONS(positions,  $\mathcal{T}$ )
5   uav_links  $\leftarrow$  BUILDUAVGRAPH(uav_abs,  $\mathcal{T}$ )
6   uav_bh_tp  $\leftarrow$  COMPUTEBACKHAULTHROUGHPUT(uav_abs, uav_links, backhaul_xyz)
7   (covered, sum_tp)  $\leftarrow$  EVALUATEGROUNDNODES(uav_abs, uav_bh_tp)
8   coverage[i]  $\leftarrow$  -covered
9   if covered > 0 then
10    | avg_score[i]  $\leftarrow$  -sum_tp/covered
11   else
12    | avg_score[i]  $\leftarrow$  0
13   G[i]  $\leftarrow$   $C_{\min} - \text{covered}$ 
14 F  $\leftarrow$  STACKCOLUMNS(coverage, avg_score); return (F, G)

```

Table 3: Description of Algorithm 1 steps.

Line	Description
1	Initialisation: Pre-allocate arrays for coverage, average throughput, and constraint flags across all individuals. This avoids repeated memory allocation during optimisation.
2	Population loop: Iterate over each candidate solution in the population matrix X , where each row encodes a complete UAV configuration.
3	Reshape candidate: Convert the flattened decision vector into an $N_{\text{uav}} \times 3$ matrix of (x, y, h_{rel}) triplets for geometric evaluation.
4	Terrain lift: The function adds DEM elevation $\mathcal{T}(x, y)$ to each UAV's relative altitude, producing absolute coordinates used in subsequent signal computations.
5	UAV–UAV mesh: Constructs the UAV connectivity graph using pairwise distance computation. Each unique UAV pair (u, v) is tested for hard line-of-sight blocks, distance through foliage and Fresnel clearance. If LoS is clear, received power is estimated using approach outlined in section 3.2.3. Valid bidirectional links are stored in an adjacency list as (v, RSSI_{uv}) , forming the weighted UAV–UAV mesh used for multi-hop routing.
6	Backhaul throughput: Searches the UAV mesh via breadth-first traversal to each backhaul node. The minimum RSSI along a path defines its bottleneck. Throughput is calculated using the methodology in Section 3.2.4.
7	Ground-node evaluation: Checks every GN against all UAVs. For valid LoS links, it evaluates the best throughput on the chosen bandwidths and returns the maximum rate. End-to-end throughput is $T_g = \min(T^{GN}, T^{BH})$.
8	Coverage objective: Assign $f_1 = - \mathcal{S} $, where \mathcal{S} is the set of ground nodes with non-zero end-to-end throughput.
9–12	Throughput objective: Compute $f_2 = -\frac{1}{ \mathcal{S} } \sum_{g \in \mathcal{S}} T_g$ if coverage is non-zero, otherwise set $f_2 = 0$.
13	Constraint: Flag infeasible solutions when coverage falls below the required minimum, $G[i] = \mathbf{1}[\mathcal{S} < \text{MIN_COVERAGE}]$ (set to 2).
14	Return: Stack both objectives into matrix $F = [f_1, f_2]$ and return (F, G) to the NSGA-II optimiser for non-dominated sorting and selection.

NSGA-II configuration

The optimisation uses the NSGA-II evolutionary algorithm, well suited to the non-differentiable and multi-modal landscape produced by the terrain-aware signal and throughput models. Each generation evaluates all candidate solutions through the custom evaluator described in Algorithm 1, and the resulting Pareto fronts capture the trade-off between coverage and throughput.

Algorithm parameters. Table 4 summarises the NSGA-II settings used in this work. These parameters are the default NSGA-II settings provided by the `pymoo` implementation and were sufficient for the optimisation runs in this work.

Table 4: NSGA-II configuration parameters.

Parameter	Value
Population size	100
Generations	20
Initialisation	Uniform random, seed = 1
Crossover operator	Simulated binary crossover (SBX)
Crossover probability p_c	0.9
Crossover distribution index η_c	15
Mutation operator	Polynomial mutation
Mutation probability p_m	$1/n_{\text{var}}$
Mutation distribution index η_m	20
Selection method	Binary tournament with crowding distance
Implementation	<code>pymoo</code> v0.6.1.2

Convergence behaviour and the resulting Pareto fronts are presented in Section 4.2.

Time complexity and Optimisations

Each NSGA-II generation has two main costs: (i) the internal nondominated sorting and selection, and (ii) the external evaluation of each candidate solution. The sorting stage follows the NSGA-II complexity of $O(MP^2)$ for M objectives and population size P [27]. In practice, however, the runtime is dominated by the evaluator in Algorithm 1, which performs terrain-aware LoS checks and throughput calculations for every candidate. Table 6 summarises the per-stage asymptotic costs.

Table 6: Asymptotic time complexity for one NSGA-II generation.

Stage	Complexity
UAV–UAV graph build (LoS + distance)	$O(N_{\text{uav}}^2)$
Backhaul throughput (BFS + LoS checks)	$O(N_{\text{uav}}(E + N_{\text{BH}}))$
GN evaluation (LoS + throughput)	$O(N_{\text{uav}}N_{\text{GN}})$
Evaluator (per individual)	$O(N_{\text{uav}}^2 + N_{\text{uav}}N_{\text{GN}} + N_{\text{uav}}N_{\text{BH}})$
Evaluator (per generation)	$O(P(N_{\text{uav}}^2 + N_{\text{uav}}N_{\text{GN}} + N_{\text{uav}}N_{\text{BH}}))$
NSGA-II sorting + selection	$O(MP^2)$
Total per generation	$O(P(N_{\text{uav}}^2 + N_{\text{uav}}N_{\text{GN}} + N_{\text{uav}}N_{\text{BH}})) + O(MP^2)$

3.2.6 Visualisation Overview

Interactive 3D visualisation is implemented using Plotly to examine UAV positions, connectivity links, and terrain profiles. Each candidate solution can be visualised to validate signal paths and network topology. Visual analysis is also used to identify clusters, dead zones, and redundancy in placement.

Additional layers display the Fresnel zones for each connection type, and tool tips for each node give detailed data on the throughput, signal strength, meshing and LoS limitations. These visualisations support both qualitative analysis and verification of network connectivity.

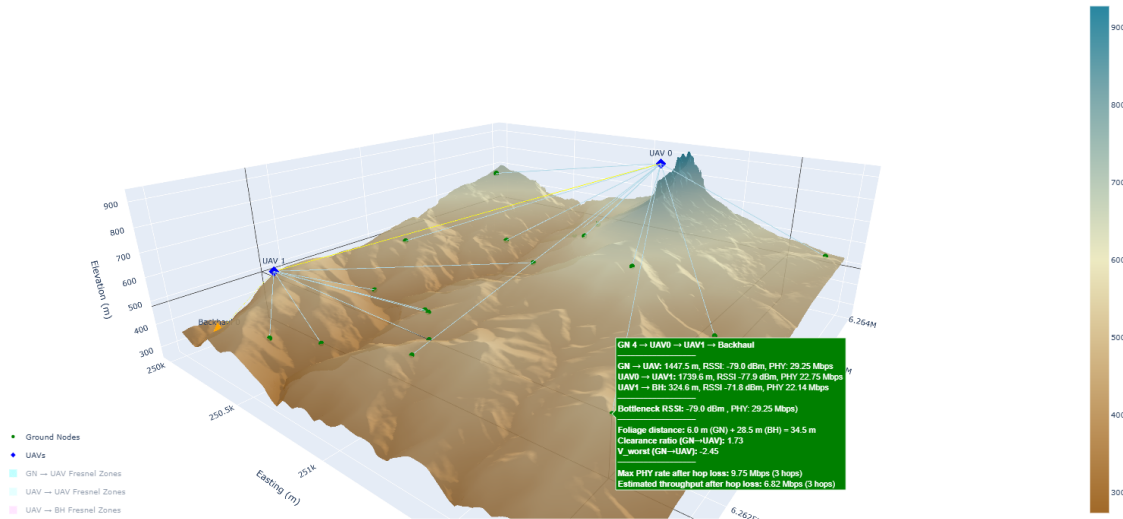


Figure 21: Example of interactive tooltips in the 3D visualisation, showing per-hop RSSI, PHY rate, and MCS details.

4 Results and Discussion

This section presents the key findings from both the Wi-Fi HaLow field testing and the multi-UAV placement algorithm. The aim is to show how real ground-to-ground and ground-to-air measurements inform the propagation model, and how this model affects UAV placement decisions over real terrain.

The results discuss HaLow performance in varied conditions, comparison of measured values against the proposed signal model, and analysis of the optimiser's outputs. The findings presented demonstrate the feasibility, limitations and trade-offs of HaLow-based UAV FANETs.

4.1 Wi-Fi HaLow Testing Results

This section presents the Wi-Fi HaLow performance measured with the HaLowLink-1 evaluation kits. The aim is to access the achievable range and throughput for G2G and G2A links under realistic deployment conditions, and to compare these results against the path loss and throughput model introduced in Section 3.2. The testing locations chosen for this section allow us to assume no foliage attenuation ($L_{\text{foliage}} = 0$) and calculate knife-edge diffraction loss ($L_{\text{diffraction}}$) based on the recorded elevations.

For each dataset, a max-aggregation approach was used to combine repeated measurements at the same distance. Selecting the best-performing sample emphasises the upper bound of achievable performance and reduces the influence of transient interference, noise spikes, and other un-modelled fluctuations.

Across all tests the radios were configured as outlined in the Section 3.1. Figure 22 shows the captured on site setup.

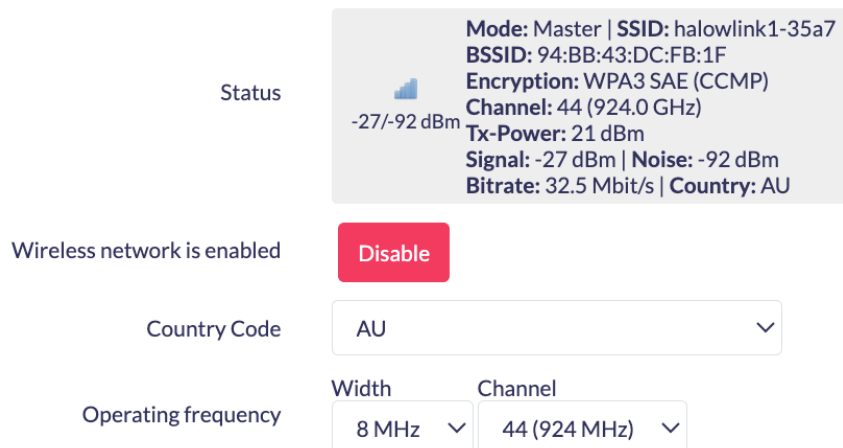


Figure 22: Status snapshot at short range, confirming configuration and noise floor.

4.1.1 Ground-to-Ground Testing

Test site and link geometry

The ground-to-ground (G2G) range testing was conducted along the coastline between Long Reef and Narrabeen Beach. The fixed (remote) node was mounted on top of Longreef headland, while the mobile (local) node was mounted on a tripod at ground level. The local node was moved along the shoreline following the upper side of the dune up to 3.2 km. Figure 23 shows the GPS track of all test points overlaid on satellite imagery, with each marker corresponding to a measurement location.

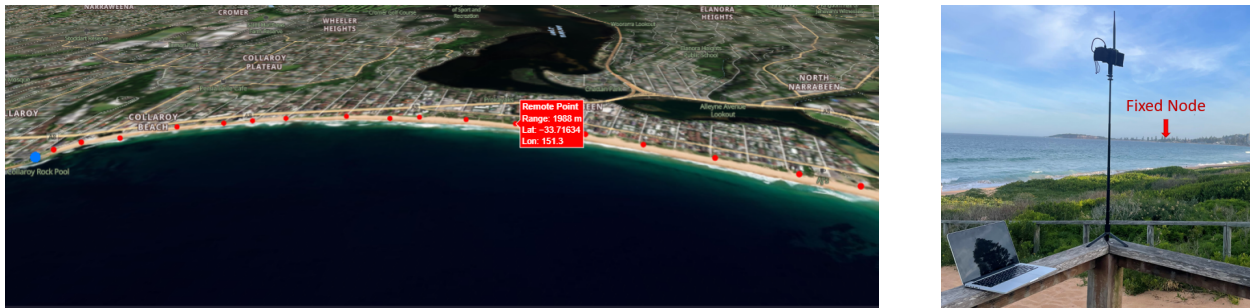


Figure 23: Ground-to-ground Wi-Fi HaLow range testing environment. (Left) Annotated map of test locations. (Right) Remote HaLow node setup at the highlighted remote point.

The beach environment provides predominantly line-of-sight propagation over water and sand, with low dunes and occasional beach access structures introducing minor obstructions. As such, these tests approximate LoS links in a low-to-moderate noise environment. The main limiting factors during testing were pedestrians occasionally entering the Fresnel zone near the receivers and low antenna elevation causing increased ground interference beyond 1.4 km. These effects were mitigated by selecting locations with raised sand banks and ensuring clear Fresnel clearance wherever possible.

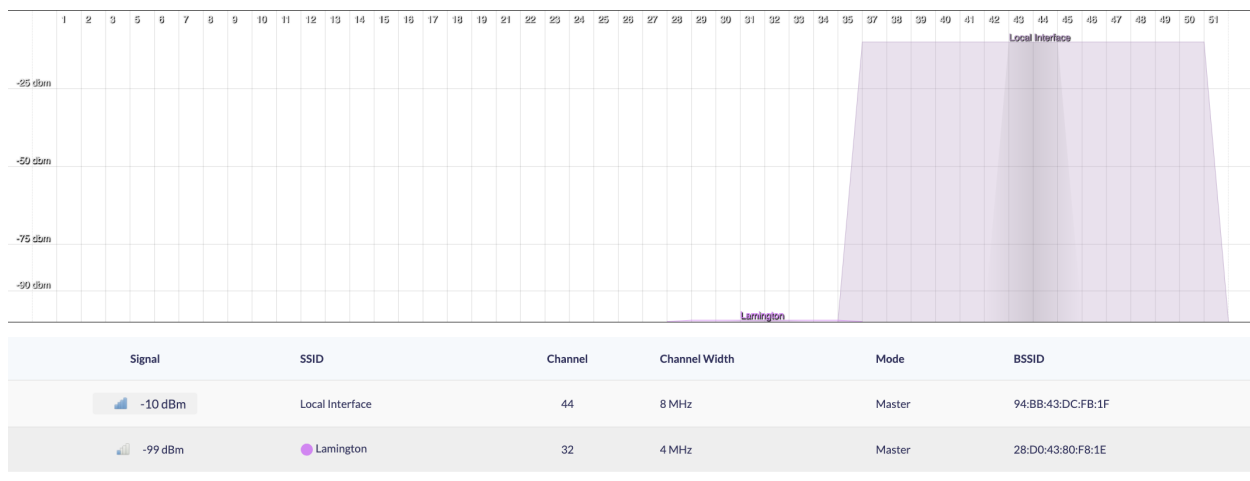


Figure 24: Measured spectrum from 900-952 MHz at the test site, showing the selected HaLow channel and weak narrowband interference around channel 32.

Channel survey, noise and configuration

Before performing the range tests, a wide band spectrum analysis was conducted from 900 MHz to 952 MHz at the remote node. Figure 24 shows the measured received power across this band. Apart from the selected HaLow carrier, the spectrum is largely quiet, with a single narrow interferer seen at channel 32 (4 MHz wide) with a signal of -99 dBm. Given the low signal strength, this interference should be insignificant for most of the link.

Noise levels along the Long Reef-Narrabeen corridor were generally low and stable, with outliers over specific ranges. Figure 25 shows the noise floor reported by the HaLowLink1 radios at each test point, and highlights how the remote kit remained consistent throughout the experiment. Results show a median noise of -89.5 dBm and fluctuations of ± 2 dBm, indicating the absence of sustained interference events at the fixed node.

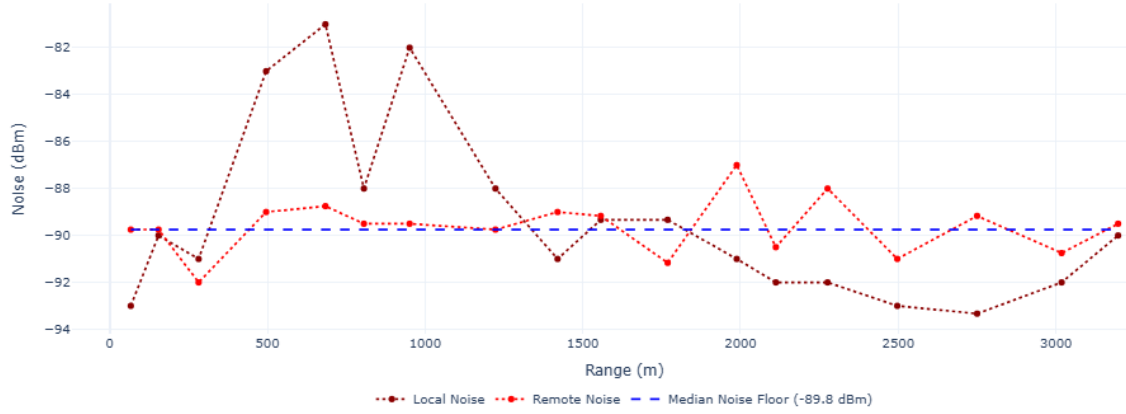


Figure 25: Measured noise floor along the Long Reef-Narrabeen test route.

In contrast, the local kit experienced greater variability. Between 500 m and 1 km, the local noise floor rose to -80 to -82 dBm for several consecutive measurements, suggesting a localised narrowband source. At the northern end of the route, the noise floor decreased with values as low as -93 dBm. These variations align with urban density along the beach.

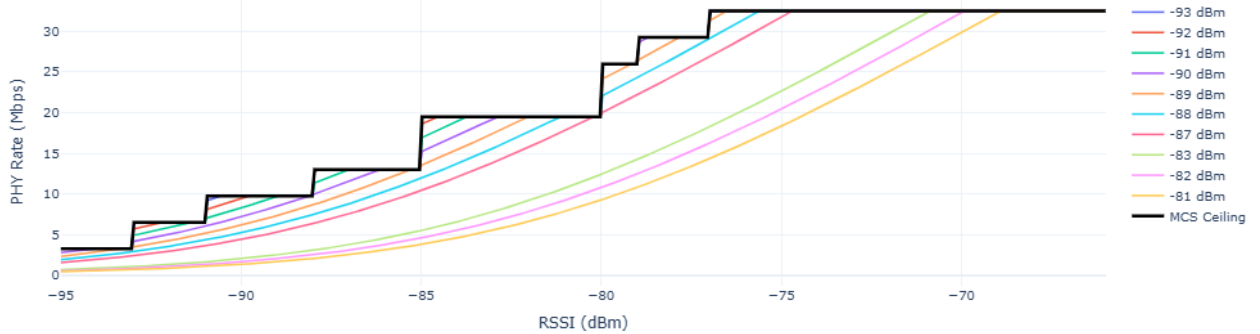


Figure 26: RSSI versus PHY rate for all observed integer noise floors.

At the higher observed noise levels, the PHY rate is limited primarily by the Shannon capacity rather than the 8 MHz MCS ceilings. Higher noise lowers the effective SINR,

reducing achievable PHY throughput and shifting the MCS transition points. Figure 26 illustrates the impact of the measured noise floors on predicted PHY rate. It can also be observed that the 8 MHz configuration remains the dominant channel width for the test location.

RSSI versus range

Figure 27 plots the measured local and remote RSSI against range, along with the theoretical curve derived from the FSPL model. The location specific noise floor is shown as a red horizontal line, indicating the point where communication links fail.

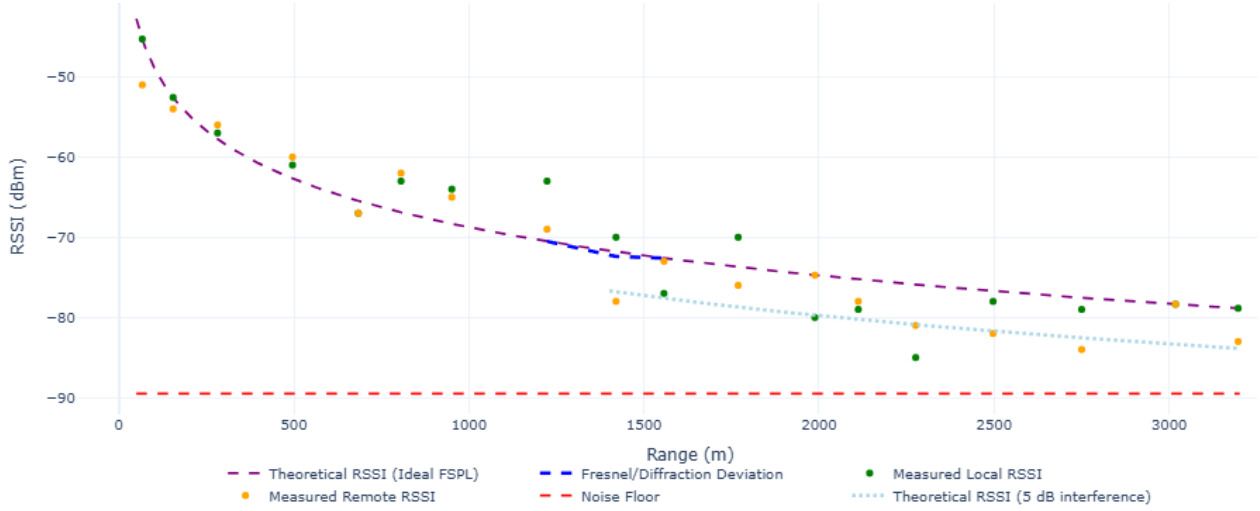


Figure 27: Measured local and remote RSSI versus range for the G2G tests, compared with the FSPL model and interference margin.

Over the first kilometre, the measured RSSI follows the ideal FSPL closely, indicating low environmental losses. Between 500 m and 1.3 km, several points sit a several decibels above the ideal FSPL curve. This behaviour indicates some level of constructive interference is being observed due to ground reflections, or that there are potential calibration offsets between the model and the hardware due to enabling v4.3FEM.

Beyond 1.4 km, the measured RSSI falls below the ideal FSPL. This loss equates to an average environmental interference of 5 dB and reflects the limitations of low-elevation G2G links at longer ranges. As the distance increases, the first Fresnel zone increasingly overlaps the ocean surface, and unmodelled destructive ground reflection and scattering effects introduce additional attenuation compared to the ideal FSPL.

The Fresnel-zone diagnostic in Figure 28 supports this interpretation, as the Fresnel clearance ratio decreases gradually with range. The ground first intersects the first Fresnel zone beyond 600 m and gradually declines to the 60% clearance threshold where it stays for most of the path, with exception of the final test point. Although avoiding the knifes-edge diffraction used in the proposed model, partial Fresnel-zone obstruction still introduces additional loss and accounts for the deviation from the ideal FSPL curve seen in Figure 27. This indicates

that G2G links would require additionally modelling of ground-based interference if included the UAV placement model.

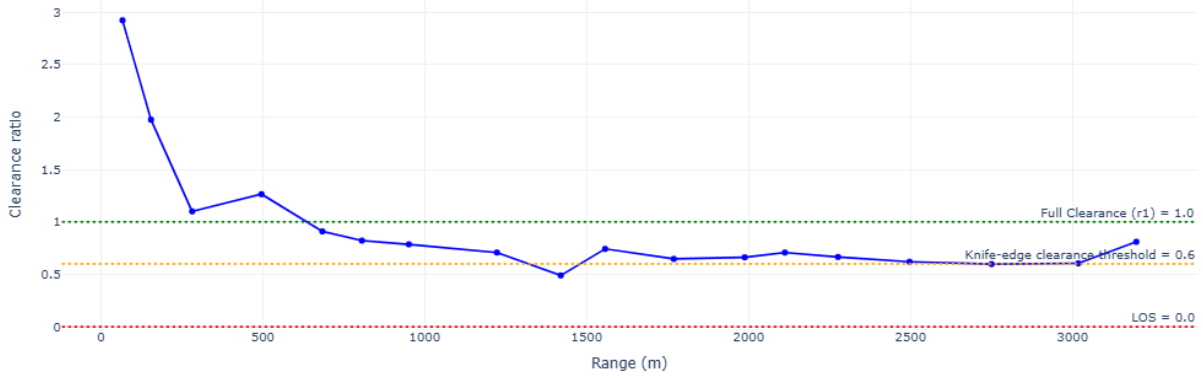


Figure 28: Fresnel-zone clearance ratio for the G2G tests with primary thresholds.

At the longest distances, the measured RSSI approaches the noise floor, and the link operates with very limited SNR margin at MCS 0. Connectivity is still maintained out to 3.2 km, but the TCP tests become unstable. Several runs at the furthest point experienced timeouts or failed to complete the full 10 s interval due to intermittent packet loss. In a lower-noise environment or with narrower bandwidth modes such as 1 MHz or 2 MHz, the same hardware would be expected to sustain the link over longer distances.

Figure 27 also shows that the local and remote RSSI are closely aligned within the first kilometre of the test. Beyond this point, the RSSI gap between the nodes increases by several decibels, aligning with the decrease in ground clearance observed previously, further indicating the importance of clear Fresnel zones.

Overall, the agreement between the model and the measured RSSI supports its use in the subsequent UAV placement experiments, given that environmental interference is correctly tuned.

RSSI, PHY capacity and throughput

Figure 29 compares RSSI with both the modelled PHY capacity and the measured UDP/TCP throughput. Each point represents the bottle neck RSSI at which the measured throughput is achieved. Points are colour-coded by range so that distance trends remain visible in RSSI space and overlaid curves show the modelled PHY ceiling and the corresponding throughput estimate. These curves are modelled using 70% MAC/IP efficiency and a PER of 0.02, consistent with the packet-loss observed during testing.

Real Wi-Fi hardware typically requires several decibels more SINR than the theoretical sensitivity tables predict. Prior measurement studies report a consistent 4–8 dB offset between ideal MCS thresholds and the points at which devices actually change modulation, due to implementation loss and the rapid rise in PER near each MCS boundary [37]. Similar behaviour has been observed in outdoor 802.11ah evaluations, where measured PER

curves and MCS transitions occur several decibels above vendor sensitivities [51].

In this dataset, a 6 dB SNR gap is used to align the modelled MCS boundaries with the measured throughput collapse, matching the behaviour of the HaLowLink-1 hardware.

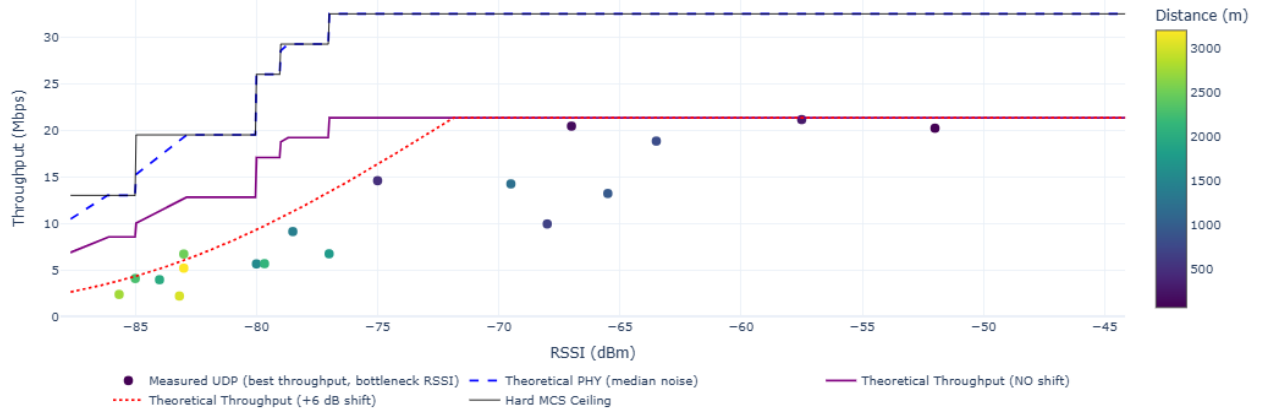


Figure 29: Measured UDP/TCP throughput and modelled PHY capacity versus RSSI for the G2G tests.

At high RSSI, the measured UDP throughput closely matches the model, confirming that the chosen MAC/IP efficiency and PER values capture the protocol overheads. As RSSI decreases, both the measured throughput and the model follow the expected step-like behaviour caused by MCS downgrades. Vertical deviation from the theoretical throughput also indicates early MCS adoption due to high PER, likely caused by environmental variation in the SINR.

Some discrepancies occur in the mid-range, with points between -70 and -60 dBm falling several megabits below the modelled envelope. These points correspond to the high-noise section identified in Figure 25, where the local noise floor rose to -80 to -82 dBm. Although RSSI appears adequate, the elevated noise reduces SINR and lowers the throughput relative to the ideal model. A sparse region also occurs between -76 and -70 dBm, aligning with the 1.4 km point in Figure 27, where a noticeable drop in the measured RSSI was recorded. Additional data points within this range would be greatly beneficial for analysing behaviour around the first MCS threshold.

At lower RSSI values, the measured throughput again aligns closely with the model. Some late-range points even exceed the modelled envelope as the noise floor decreases toward the northern end of the test route, giving the link a slightly higher SINR than the model assumes (Figure 25).

While additional data points in the sparser regions would provide a clearer picture of the precise MCS transition behaviour, throughput is captured well by the Shannon–MCS, model and validates its use later in the optimiser.

UDP and TCP throughput versus range

Figure 30 shows the end-to-end UDP and TCP throughput as a function of range. The plot includes send and receive directions for both protocols, along with the modelled PHY ceiling and the scaled theoretical throughput envelope. The scaled curve incorporates the 6 dB SNR gap from Figure 29) and the 5 dB environmental loss beyond 1.4 km in Figure 27.

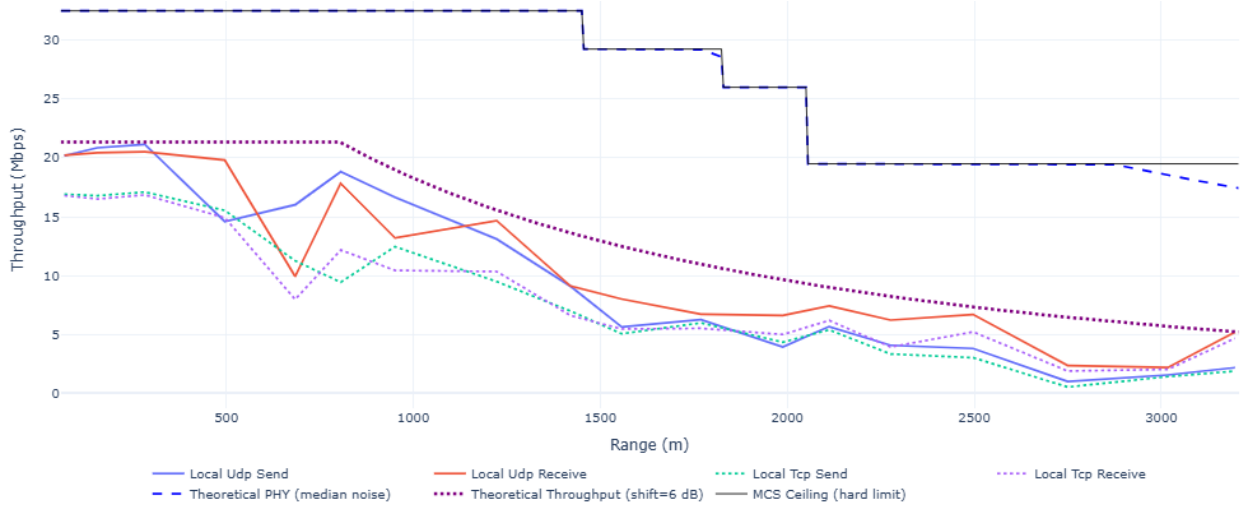


Figure 30: Measured UDP and TCP throughput versus range for the G2G tests.

At short range, UDP throughput closely follows the modelled single-link capacity. TCP remains slightly lower, as expected, due to acknowledgements and congestion control, but still maintains high throughput when RSSI is strong. This behaviour is consistent with the 55% TCP efficiency reported by Morse Micro [61].

As range increases, there is a gradual decline in throughput as the link steps down through lower MCS indices, following the predicted throughput curve. Although following the general MCS trend, there are points at which the MCS index drops prematurely, namely at 700 m under the presence of high noise, and between 2.7 and 3 km where ground based interference and low SNR effects the signal. At the final test point, the measured throughput aligns the modelled value, as clearance is improved by mounting on a elevated lookout. This highlights the importance of ground clearance on long range throughput and highlights the benefits of aerial links for avoiding terrain based losses.

Despite the environmental challenges, the link maintains usable throughput even when RSSI is only a few decibels above the noise floor. This result is encouraging for the UAV deployment algorithm, as distant links through terrain are likely to operate near these margins.

4.1.2 Drone interference at fixed range

Before performing the main ground-to-air measurements, a controlled experiment was conducted to quantify how additional onboard radios affect the HaLow link budget. All tests were performed at a fixed separation of 40 m between the two HaLow nodes, using the following configurations:

1. Both HaLow kits placed on tripods on the ground (baseline).
2. One HaLow kit mounted on the drone with both the 915 MHz and 2.4 GHz telemetry links active.
3. One HaLow kit mounted on the drone with only the 2.4 GHz telemetry link active.

Figures 31 and 32 summarise the measured noise floor, RSSI, and resulting UDP/TCP throughput across these three configurations.

Noise floor and received signal strength

Figure 31 shows that the G2G baseline noise floor sits at roughly -92 dBm and -94 dBm for the remote and local receivers. When either UAV platform is powered and hovering, the remote HaLow node consistently records a 4 dB rise in noise at the remote node, corresponding to platform based interference. Noise at the ground receiver however shifts depending on the telemetry configuration.

The most significant change occurs when the 915 MHz telemetry radio is enabled. In this mode the local HaLow receiver's noise floor climbs to around -82 dBm, clearly deviating from the baseline and the 2.4 GHz configuration. Given no similar change is observed in the 2.4 GHz link, the increase can be attributed to near-band emissions from the 915 MHz transmitter.

This behaviour is also reflected in the received signal strength. With the 915 MHz telemetry active, the drone-side RSSI drops to approximately -93 dBm. By comparison, the 2.4 GHz configuration and the ground-only baseline show much healthier levels of -49 dBm and -45 dBm. The combination of reduced received power and a higher noise floor produces a substantial SNR penalty for the 915 MHz setup.

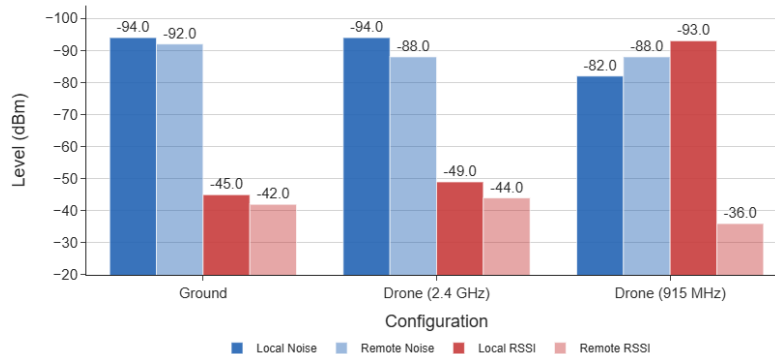


Figure 31: Noise floor and RSSI measurements at 40 m for the three test configurations.

Throughput impact

The consequences for throughput are immediate. With the 915 MHz telemetry enabled, both UDP and TCP performance fall, reflecting the sharp drop in SNR. Once the telemetry is disabled, UDP stabilises at around 22 Mbps and TCP at 17 Mbps to 18 Mbps, aligning with the expected short-range performance for the 8 MHz HaLow channel and the ground results.

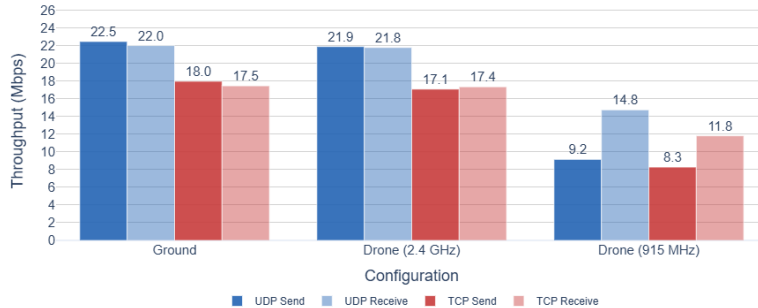


Figure 32: UDP and TCP throughput across the three configurations at 40 m.

Implications

Overall, the results demonstrate that the 915 MHz telemetry radio introduces substantial interference when mounted alongside the HaLow hardware on the drone. The elevated noise floor, weaker drone-side RSSI and large throughput deficit are all consistent with receiver desensitisation caused by the near-band telemetry transmitter. The 2.4 GHz telemetry system does not exhibit these effects, only experiencing platform induced noise increase and therefore will be used for telemetry in the G2A trials.

4.1.3 Ground-to-air testing

Test site and link geometry

The ground-to-air (G2A) tests were carried out at Centennial Park (Brazilian Fields). One HaLowLink-1 node was mounted on the drone, and the other was installed on a tripod at ground level. During each trial the drone hovered at a fixed altitude of approximately 10 m above ground level while maintaining line-of-sight (LoS) to the ground node, which was repositioned to achieve the desired separation range.



Figure 33: Ground-to-air Wi-Fi HaLow range testing environment at Centennial Park. (Left) Annotated map of test locations. (Right) HaLowLink-1 node mounted on the airframe.

Figure 33 shows the test locations of the drone and ground node overlaid on satellite imagery, and the aerial HaLow node installation. Each marker on the map corresponds to a range test location.

The field provides an open, unobstructed LoS corridor between the ground station and the UAV at all tested ranges. Compared with the Long Reef–Narrabeen G2G route in Section 4.1.1, the G2A geometry avoids ground-induced Fresnel obstruction, but introduces platform dynamics such as drone attitude changes, rotor motion and shifting antenna polarity.

Channel conditions, noise and configuration

At Centennial Park, both HaLow nodes experienced stable noise floors throughout testing. The ground node measured values around -94 dBm (± 1 dB), while the drone node sat consistently around -90 dBm (Figure 34). The UAV noise levels are comparable to the Long Reef–Narrabeen tests, where the median noise floor was -89.5 dBm (Figure 25). Figure 26 shows the effect of the noise floor on shifting the MCS curve for the observed noise values.

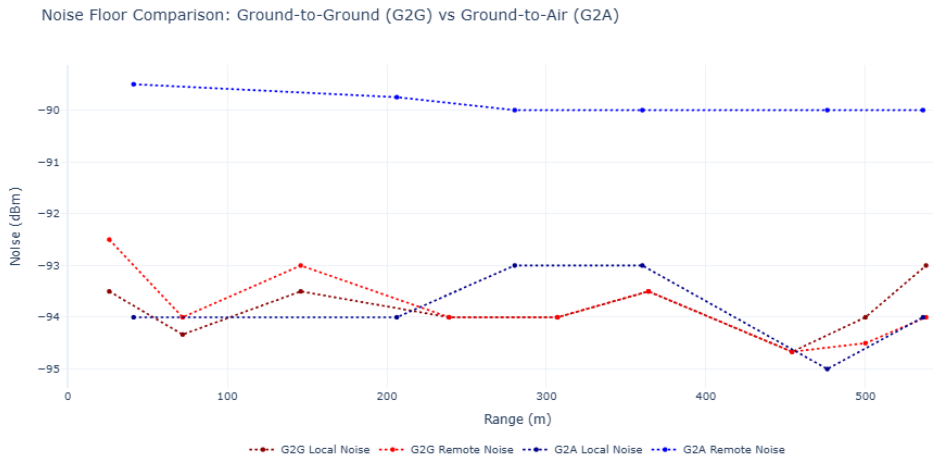


Figure 34: Measured noise floor at Centennial Park for the ground and drone HaLow nodes.

The drone's noise floor is consistently several decibels higher than the ground node, which is expected for small UAV platforms and is likely due to antenna misalignment from roll, pitch and yaw, as well as rotor and frame-induced fading that alters the local radiation pattern. Together, these effects raise the effective receiver noise floor and reduce SINR compared with an equivalent ground-based setup.

Short spectrum sweeps around the 924 MHz centre frequency did not reveal any persistent narrow band interference at the site.

RSSI versus range

Figure 35 compares the G2A RSSI measurements with the corresponding G2G results collected at the same site. A secondary theoretical RSSI is included using a 5dBm of environmental interference.

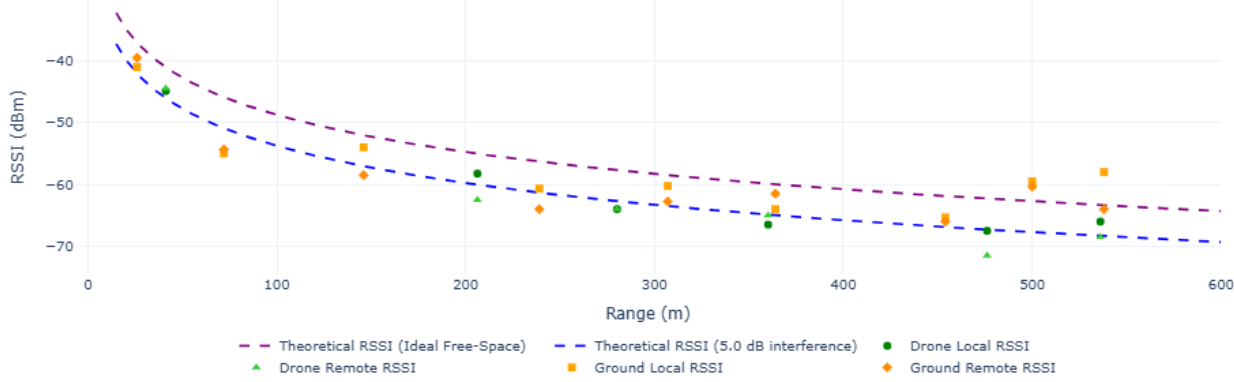


Figure 35: Measured local and remote RSSI versus range at Centennial Park.

To separate geometric effects from noise related factors, the Fresnel clearance ratio is plotted in Figure 36. The G2A path maintains full first-Fresnel clearance across the entire range, whereas the G2G path shows ground interference is present and of similar magnitude to the Longreef G2G tests.

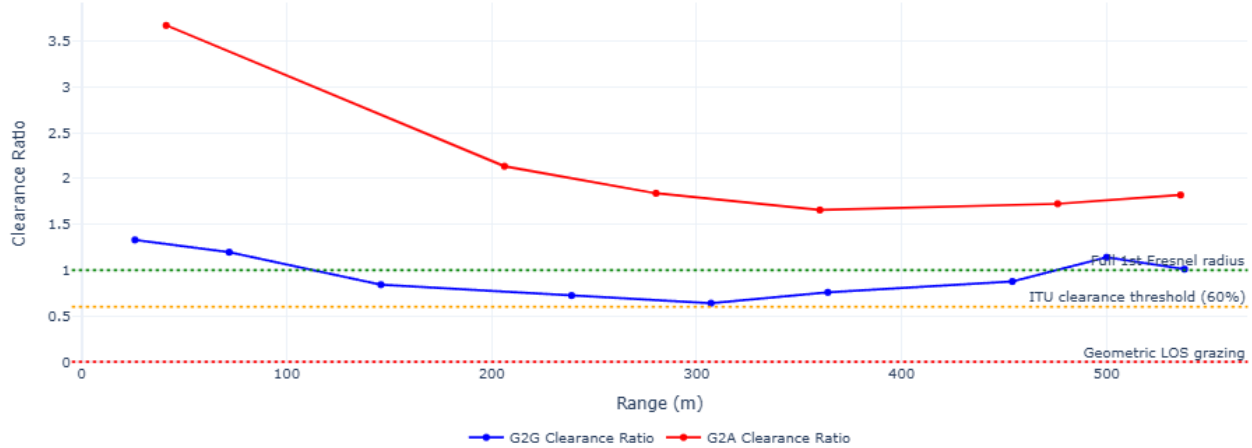


Figure 36: Clearance ratio of first fresnel zone for G2G and G2A tests.

Across the 0–550 m range, both G2A and G2G links follow modelled RSSI, with both curves sitting approximately 5 dB below the free-space model. For G2G, this matches the behaviour observed in the Long Reef–Narrabeen tests and can be attributable to reduced ground clearance. In contrast, the G2A deficit arises from the platform interference.

A notable outlier occurs at 476 m, where the G2A RSSI is roughly 3 dB below the adjusted curve. This point aligns with a measured increase in measured narrowband interference at the drone node and can be considered as an outlier. This results in a reduced SINR and lower recorded RSSI.

These observations highlight the need for further investigation into drone related interference and methods to mitigate it in order to improve HaLow performance in aerial deployments.

RSSI, PHY Capacity and Throughput (G2A comparison with G2G)

Figure 37 plots each remote and local pairs throughput as a function of bottleneck RSSI for both the G2A and G2G tests. Two theoretical throughput envelopes are included to model the ground and drone noise floors (-94 dBm and -90 dBm). Both envelopes use the 6 dB SNR gap introduced in Section 4.1.1, which aligns the modelled MCS boundaries with the measured transitions.

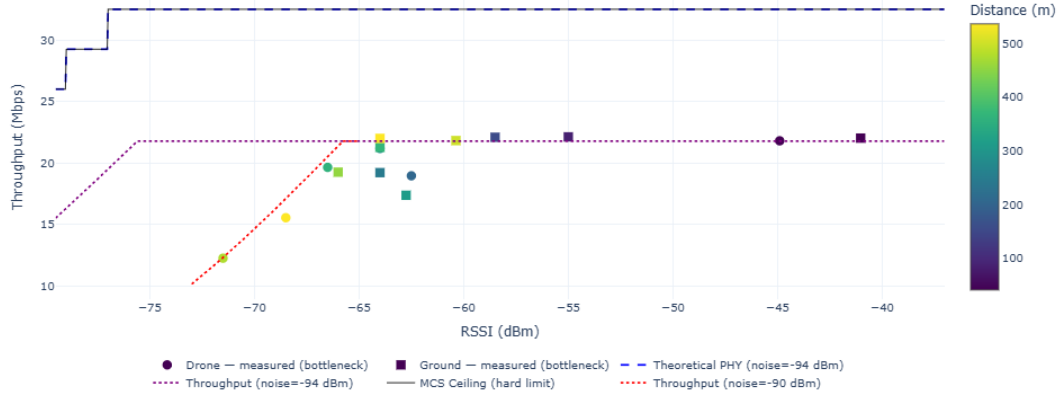


Figure 37: RSSI vs Bottlenecked throughput for G2G and G2A tests.

Over the test range, the G2A points track the throughput envelope well and encounter the MCS transition thresholds earlier than the G2G link as predicted. This behaviour is most apparent in the -73 to -65 dBm region, where the Shannons capacity causes high packet error rate and triggers early rate downgrades. It's important to note that due to the variability of platform interference, large SINR dips due to accumulative effects can contribute to transitions much earlier than the modelled curve. This can be observed at -63 dB, where the drone throughput is does not match what a stable RSSI should allow.

The G2G result in comparison are seen to remain close to the 22 Mb capacity modelled for the test range. A small drop in throughput is observed around the -66 to -63 decibel range, aligning with clearance based losses and showing how even with strong RSSI, ground interference can cause high PER and result in early MCS downgrades. This is confirmed, as when clearance increases again, G2G results return to the theoretical maximums, even with a lower RSSI.

Overall, the G2A and G2G measurements follow their respective throughput envelopes closely, confirming that the combined Shannon–MCS model captures the behaviour of both links across the measured range. The agreement also supports the magnitude of the SNR gap applied in the model, which remains consistent with the Long Reef G2G results.

While the measured points align well with the model across the available range, the dataset does not extend to sufficiently low RSSI values to assess the G2A link near the sensitivity limit. Additional measurements at longer ranges would help determine whether the same SNR gap and rate-adaptation behaviour hold when the airborne link operates with very limited SINR margin.

UDP and TCP throughput versus range (G2A comparison with G2G)

Figure 38 compares the end-to-end UDP and TCP throughput against range for the Centennial Park G2G and G2A tests. The figure overlays the measured send and receive throughput for both protocols with the FSPL derived PHY ceiling and the scaled theoretical UDP throughput envelope. The theoretical envelope uses the same PHY model as Section 4.1.1, with a 6 dB SNR gap, 5 dB of environmental interference, and MAC/IP efficiency applied. Regardless of the noise floor chosen, the envelope is approximately 22 Mbps over the plotted range.

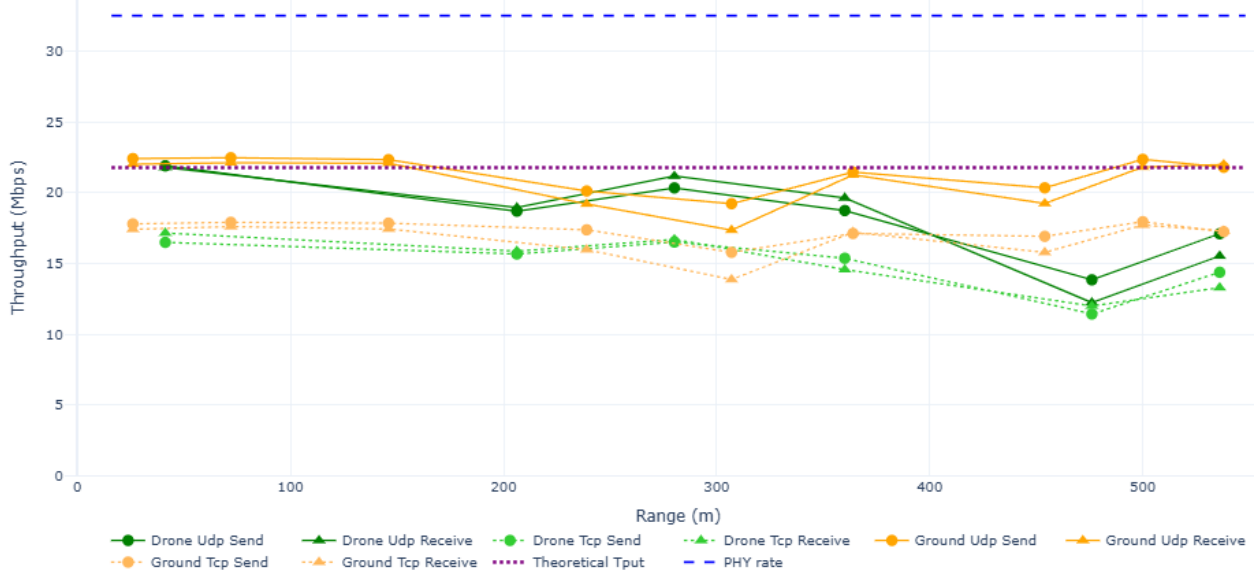


Figure 38: UDP and TCP Throughput vs Range for G2G and G2A tests.

Up to around 350-400 m, both the G2G and G2A links track the theoretical envelope closely. UDP throughput sits between 19 and 21 Mbps, and TCP remains slightly lower at around 15-17 Mbps due to acknowledgements and congestion window behaviour. This is consistent with the 70% and 55% PHY efficiencies observed in the Long Reef-Narrabeen G2G tests and on the Morse Micro website [61]. In this region, the behaviour of the G2A link is similar in performance to the G2G case, indicating that neither the aerial platform nor the drone-side noise floor is a limiting factor at short to moderate ranges.

Differences emerge near the longest test separations. At 454 m, the ground link achieves an average UDP throughput of approximately 20.3 Mbps and TCP throughput of 15.8 Mbps, very close to the modelled single-link capacity. At the comparable G2A point at 476 m, the drone-mounted link achieves only ≈ 13.1 Mbps UDP and 11.9 Mbps TCP. This corresponds to a reduction of roughly 40% in UDP throughput and 25% in TCP throughput relative to the G2G case. The reported PHY rates reflect the same behaviour, with the G2G node reporting a HaLow bitrate of 32.5 Mbps, while the drone reports 26–29 Mbps, indicating that the link was operation 1-2 MCS levels lower for the G2A link.

The reduced performance is consistent with the lower RSSI observed in Figure 35 and the

drone's higher noise floor. Together, these factors reduce the available SINR margin at the UAV, requiring the device to drop to more robust modulation schemes to maintain a connection. This results in the early divergence of throughput in Figure 37

This behaviour is also reflected in the MAC-layer statistics in Figure 39. The G2G link maintains a round-trip success rate of roughly 93-95%, while the G2A link falls to 78-88% at the longest separations. The lower success rates identified is due to a larger number of retries and ACK timeouts. Notably, this can be seen to primarily effect the RTS of the kit mounted to the drone, further showing the effect of the aerial platform and its higher noise.

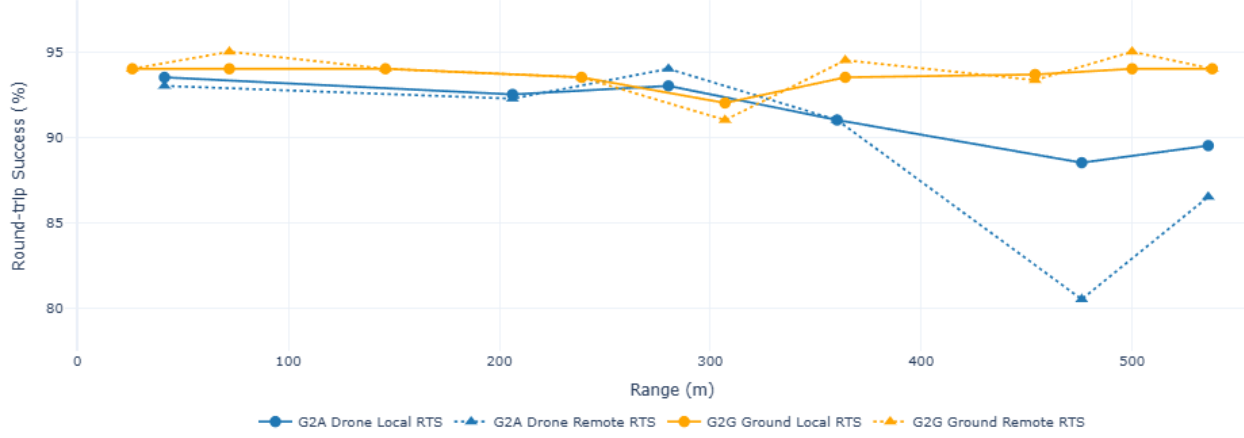


Figure 39: MAC-layer round-trip success rate versus range for the G2G and G2A tests.

However, when compared with the Long Reef G2G tests, which were conducted in a similar noise environment, the G2A throughput shows promising results. At equivalent ranges, the G2A throughput are similar, and in some cases higher than the G2G measurements due to lack of ground interference. This suggests that, aside from the airborne noise penalty, the underlying link behaviour is consistent between G2G and G2A links for the tested G2A ranges.

However, the Centennial Park site only allowed for testing out to 550 m, whereas the Long Reef tests demonstrated stable single-hop performance up to 3 km. Longer range G2A measurements are therefore needed to evaluate the aerial link at extreme distances and confirm whether the same throughput envelope and MCS-transition behaviour continue to hold. In addition, only two repetitions were possible at each G2A distance due to flight-time constraints. More repeats, smaller range increments, or continuous logging would help separate UAV specific effects from run-to-run variability. In particular, this would be useful in better determining MCS thresholds and evaluating the impact of SINR fluctuations. Nevertheless, the present results show that UAV-mounted HaLow links remain consistent with the calibrated model and that their primary constraint at longer ranges is the reduced SINR due to platform interference.

Implications for UAV relay links

For the multi-UAV placement and routing problem considered later in this thesis, these observations mainly affect how the calibrated link model is parameterised rather than structure. The G2A results confirm that UAV-mounted HaLow links follow the same RSSI to throughput relationship and MCS behaviour as G2G links, but with a small throughput reduction arising from the higher airborne noise floor and RSSI.

These effects can be incorporated into the optimisation framework by raising the environmental noise floor by 4dB for UAV receivers, and tuning the environmental interference parameter to match the 5db shift seen in the G2A results. While this adjustment is minor over the G2A ranges tested, it should reduce performance of the model at longer distances and within the UAV mesh.

4.2 Algorithm Results

This section presents the results of the NSGA-II optimiser described in Section 3.2. The goals are to evaluate how well the optimiser navigates the terrain aware HaLow model, analyse convergence behaviour, and interpret the resulting UAV placements over the DEM. All results are simulation based using the real terrain model and the calibrated HaLow throughput model from the Section 4.1.

4.2.1 Scenario configuration

The optimisation was evaluated on a DEM region corresponding to Katooba region, namely the hiking trails near the 3 sisters. This was sourced using the ELVIS database introduced in Section 3.2 and had a resolution of 1m. This area was chosen due to the low noise floor, notable elevation and topographic variation, and the high frequency of lost tourists and SAR operations in the area.

4.2.2 Experimental Setup

The optimisation was performed over a 2×2 km region with a single centrally placed backhaul node and $N_{GN} = 20$ randomly distributed ground nodes. Three UAVs ($N_{UAV} = 3$) were optimised within the area, with altitude bounds of 30-100 m above local terrain height to ensure tree clearance and operational within operational limits. A uniform tree height of 10m and global noise floor of -95 dBm was used for the search area. Each link was evaluated using the signal model stack in Section 3.2 and the calibrated HaLow PHY-to-throughput mapping from Section 4.1. The NSGA-II configuration follows the parameters selected in Section 3.2. These settings serve as the default configuration, variations to parameters may be used to examine specific behaviours, and will be stated in the relevant sections.

4.2.3 NSGA-II Convergence Behaviour

Figure 40 shows hypervolume convergence over 50 generations, and Figure 41 shows the corresponding changes in throughput and coverage. The optimiser makes larger gains early on, with later generations focused on refining the Pareto front.

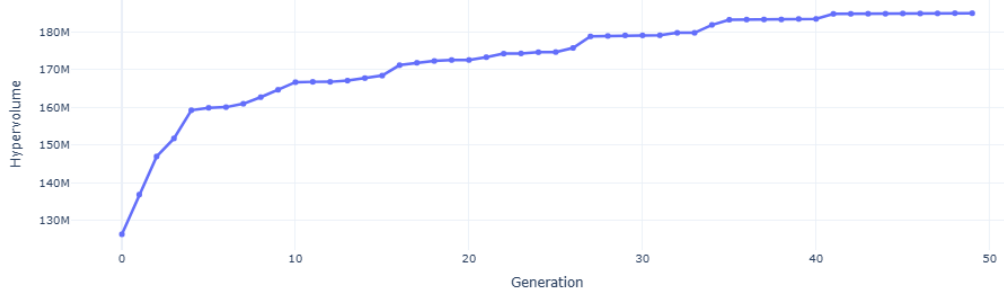


Figure 40: NSGA-II hypervolume convergence across 50 generations.

The hypervolume and throughput objectives rise rapidly during first 10 generations, indicating that NSGA-II quickly identifies the major structural improvements in UAV placement. This would primarily include changing link architecture and switching MCS levels. By approximately 15 generations, both the hypervolume and the individual objective begin to plateau, showing that the algorithm has already discovered a reasonably strong Pareto front.

Beyond this stage, convergence becomes slower and more irregular, with extended flat regions with occasional upward jumps. The increases seen reflect the discrete structure of the evaluation landscape, in which small positional adjustments can cause a link to cross MCS sensitivity thresholds or result in new network as LoS conditions are satisfied. These transitions are seen at generations 28, 34, and 41 (Figure 40). This further emphasises the importance of using a genetics based algorithm, as gradient based optimisers cannot reliably progress in discrete landscapes.

The gradual convergence at the upper end is also influenced by the logarithmic smoothing applied to the MCS steps in Section 3.2. This smoothing accelerates early progress by encouraging individuals to move well into new MCS boundaries, while providing more nuanced, incremental gains further into a MCS tier. Although the smoothing parameter k could be tuned to sharpen late stage optimisation, it would have the inverse effect of undervaluing throughput at the start of a MCS tier. As the optimisers primary task is to determine the correct MCS tiers and viable routes, optimising throughput within a plateau, although crucial, is less important.

From a practical standpoint, the convergence results demonstrate that twenty generations is sufficient to obtain a stable Pareto front for real-time SAR deployment, with each optimisation run taking approximately eight minutes on a single-threaded configuration using consumer grade hardware. Additional generations provide optimisations within the plateaus and provide marginal improvements unless a discrete link transition is discovered. If late generation optimisation is required by responders, evaluation can be parallelised, warm-started from previous UAV placements, or computed externally via the cloud.

Overall, the convergence behaviour in Figures 40 and 41 supports the use of a short optimisation horizons for real-time field operation, while still achieving high quality UAV placements.

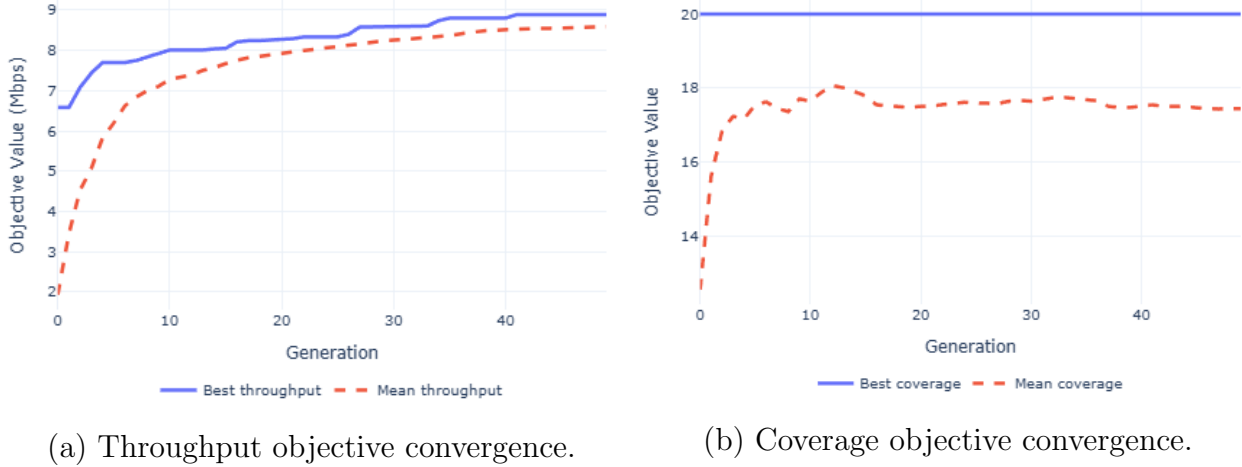


Figure 41: Objective convergence across generations: (a) throughput and (b) coverage.

4.2.4 Pareto Front and Trade-off Analysis

The final non-dominated set obtained by NSGA-II reveals the fundamental trade-off between maximising GN coverage and maximising average end-to-end throughput. Figure 42 presents both the Pareto front and a parallel-coordinates view for the setup in Section 4.2.2.

Across the six non-dominated solutions, GN coverage ranges from fifteen to the full set of twenty nodes, while the average throughput remains tightly grouped between approximately 8.40 and 8.89 Mbps. This shows that the optimiser finds UAV placements that maintain high throughput while discarding only the most difficult ground nodes. The Pareto front has a shallow negative slope, which reflects how increasing coverage requires only a modest reduction in average throughput when a sufficient number of UAVs is supplied. The parallel-coordinates plot supports this behaviour and indicates a well-formed Pareto set without degenerate or isolated solutions.

A similar trend is observed in the two-UAV experiment in Figure 44. In this case the Pareto front covers values from thirteen to eighteen ground nodes with less than one megabit of throughput variation. This again suggests a stable group of near-equivalent solutions. However, when the optimiser attempts to cover all twenty nodes the performance drops sharply to less than three megabits per second, indicating that two UAVs are not sufficient to cover the problem space without a significant throughput penalty. This provides useful information to mission operations, with Pareto fronts highlighting the effectiveness of the number of UAVs available.

Overall, the Pareto structure demonstrates that the UAV topology can be tuned flexibly toward either greater coverage or higher average throughput. This behaviour is advantageous in SAR deployments where mission priorities may shift dynamically, allowing for real-time re-weighting of the objectives without requiring fundamentally different UAV placements.

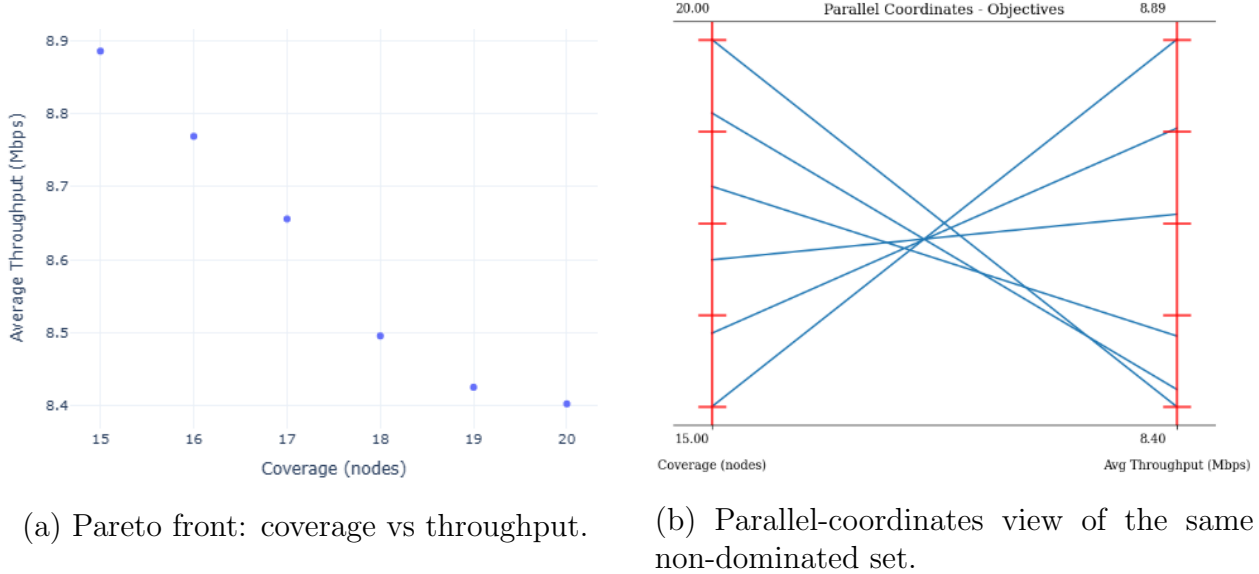


Figure 42: Non-dominated solutions obtained by NSGA-II at the end of the optimisation.

4.2.5 Representative Optimised Deployments

To illustrate how NSGA-II exploits both the terrain geometry and the HaLow throughput model, four representative deployment scenarios are presented in Figure 43. Each case uses the same optimisation pipeline described in Section 3.2 and selects a solution from the final Pareto set that achieves maximal GN coverage, allowing the placement behaviour to be compared directly across different environmental or structural conditions.

The first scenario corresponds to the baseline configuration introduced in Section 4.2.2, providing insight into general UAV placement. It can be seen that UAVs are placed above notable landmarks, such as valleys, ridges or hill tops to maximise coverage range and terrain offset. This also provides clean LoS pathways between air nodes. The following scenarios diverge from this setup by altering of the tuneable variables to evaluating its effect.

The second scenario evaluates how the optimiser adapts when only two UAVs are available. Similar placement is used to the 3 UAV test, identifying the candidate locations as highly optimal coverage locations. Notably, it can be seen that the resulting coverage struggles to maintain a high average throughput seen in the first scenario, indicating that the problem is under constrained.

The third scenario retains the three-UAV configuration but replaces the GN set with a different random seed, isolating how the optimiser handles changes in user distribution while maintaining identical environmental assumptions. Similar UAV placement is observed, with aerial nodes following ridge lines to create communication links over notable terrain elements.

The fourth deployment moves the backhaul to a challenging corner location, forcing UAVs

to account for reduced visibility and route effectively through the UAV mesh. This demonstrates the systems strong capability to establish backhaul connections and coverage in highly constrained scenarios.

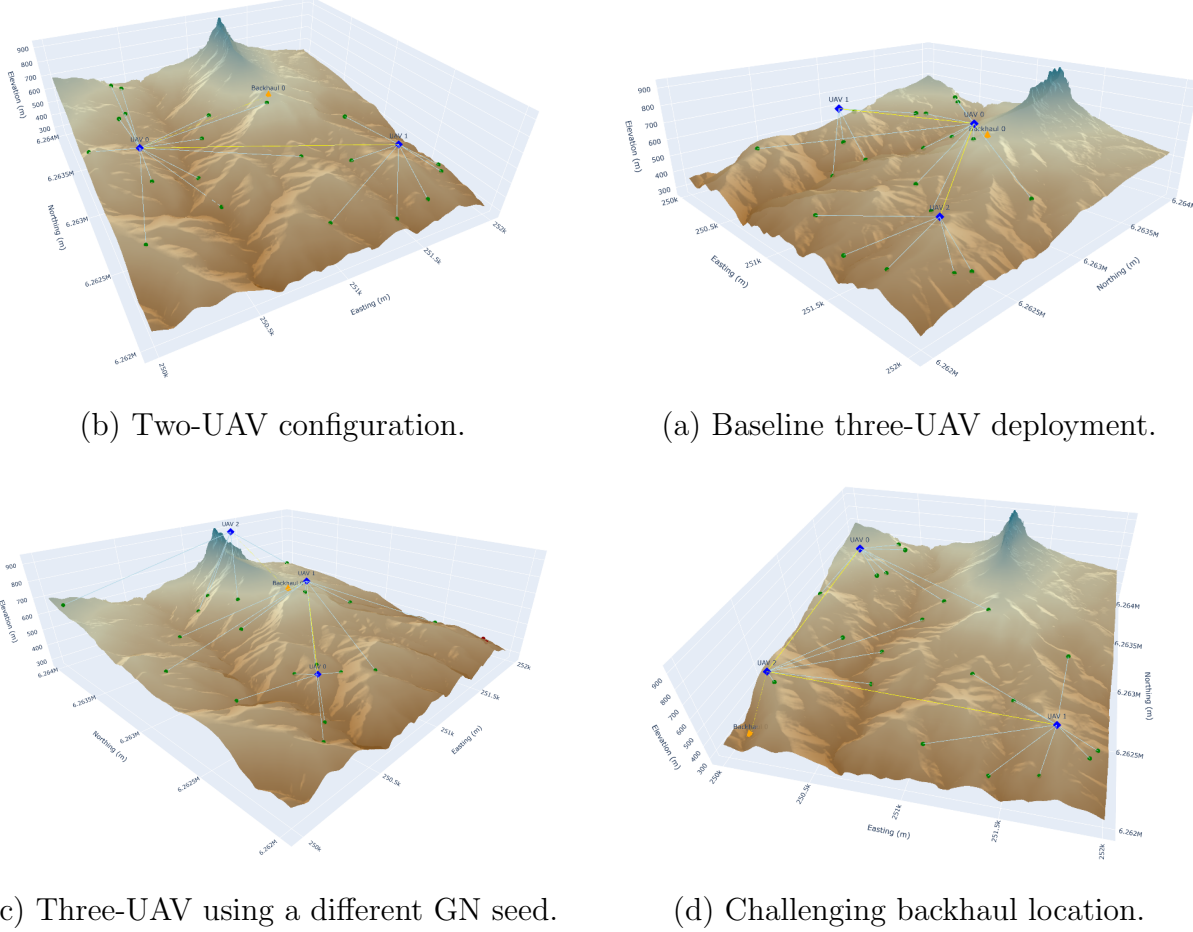


Figure 43: Representative optimised UAV deployments selected from the non-dominated set for four different scenarios.

4.2.6 Stability across optimisation runs

To evaluate the repeatability of the optimisation results, NSGA-II was executed five times using different random seeds. The Figure 43a. setup was used to evaluate performance in under-constrained deployments. Figure 44 overlays the resulting Pareto fronts.

Across all runs, the Pareto fronts align closely, with only minor variation at the extremes of the trade-off curve. This demonstrates that the optimisation problem is well conditioned and that NSGA-II consistently converges toward the same coverage–throughput trade-off surface, even when limited to only 20 generations. The tight clustering of fronts indicates that the resulting solutions are robust and not dependent on the initial population or random seed.

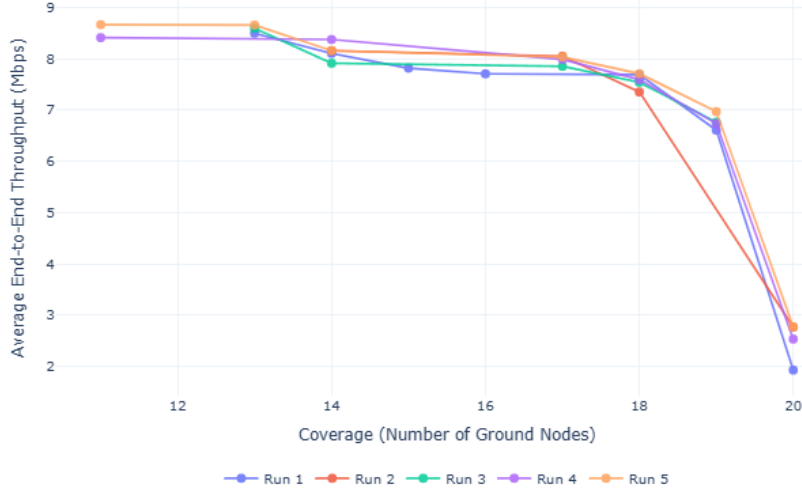


Figure 44: Overlay of Pareto fronts from repeated NSGA-II runs with different random seeds.

4.3 Discussion and Implications for UAV relay design

This section brings together the main findings from the Wi-Fi HaLow tests and the NSGA-II optimisation and links them to the research gaps in Section 2.5. The measurements address the lack of real world data for HaLow links in outdoor and aerial settings, while the optimisation results address the need for a terrain aware deployment method that is tuned to search and rescue operations.

The Long Reef ground to ground experiments in Figures 27, 29 and 30 show that HaLow can maintain useful throughput over several kilometres in a mostly line of sight coastal environment when interference is low. The measured RSSI tracks the corrected FSPL model closely until the Fresnel zone begins to graze the ground, and the observed throughput follows the combined Shannon and MCS envelope once a single SNR gap is applied. The fixed range drone interference tests in Figures 31 and 32 then show how platform specific radios can degrade performance by raising the noise floor and desensitising the HaLow receiver. Finally, the Centennial Park ground to air results in Figures 35, 37 and 38 demonstrate that airborne links follow the same general RSSI versus throughput relationship as ground links, but with a small penalty at longer ranges due to the higher noise floor and more frequent MAC level loss. Together, these plots show that a single measurement driven link model, with appropriate noise and margin terms, can represent both G2G and G2A links over the ranges tested.

The optimisation study builds directly on this calibrated model. In the representative layouts in Figure 43, the optimiser places UAVs on ridges and elevated plateaus that provide good visibility to both the backhaul and nearby ground nodes. These positions emerge from the line of sight, Fresnel and foliage checks in the evaluation pipeline and align with practical intuition about placing relays on high ground. Changing the number of UAVs, moving the backhaul, or resampling the ground node set produces new layouts that still favour terrain features with strong backhaul access and good sight lines into the valleys.

The Pareto fronts in Figures 42 and 44 summarise the system level trade offs. For three UAVs over a 2km² DEM, coverage and average throughput are only weakly in conflict, with coverage increasing from partial to full while the average per node throughput decreases only slightly. The two UAV case produces a very similar front over the mid coverage range but suffers a large drop in average throughput when forced to serve all twenty nodes. These results indicate that there is a usable operating region where small changes in the number of UAVs, or small changes in coverage, do not dramatically affect average throughput. They also show that there is a clear limit to what a small fleet can provide once the terrain and hop penalties are taken into account. To prevent unrealistic fitting seen in the 2 UAV tests, a minimum throughput could be applied to each node to ensure connects meet the operational requirements.

The convergence and repeatability results in Figures 40 and 41 show that NSGA-II converges to usable deployments quickly, with additional generations mainly refining the final placements. Hypervolume and objective values improve rapidly over the first few tens of generations and then change only when a link crosses an MCS boundary or a ground node reattaches to a different UAV. The repeated runs in Figure 44 produce tightly clustered Pareto fronts for the same scenario, which indicates that the optimisation problem is well conditioned and that the solutions are not strongly dependent on the initial population. This is important for field deployment, since it suggests that short runs are sufficient to obtain useful placements and that recomputing the front as conditions change will give consistent guidance.

Taken together, these results help close the gaps identified in Section 2.5. The measurements provide insight into HaLow range, interference sensitivity and airborne penalties in realistic environments, and supply the parameters needed for a usable propagation and throughput model. The optimisation study then uses this model with a DEM of the Katoomba region to explore how many ground personnel can be covered with a given drone fleet size, where the UAVs should fly relative to the terrain, and how much throughput must be traded to reach additional responders. While not yet validated in a full-scale field deployment, the combined work demonstrates that a measurement-informed NSGA-II framework can generate terrain-aware FANET configurations that are suitable for SAR operations.

5 Conclusion

This thesis investigated the use of Wi-Fi HaLow based Flying Ad Hoc Networks to extend communication coverage for search and rescue operations in challenging terrain. The work combined field measurements using Morse Micro HaLow development kits, a calibrated propagation and throughput model, and a terrain-aware multi-UAV placement algorithm using NSGA-II. Together, these were used to assess the operational range of HaLow links in real world environments and how UAV relays can be positioned to support first responders.

The experimental results showed that Wi-Fi HaLow can deliver stable, megabit-per-second throughput over kilometre-scale ground-to-ground links when the channel is unobstructed and interference is controlled. Ground-to-air tests with a UAV-mounted HaLow node produced similar RSSI–throughput behaviour to the ground links, with only a modest penalty at the longest measured ranges. Controlled interference measurements demonstrated that a co-located 915 MHz telemetry radio can significantly raise the effective noise floor and reduce throughput. For testing, a 2.4 GHz telemetry link was used and shown to have low impact on the HaLow receiver. These findings support the feasibility of HaLow-based relay links for field operations, provided that platform integration and co-channel interference are managed carefully. Using Wi-Fi Halow for UAV telemetry instead of other receivers is also a potential solution to this issue.

The propagation and throughput model developed in this thesis combines free space loss, Fresnel clearance, foliage and diffraction terms with calibrated noise floors and empirically tuned MCS behaviour. Embedding this model inside an NSGA-II framework allowed UAV placements to be optimised over a real digital elevation model of the Katoomba region. The optimisation results showed that UAVs placed on ridgelines and elevated terrain can provide consistent backhaul access to dispersed ground teams, and that the trade off between coverage and average throughput remains shallow when the UAV fleet has sufficient degrees of freedom. The Pareto sets produced across multiple runs were stable and repeatable, demonstrating that high quality deployments can be achieved reliably within short optimisation horizons.

While these findings support the use of HaLow equipped UAVs in SAR environments, limitations of the work should be acknowledged. Optimisation results, although tuned using the G2A and G2G tests, are simulation based and would need to be compared to full multi UAV field trials to validate accuracy. Throughput values should therefore be treated as estimates in SAR pre-planning rather than guaranteed throughput. Vegetation in the model is also assumed to be constant height, and all ground nodes are modelled as static.

Future Work

Future work should close the gap between simulation and field use by testing in environments that more closely match real SAR conditions, improving the reliability of the calibrated HaLow parameters.

Additional G2G and G2A measurements are needed in dense vegetation and forested valleys to validate and refine the foliage loss model used in this thesis. Replacing the assumed constant canopy height and density with site specific vegetation data would provide more accurate estimation of interference and LoS conditions. To better represent movement in the ground nodes, adaptive in flight repositioning could also be incorporated, where UAVs adjust their position between optimiser updates based on real time link quality, helping to maintain connectivity as responders move and reduce the likelihood of links being dropped.

An option for further work would be to explore hybrid architectures that use a satellite uplink on the UAVs instead of meshing back to a fixed backhaul. While large Starlink panels are impractical to mount due to power and size constraints, compact low power satellite terminals are beginning to emerge. These systems could allow UAVs to shadow responder teams independently of other relay nodes, avoiding the multi hop throughput loss associated with HaLow meshing. This approach would be beneficial in wide area searches where ground teams operate in small, widely separated clusters, and where maintaining a continuous multi UAV mesh across the entire region would be impractical.

Alternatively, investigating full duplex receivers would allow nodes to simultaneous transmit and receive data, substantially reducing the throughput loss at each relay hop. This system would also allow the optimiser to use RSSI as an objective, rather than throughput. This would avoid the need for MCS throughput modelling as used in the current model and improve overall accuracy. While Australia's narrow HaLow bandwidth limits practical full duplex use today, wider allocations in other regions or future hardware improvements may make this approach feasible.

Further work is also needed on autonomous FANET behaviour, including automatic repositioning, battery aware handover and self healing of relay chains as UAVs rotate out for recharging. This would be critical to achieving the up time required for SAR operations and proving the feasibility of a FANET solution.

Finally, additional optimisation objectives such as fleet size could be introduced help identify the minimum number of UAVs required for a given mission. For visualisation, region wide throughput heat maps could be used to provide additional location analysis to first responders.

Overall, the results in this thesis show that Wi-Fi HaLow equipped UAVs form a promising foundation for rapidly deployable communication in SAR operations. With further validation and continued refinement of the optimisation framework, these systems could provide robust and flexible communication support across a wide range of terrain constrained scenarios.

Acknowledgments

I would like to thank my supervisor, James Stevens, for his guidance and support throughout this project. His advice shaped both the experimental work and the modelling, and he was instrumental in planning and running the G2A tests.

I am also grateful to Lyall Beveridge for sharing his extensive knowledge of the HaLow kits, for showing me around the Morse Micro office, and for providing many practical tips that made configuration and field measurements far smoother. An additional thanks to Morse Micro for supplying the HaLow test kits used throughout this work.

Thank you Mitchell Torok for providing drone access, flying the platform, and helping set up safe and reliable G2A tests. His involvement made the aerial measurements possible and greatly strengthened scope of this thesis.

I would like to acknowledge Siddh Rawal and Vincent Ho for their knowledge handover from their own HaLow thesis projects and for their help in getting the kits configured and operating correctly, and to Liam for assisting with the G2G measurements at Long Reef.

Finally, thank you to everyone who offered their time, advice, and encouragement along the way.

References

- [1] United Nations Office for Disarmament Affairs. *Human Cost of Disasters: An Overview of the Last 20 Years 2000-2019*. en. United Nations, Nov. 2020. ISBN: 978-92-1-005447-8. DOI: 10.18356/79b92774-en. URL: <https://www.un-ilibrary.org/content/books/9789210054478> (visited on 03/26/2025).
- [2] Dr Agrawal and Dr Monit Kapoor. “A comparative study of mobility models for flying ad hoc networks”. In: *International Journal of Sensor Networks* 38 (Jan. 2022), p. 204. DOI: 10.1504/IJSNET.2022.121709.
- [3] Moses Alabi. “Telecommunications and Wireless Networks for Disaster Response and Recovery”. In: (Dec. 2023).
- [4] Tejasvi Alladi et al. “SecAuthUAV: A Novel Authentication Scheme for UAV-Ground Station and UAV-UAV Communication”. In: *IEEE Transactions on Vehicular Technology* 69.12 (Dec. 2020), pp. 15068–15077. ISSN: 1939-9359. DOI: 10.1109/TVT.2020.3033060. URL: <https://ieeexplore.ieee.org/document/9237145> (visited on 04/10/2025).
- [5] Riham Altawy and Amr M. Youssef. “Security, Privacy, and Safety Aspects of Civilian Drones: A Survey”. In: *ACM Trans. Cyber-Phys. Syst.* 1.2 (Nov. 2016), 7:1–7:25. ISSN: 2378-962X. DOI: 10.1145/3001836. URL: <https://doi.org/10.1145/3001836> (visited on 04/10/2025).

- [6] Mohamed Alzenad et al. “3-D Placement of an Unmanned Aerial Vehicle Base Station (UAV-BS) for Energy-Efficient Maximal Coverage”. In: *IEEE Wireless Communications Letters* 6.4 (Aug. 2017), pp. 434–437. ISSN: 2162-2345. DOI: 10.1109/LWC.2017.2700840. URL: <https://ieeexplore.ieee.org/document/7918510> (visited on 04/10/2025).
- [7] Mahdi Asadpour et al. “Routing in a fleet of micro aerial vehicles: first experimental insights”. In: *Proceedings of the third ACM workshop on Airborne networks and communications*. AIRBORNE ’14. New York, NY, USA: Association for Computing Machinery, Aug. 2014, pp. 9–10. ISBN: 978-1-4503-2985-9. DOI: 10.1145/2636582.2636832. URL: <https://doi.org/10.1145/2636582.2636832> (visited on 04/26/2025).
- [8] Nils Aschenbruck et al. “Modelling mobility in disaster area scenarios”. In: *Proceedings of the 10th ACM Symposium on Modeling, analysis, and simulation of wireless and mobile systems*. MSWiM ’07. New York, NY, USA: Association for Computing Machinery, Oct. 2007, pp. 4–12. ISBN: 978-1-59593-851-0. DOI: 10.1145/1298126.1298131. URL: <https://doi.org/10.1145/1298126.1298131> (visited on 04/09/2025).
- [9] Aloÿs Augustin et al. “A Study of LoRa: Long Range & Low Power Networks for the Internet of Things”. en. In: *Sensors* 16.9 (Sept. 2016). Number: 9 Publisher: Multidisciplinary Digital Publishing Institute, p. 1466. ISSN: 1424-8220. DOI: 10.3390/s16091466. URL: <https://www.mdpi.com/1424-8220/16/9/1466> (visited on 03/16/2025).
- [10] Cherry Ye Aung, Ivan Wang-Hei Ho, and Peter Han Joo Chong. “Store-Carry-Cooperative Forward Routing With Information Epidemics Control for Data Delivery in Opportunistic Networks”. In: *IEEE Access* 5 (2017), pp. 6608–6625. ISSN: 2169-3536. DOI: 10.1109/ACCESS.2017.2690341. URL: <https://ieeexplore.ieee.org/document/7891962> (visited on 04/27/2025).
- [11] Australian Communications and Media Authority. *Communications report 2017–18 — ACMA*. en. Publisher: Australian Communications and Media Authority. URL: <https://www.acma.gov.au/publications/2019-02/report/communications-report-2017-18> (visited on 04/14/2025).
- [12] Muhammad Mukarram Bin Tariq, Mostafa Ammar, and Ellen Zegura. “Message ferry route design for sparse ad hoc networks with mobile nodes”. In: *Proceedings of the 7th ACM international symposium on Mobile ad hoc networking and computing*. MobiHoc ’06. New York, NY, USA: Association for Computing Machinery, May 2006, pp. 37–48. ISBN: 978-1-59593-368-3. DOI: 10.1145/1132905.1132910. URL: <https://doi.org/10.1145/1132905.1132910> (visited on 04/26/2025).
- [13] Paul Bupe, Rami Haddad, and Fernando Rios-Gutierrez. “Relief and emergency communication network based on an autonomous decentralized UAV clustering network”. In: *SoutheastCon 2015*. ISSN: 1558-058X. Apr. 2015, pp. 1–8. DOI: 10.1109/SECON.2015.7133027. URL: <https://ieeexplore.ieee.org/document/7133027> (visited on 04/07/2025).

- [14] Christelle Caillouet and Tahiry Razafindralambo. “Efficient deployment of connected unmanned aerial vehicles for optimal target coverage”. In: *2017 Global Information Infrastructure and Networking Symposium (GIIS)*. ISSN: 2150-329X. Oct. 2017, pp. 1–8. DOI: 10.1109/GIIS.2017.8169803. URL: <https://ieeexplore.ieee.org/document/8169803> (visited on 04/10/2025).
- [15] Seyit Alperen CELTEK, Akif DURDU, and Ender KURNAZ. “Design and Simulation of the Hierarchical Tree Topology Based Wireless Drone Networks”. In: *2018 International Conference on Artificial Intelligence and Data Processing (IDAP)*. Sept. 2018, pp. 1–5. DOI: 10.1109/IDAP.2018.8620755. URL: <https://ieeexplore.ieee.org/document/8620755> (visited on 04/07/2025).
- [16] Indu Chandran and Kizheppatt Vipin. “Multi-UAV Networks for Disaster Monitoring: Challenges and Opportunities from a Network Perspective”. en. In: *SN Computer Science* 5.5 (May 2024), p. 519. ISSN: 2661-8907. DOI: 10.1007/s42979-024-02788-3. URL: <https://doi.org/10.1007/s42979-024-02788-3> (visited on 03/10/2025).
- [17] Ing-Chau Chang, Chi-Sheng Liao, and Chin-En Yen. “The Energy-Aware Multi-UAV Dispatch and Handoff Algorithm for Maximizing the Event Communication Time in Disasters”. In: *Applied Sciences* 11 (Jan. 2021), p. 1054. DOI: 10.3390/app11031054.
- [18] Hao Chen et al. “Formation flight of fixed-wing UAV swarms: A group-based hierarchical approach”. In: *Chinese Journal of Aeronautics* 34.2 (Feb. 2021), pp. 504–515. ISSN: 1000-9361. DOI: 10.1016/j.cja.2020.03.006. URL: <https://www.sciencedirect.com/science/article/pii/S1000936120301205> (visited on 04/07/2025).
- [19] Gaurav Choudhary et al. “Intrusion Detection Systems for Networked Unmanned Aerial Vehicles: A Survey”. In: *2018 14th International Wireless Communications & Mobile Computing Conference (IWCMC)*. ISSN: 2376-6506. June 2018, pp. 560–565. DOI: 10.1109/IWCMC.2018.8450305. URL: <https://ieeexplore.ieee.org/document/8450305> (visited on 04/10/2025).
- [20] Luís Conceição and Marilia Curado. “Modelling Mobility Based on Human Behaviour in Disaster Areas”. en. In: *Wired/Wireless Internet Communication*. Ed. by Vassilis Tsaoussidis et al. Berlin, Heidelberg: Springer, 2013, pp. 56–69. ISBN: 978-3-642-38401-1. DOI: 10.1007/978-3-642-38401-1_5.
- [21] Yanpeng Cui et al. “Topology-Aware Resilient Routing Protocol for FANETs: An Adaptive Q-Learning Approach”. In: *IEEE Internet of Things Journal* 9.19 (Oct. 2022). arXiv:2306.17360 [cs], pp. 18632–18649. ISSN: 2327-4662, 2372-2541. DOI: 10.1109/JIOT.2022.3162849. URL: <http://arxiv.org/abs/2306.17360> (visited on 04/27/2025).
- [22] Magda Dabrowska. *Vodafone and AST SpaceMobile sign 10-year deal for space-based connectivity*. en-GB. Dec. 2024. URL: <https://www.vanillaplus.com/2024/12/10/88039-vodafone-and-ast-spacemobile-sign-10-year-deal-for-space-based-connectivity/> (visited on 03/31/2025).

- [23] David Daly. *How Advanced Communication Systems Aid Search and Rescue Missions - Base Camp Connect*. Jan. 2025. URL: https://basecampconnect.com/how-advanced-communication-systems-aid-search-and-rescue-missions/?utm_source=chatgpt.com (visited on 03/26/2025).
- [24] Dandelions. *Air Deployed IOT Solutions*. URL: <https://www.dandelions.cloud/products/air-deployed-iot-solutions> (visited on 04/03/2025).
- [25] Dandelions. *Latest Technologies To Prevent and Fight Bushfires - February 2020*. URL: <https://www.dandelions.cloud/news/latest-technologies-to-prevent-and-fight-bushfires> (visited on 04/03/2025).
- [26] Dandelions. *What You Could Fit In The Gyrochute: GPS*. URL: <https://www.dandelions.cloud/news/what-you-could-fit-in-the-gyrochute-gps> (visited on 04/03/2025).
- [27] K. Deb et al. “A fast and elitist multiobjective genetic algorithm: NSGA-II”. In: *IEEE Transactions on Evolutionary Computation* 6.2 (Apr. 2002), pp. 182–197. ISSN: 1941-0026. DOI: 10.1109/4235.996017. URL: <https://ieeexplore.ieee.org/document/996017> (visited on 11/19/2025).
- [28] Premier’s Department. “New technology to help communities stay connected following disasters — NSW Government”. en-AU. In: (Sept. 2024). Last Modified: 2024-09-20 Publisher: NSW Government. URL: <https://www.nsw.gov.au/media-releases/new-technology-to-help-communities-stay-connected-following-disasters> (visited on 03/27/2025).
- [29] Shopan Dey et al. “Ad-hoc networked UAVs as Aerial Mesh Network for disaster management application and remote sensing: An approach”. In: *2017 8th IEEE Annual Information Technology, Electronics and Mobile Communication Conference (IEMCON)*. Oct. 2017, pp. 301–304. DOI: 10.1109/IEMCON.2017.8117231. URL: <https://ieeexplore.ieee.org/document/8117231> (visited on 04/07/2025).
- [30] Chao Dong et al. “Optimal deployment density for maximum coverage of drone small cells”. In: *China Communications* 15.5 (May 2018), pp. 25–40. ISSN: 1673-5447. DOI: 10.1109/CC.2018.8387984. URL: <https://ieeexplore.ieee.org/document/8387984> (visited on 04/10/2025).
- [31] Zhaoyang Du et al. “A Routing Protocol for UAV-Assisted Vehicular Delay Tolerant Networks”. English. In: *IEEE Open Journal of the Computer Society* 2.01 (Jan. 2021). Publisher: IEEE Computer Society, pp. 85–98. ISSN: 2644-1268. DOI: 10.1109/OJCS.2021.3054759. URL: <https://www.computer.org/csdl/journal/oj/2021/01/09336218/1qHL9i2msYo> (visited on 04/27/2025).
- [32] Omid Esrafilian, Rajeev Gangula, and David Gesbert. “Autonomous UAV-aided Mesh Wireless Networks”. In: *IEEE INFOCOM 2020 - IEEE Conference on Computer Communications Workshops (INFOCOM WKSHPS)*. July 2020, pp. 634–640. DOI: 10.1109/INFOCOMWKSHPS50562.2020.9162753. URL: <https://ieeexplore.ieee.org/document/9162753> (visited on 04/07/2025).
- [33] *FireMapper by Fire Front Solutions*. en-AU. URL: <https://www.firemapper.app> (visited on 03/26/2025).

- [34] Siddarth Ganesh, Vaishnavi Gopalasamy, and N B Sai Shibu. “Architecture for Drone Assisted Emergency Ad-hoc Network for Disaster Rescue Operations”. In: *2021 International Conference on COMmunication Systems & NETworkS (COMSNETS)*. ISSN: 2155-2509. Jan. 2021, pp. 44–49. DOI: 10.1109/COMSNETS51098.2021.9352814. URL: <https://ieeexplore.ieee.org/document/9352814> (visited on 04/07/2025).
- [35] Yixin Gu et al. “Airborne WiFi networks through directional antennae: An experimental study”. In: *2015 IEEE Wireless Communications and Networking Conference (WCNC)*. ISSN: 1558-2612. Mar. 2015, pp. 1314–1319. DOI: 10.1109/WCNC.2015.7127659. URL: <https://ieeexplore.ieee.org/document/7127659> (visited on 03/16/2025).
- [36] Manali Gupta and Shirshu Varma. “Optimal placement of UAVs of an aerial mesh network in an emergency situation”. en. In: *Journal of Ambient Intelligence and Humanized Computing* 12.1 (Jan. 2021), pp. 343–358. ISSN: 1868-5145. DOI: 10.1007/s12652-020-01976-2. URL: <https://doi.org/10.1007/s12652-020-01976-2> (visited on 04/10/2025).
- [37] Daniel Halperin et al. *Predictable 802.11 Packet Delivery from Wireless Channel Measurements*. Vol. 40. Journal Abbreviation: Computer Communication Review - CCR Pages: 170 Publication Title: Computer Communication Review - CCR. Aug. 2010. DOI: 10.1145/1851275.1851203.
- [38] Simon Heron. “Advanced Encryption Standard (AES)”. In: *Network Security* 2009.12 (Dec. 2009), pp. 8–12. ISSN: 1353-4858. DOI: 10.1016/S1353-4858(10)70006-4. URL: <https://www.sciencedirect.com/science/article/pii/S1353485810700064> (visited on 04/10/2025).
- [39] Akram Al-Hourani, Sithamparanathan Kandeepan, and Simon Lardner. “Optimal LAP Altitude for Maximum Coverage”. In: *IEEE Wireless Communications Letters* 3.6 (Dec. 2014), pp. 569–572. ISSN: 2162-2345. DOI: 10.1109/LWC.2014.2342736. URL: <https://ieeexplore.ieee.org/document/6863654> (visited on 04/10/2025).
- [40] Md. Nurul Huda et al. “An approach for short message resilience in disaster-stricken areas”. In: *The International Conference on Information Network 2012*. ISSN: 2332-5658. Feb. 2012, pp. 120–125. DOI: 10.1109/ICOIN.2012.6164362. URL: <https://ieeexplore.ieee.org/document/6164362> (visited on 04/27/2025).
- [41] Jeremy Hyatt. *Pushing the limits: Wi-Fi HaLow Testing in Joshua Tree National Park*. en-US. Sept. 2024. URL: <https://www.morsemicro.com/2024/09/09/pushing-the-limits-wi-fi-hallow-testing-in-joshua-tree-national-park/> (visited on 03/17/2025).
- [42] ICSM. *Elvis - Elevation and Depth - Foundation Spatial Data*. en. Apr. 2025. URL: <https://elevation.fsdf.org.au/> (visited on 07/31/2025).
- [43] “IEEE Standard for Information technology—Telecommunications and information exchange between systems - Local and metropolitan area networks—Specific requirements - Part 11: Wireless LAN Medium Access Control (MAC) and Physical Layer (PHY) Specifications Amendment 2: Sub 1 GHz License Exempt Operation”. In: *IEEE Std 802.11ah-2016 (Amendment to IEEE Std 802.11-2016, as amended by IEEE Std*

- 802.11ai-2016) (May 2017), pp. 1–594. DOI: 10.1109/IEEEESTD.2017.7920364. URL: <https://ieeexplore.ieee.org/document/7920364> (visited on 11/19/2025).
- [44] *ITU-R P.526-15: Propagation by diffraction*. Tech. rep. International Telecommunication Union, Radiocommunication Sector, 2019. URL: <https://www.itu.int/rec/R-REC-P.526/en>.
- [45] Abhishek Joshi et al. “Simulation of Multi-UAV Ad-Hoc Network for Disaster Monitoring Applications”. In: *2020 International Conference on Information Networking (ICOIN)*. ISSN: 1976-7684. Jan. 2020, pp. 690–695. DOI: 10.1109/ICOIN48656.2020.9016543. URL: <https://ieeexplore.ieee.org/document/9016543> (visited on 04/07/2025).
- [46] Regina Lambin et al. “From Challenges to Solutions: Stakeholder Roles in Disaster Relief Operations”. In: *International Journal of Research and Innovation in Social Science* VIII (Sept. 2024), pp. 3788–3803. DOI: 10.47772/IJRRISS.2024.8080282.
- [47] Jialiuyuan Li et al. *Energy-Efficient UAV Swarm Assisted MEC with Dynamic Clustering and Scheduling*. arXiv:2402.18936 [cs]. Feb. 2024. DOI: 10.48550/arXiv.2402.18936. URL: <http://arxiv.org/abs/2402.18936> (visited on 04/10/2025).
- [48] Chi Harold Liu et al. “Distributed Energy-Efficient Multi-UAV Navigation for Long-Term Communication Coverage by Deep Reinforcement Learning”. In: *IEEE Transactions on Mobile Computing* 19.6 (June 2020), pp. 1274–1285. ISSN: 1558-0660. DOI: 10.1109/TMC.2019.2908171. URL: <https://ieeexplore.ieee.org/document/8676325> (visited on 04/10/2025).
- [49] Jiangbin Lyu et al. “Placement Optimization of UAV-Mounted Mobile Base Stations”. In: *IEEE Communications Letters* 21.3 (Mar. 2017), pp. 604–607. ISSN: 1558-2558. DOI: 10.1109/LCOMM.2016.2633248. URL: <https://ieeexplore.ieee.org/document/7762053> (visited on 04/10/2025).
- [50] Rooha Masroor, Muhammad Naeem, and Waleed Ejaz. “Efficient deployment of UAVs for disaster management: A multi-criterion optimization approach”. In: *Computer Communications* 177 (Sept. 2021), pp. 185–194. ISSN: 0140-3664. DOI: 10.1016/j.comcom.2021.07.006. URL: <https://www.sciencedirect.com/science/article/pii/S0140366421002607> (visited on 04/10/2025).
- [51] Sébastien Maudet et al. “Practical evaluation of Wi-Fi HaLow performance”. In: *Internet of Things* 24 (Dec. 2023), p. 100957. ISSN: 2542-6605. DOI: 10.1016/j.iot.2023.100957. URL: <https://www.sciencedirect.com/science/article/pii/S2542660523002809> (visited on 11/19/2025).
- [52] Jake N. McRae et al. “Utilizing Drones to Restore and Maintain Radio Communication During Search and Rescue Operations”. In: *Wilderness & Environmental Medicine* 32.1 (Mar. 2021), pp. 41–46. ISSN: 1080-6032. DOI: 10.1016/j.wem.2020.11.002. URL: <https://www.sciencedirect.com/science/article/pii/S1080603220302076> (visited on 03/27/2025).

- [53] Mohamed-Ayoub Messous, Sidi-Mohammed Senouci, and Hichem Sedjelmaci. “Network connectivity and area coverage for UAV fleet mobility model with energy constraint”. In: *2016 IEEE Wireless Communications and Networking Conference*. ISSN: 1558-2612. Apr. 2016, pp. 1–6. DOI: 10.1109/WCNC.2016.7565125. URL: <https://ieeexplore.ieee.org/document/7565125> (visited on 04/10/2025).
- [54] Jize Mi and Zhitao Dai. “A 3D Smooth Mobility Model Based on Semi-random Circular Movement for FANETs”. In: *2021 7th International Conference on Computer and Communications (ICCC)*. Dec. 2021, pp. 954–959. DOI: 10.1109/ICCC54389.2021.9674424. URL: <https://ieeexplore.ieee.org/document/9674424> (visited on 04/10/2025).
- [55] Morse Micro. *End Products*. en-US. URL: <https://www.morsemicro.com/end-products/> (visited on 04/14/2025).
- [56] Morse Micro. *Technology*. en-US. URL: <https://www.morsemicro.com/technology/> (visited on 03/17/2025).
- [57] Nemanja Miljković. *Challenges and Obstacles in the Use of Search and Rescue Dogs During Disaster Operations: A Case Study of the Earthquake in Turkey*. en. July 2024. DOI: 10.20944/preprints202407.1177.v1. URL: <https://www.preprints.org/manuscript/202407.1177/v1> (visited on 03/26/2025).
- [58] Simon Morgenthaler et al. “UAVNet: A mobile wireless mesh network using Unmanned Aerial Vehicles”. In: *2012 IEEE Globecom Workshops*. ISSN: 2166-0077. Dec. 2012, pp. 1603–1608. DOI: 10.1109/GLOCOMW.2012.6477825. URL: <https://ieeexplore.ieee.org/document/6477825> (visited on 04/25/2025).
- [59] Morse Micro. *3k Wi-Fi HaLow Shatters Limits with a 3-Kilometer Range*. Jan. 2024. URL: <https://www.youtube.com/watch?v=2x1UiJXuCoM> (visited on 04/11/2025).
- [60] Morse Micro. *Wi-Fi HaLow delivers throughput at 16km range*. Sept. 2024. URL: <https://www.youtube.com/watch?v=fBMgZah2Z7g> (visited on 03/17/2025).
- [61] MorseMicro. *HaLowLink1 - MM6108 Data Sheet*. en-US. Jan. 2025. URL: <https://www.morsemicro.com/chips/> (visited on 07/31/2025).
- [62] Mohammad Mozaffari et al. “Efficient Deployment of Multiple Unmanned Aerial Vehicles for Optimal Wireless Coverage”. In: *IEEE Communications Letters* 20.8 (Aug. 2016), pp. 1647–1650. ISSN: 1558-2558. DOI: 10.1109/LCOMM.2016.2578312. URL: <https://ieeexplore.ieee.org/document/7486987> (visited on 04/10/2025).
- [63] Wajeeha Nasar et al. “Improving search and rescue planning and resource allocation through case-based and concept-based retrieval”. In: *Journal of Intelligent Information Systems* 62 (June 2024), pp. 1431–1453. DOI: 10.1007/s10844-024-00861-0.
- [64] Parrot. *Australian Drone Regulations*. en. URL: <https://www.parrot.com/en/drone-regulations/australia> (visited on 04/10/2025).

- [65] Mansi Peer, Vivek Ashok Bohara, and Anand Srivastava. “Multi-UAV Placement Strategy for Disaster-Resilient Communication Network”. In: *2020 IEEE 92nd Vehicular Technology Conference (VTC2020-Fall)*. ISSN: 2577-2465. Nov. 2020, pp. 1–7. DOI: 10.1109/VTC2020-Fall149728. 2020.9348687. URL: <https://ieeexplore.ieee.org/document/9348687> (visited on 04/10/2025).
- [66] Stéphane Pomportes, Joanna Tomaszik, and Véronique Vèque. “A Composite Mobility Model for Ad Hoc Networks in Disaster Areas”. en. In: *REV Journal on Electronics and Communications* 1.1 (Apr. 2011). Number: 1. ISSN: 1859-378X. DOI: 10.21553/rev-jec.10. URL: <https://rev-jec.org/index.php/rev-jec/article/view/10> (visited on 04/10/2025).
- [67] Ayush Puri, Mohamed Elkharboutly, and Naseem Ameer Ali. “Identifying major challenges in managing post-disaster reconstruction projects: A critical analysis”. In: *International Journal of Disaster Risk Reduction* 107 (June 2024), p. 104491. ISSN: 2212-4209. DOI: 10.1016/j.ijdrr.2024.104491. URL: <https://www.sciencedirect.com/science/article/pii/S221242092400253X> (visited on 03/26/2025).
- [68] Carlos Osorio Quero and Jose Martinez-Carranza. “Unmanned aerial systems in search and rescue: A global perspective on current challenges and future applications”. In: *International Journal of Disaster Risk Reduction* 118 (Feb. 2025), p. 105199. ISSN: 2212-4209. DOI: 10.1016/j.ijdrr.2025.105199. URL: <https://www.sciencedirect.com/science/article/pii/S2212420925000238> (visited on 03/10/2025).
- [69] AMHERST Radio Hire. *Radio Repeater - Explained*. URL: <https://www.walkie-talkie-hire.co.uk/info/what-is-a-repeater> (visited on 03/27/2025).
- [70] Christian Raffelsberger and Hermann Hellwagner. “A hybrid MANET-DTN routing scheme for emergency response scenarios”. In: *2013 IEEE International Conference on Pervasive Computing and Communications Workshops (PERCOM Workshops)*. Mar. 2013, pp. 505–510. DOI: 10.1109/PerComW.2013.6529549. URL: <https://ieeexplore.ieee.org/document/6529549> (visited on 04/27/2025).
- [71] Hairani Maisarah Rahim, Chee Yen Leow, and Tharek Abd. Rahman. “Millimeter wave propagation through foliage: Comparison of models”. In: *2015 IEEE 12th Malaysia International Conference on Communications (MICC)*. Nov. 2015, pp. 236–240. DOI: 10.1109/MICC.2015.7725440. URL: <https://ieeexplore.ieee.org/document/7725440> (visited on 11/19/2025).
- [72] Zahra Rahimi et al. “An Efficient 3-D Positioning Approach to Minimize Required UAVs for IoT Network Coverage”. In: *IEEE Internet of Things Journal* 9.1 (Jan. 2022), pp. 558–571. ISSN: 2327-4662. DOI: 10.1109/JIOT.2021.3084521. URL: <https://ieeexplore.ieee.org/document/9442809> (visited on 04/10/2025).
- [73] Shanyao Ren et al. “HWMP-based secure communication of multi-agent systems”. In: *Ad Hoc Networks* 157 (Apr. 2024), p. 103456. ISSN: 1570-8705. DOI: 10.1016/j.adhoc.2024.103456. URL: <https://www.sciencedirect.com/science/article/pii/S1570870524000672> (visited on 04/27/2025).

- [74] Arnau Rovira-Sugranes et al. “A review of AI-enabled routing protocols for UAV networks: Trends, challenges, and future outlook”. In: *Ad Hoc Networks* 130 (May 2022), p. 102790. ISSN: 1570-8705. DOI: 10.1016/j.adhoc.2022.102790. URL: <https://www.sciencedirect.com/science/article/pii/S1570870522000087> (visited on 04/27/2025).
- [75] Sérgio Sabino, Nuno Horta, and António Grilo. “Centralized Unmanned Aerial Vehicle Mesh Network Placement Scheme: A Multi-Objective Evolutionary Algorithm Approach”. en. In: *Sensors* 18.12 (Dec. 2018). Number: 12 Publisher: Multidisciplinary Digital Publishing Institute, p. 4387. ISSN: 1424-8220. DOI: 10.3390/s18124387. URL: <https://www.mdpi.com/1424-8220/18/12/4387> (visited on 04/27/2025).
- [76] Elnaz Safapour, Sharareh Kermanshachi, and Apurva Pamidimukkala. “Post-disaster recovery in urban and rural communities: Challenges and strategies”. In: *International Journal of Disaster Risk Reduction* 64 (Oct. 2021), p. 102535. ISSN: 2212-4209. DOI: 10.1016/j.ijdrr.2021.102535. URL: <https://www.sciencedirect.com/science/article/pii/S2212420921004969> (visited on 03/26/2025).
- [77] Ozgur Koray Sahingoz. “Networking Models in Flying Ad-Hoc Networks (FANETs): Concepts and Challenges”. en. In: *Journal of Intelligent & Robotic Systems* 74.1 (Apr. 2014), pp. 513–527. ISSN: 1573-0409. DOI: 10.1007/s10846-013-9959-7. URL: <https://doi.org/10.1007/s10846-013-9959-7> (visited on 04/10/2025).
- [78] Victor Sanchez-Aguero et al. “Energy-Aware Management in Multi-UAV Deployments: Modelling and Strategies”. In: *Sensors (Basel, Switzerland)* 20.10 (May 2020), p. 2791. ISSN: 1424-8220. DOI: 10.3390/s20102791. URL: <https://www.ncbi.nlm.nih.gov/pmc/articles/PMC7284756/> (visited on 04/10/2025).
- [79] Arslan Shafique, Abid Mehmood, and Mourad Elhadef. “Survey of Security Protocols and Vulnerabilities in Unmanned Aerial Vehicles”. In: *IEEE Access* 9 (2021), pp. 46927–46948. ISSN: 2169-3536. DOI: 10.1109/ACCESS.2021.3066778. URL: <https://ieeexplore.ieee.org/document/9380688> (visited on 04/10/2025).
- [80] Vishal Sharma et al. “LoRaWAN-Based Energy-Efficient Surveillance by Drones for Intelligent Transportation Systems”. en. In: *Energies* 11.3 (Mar. 2018). Number: 3 Publisher: Multidisciplinary Digital Publishing Institute, p. 573. ISSN: 1996-1073. DOI: 10.3390/en11030573. URL: <https://www.mdpi.com/1996-1073/11/3/573> (visited on 04/11/2025).
- [81] Liping Shi, Néstor J. Hernández Marcano, and Rune Hylsberg Jacobsen. “A review on communication protocols for autonomous unmanned aerial vehicles for inspection application”. In: *Microprocessors and Microsystems* 86 (Oct. 2021), p. 104340. ISSN: 0141-9331. DOI: 10.1016/j.micpro.2021.104340. URL: <https://www.sciencedirect.com/science/article/pii/S014193312100497X> (visited on 04/27/2025).
- [82] Benjamin Sliwa et al. *PARRoT: Predictive Ad-hoc Routing Fueled by Reinforcement Learning and Trajectory Knowledge*. arXiv:2012.05490 [cs]. Dec. 2020. DOI: 10.48550/arXiv.2012.05490. URL: <http://arxiv.org/abs/2012.05490> (visited on 04/27/2025).

- [83] AST SpaceMobile. *Direct Connection*. en-US. URL: <https://ast-science.com/spacemobile-network/direct-connection/> (visited on 03/31/2025).
- [84] *SpaceMobile Network*. en-US. URL: <https://ast-science.com/spacemobile-network/> (visited on 03/27/2025).
- [85] Starlink Starlink. *Starlink*. en. URL: <https://www.starlink.com/> (visited on 03/30/2025).
- [86] Marco Stellin, Sérgio Sabino, and António Grilo. “LoRaWAN Networking in Mobile Scenarios Using a WiFi Mesh of UAV Gateways”. en. In: *Electronics* 9.4 (Apr. 2020). Number: 4 Publisher: Multidisciplinary Digital Publishing Institute, p. 630. ISSN: 2079-9292. DOI: 10.3390/electronics9040630. URL: <https://www.mdpi.com/2079-9292/9/4/630> (visited on 04/27/2025).
- [87] Sujunjie Sun et al. “Optimizing Multi-UAV Deployment in 3-D Space to Minimize Task Completion Time in UAV-Enabled Mobile Edge Computing Systems”. In: *IEEE Communications Letters* 25.2 (Feb. 2021), pp. 579–583. ISSN: 1558-2558. DOI: 10.1109/LCOMM.2020.3029144. URL: <https://ieeexplore.ieee.org/document/9214892> (visited on 04/10/2025).
- [88] Morse Micro Engineering Team. *Personal communication regarding Wi-Fi HaLow foliage propagation tests*. English. morse2025personal. Sept. 2025.
- [89] Li Teng et al. “Lightweight Security Authentication Mechanism Towards UAV Networks”. In: *2019 International Conference on Networking and Network Applications (NaNA)*. Oct. 2019, pp. 379–384. DOI: 10.1109/NaNA.2019.90072. URL: <https://ieeexplore.ieee.org/document/9027572> (visited on 04/10/2025).
- [90] Le Tian. “(PDF) Wi-Fi HaLow for the Internet of Things: An up-to-date survey on IEEE 802.11ah research”. en. In: *ResearchGate* (Oct. 2024). DOI: 10.1016/j.jnca.2021.103036. URL: https://www.researchgate.net/publication/350047434_Wi-Fi_HaLow_for_the_Internet_of_Things_An_up-to-date_survey_on_IEEE_80211ah_research (visited on 03/24/2025).
- [91] Na Wang et al. “UAV 3D Mobility Model Oriented to Dynamic and Uncertain Environment”. en. In: *Algorithms and Architectures for Parallel Processing*. Ed. by Jaideep Vaidya and Jin Li. Cham: Springer International Publishing, 2018, pp. 640–650. ISBN: 978-3-030-05057-3. DOI: 10.1007/978-3-030-05057-3_48.
- [92] Qian Wang et al. “An Overview of Emergency Communication Networks”. en. In: *Remote Sensing* 15.6 (Jan. 2023). Number: 6 Publisher: Multidisciplinary Digital Publishing Institute, p. 1595. ISSN: 2072-4292. DOI: 10.3390/rs15061595. URL: <https://www.mdpi.com/2072-4292/15/6/1595> (visited on 03/26/2025).
- [93] Wei Wang et al. “A novel mobility model based on semi-random circular movement in mobile ad hoc networks”. In: *Information Sciences* 180.3 (Feb. 2010), pp. 399–413. ISSN: 0020-0255. DOI: 10.1016/j.ins.2009.10.001. URL: <https://www.sciencedirect.com/science/article/pii/S0020025509004265> (visited on 04/10/2025).

- [94] Yuntao Wang et al. “A Secure and Intelligent Data Sharing Scheme for UAV-Assisted Disaster Rescue”. In: *IEEE/ACM Transactions on Networking* 31.6 (Dec. 2023), pp. 2422–2438. ISSN: 1558-2566. DOI: 10.1109/TNET.2022.3226458. URL: <https://ieeexplore.ieee.org/document/10106022> (visited on 04/10/2025).
- [95] Gordon H. Worley. “Wilderness Communications”. en. In: *Wilderness & Environmental Medicine* 22.3 (Sept. 2011), pp. 262–269. ISSN: 1080-6032, 1545-1534. DOI: 10.1016/j.wem.2011.05.001. URL: <https://journals.sagepub.com/doi/10.1016/j.wem.2011.05.001> (visited on 03/27/2025).
- [96] Yuanhao Yang et al. “Energy-efficient data routing in cooperative UAV swarms for medical assistance after a disaster”. In: *Chaos: An Interdisciplinary Journal of Non-linear Science* 29.6 (June 2019), p. 063106. ISSN: 1054-1500. DOI: 10.1063/1.5092740. URL: <https://doi.org/10.1063/1.5092740> (visited on 04/27/2025).
- [97] Zebo Yang et al. “Factors Affecting the Performance of Sub-1 GHz IoT Wireless Networks”. en. In: *Wireless Communications and Mobile Computing* 2021.1 (Jan. 2021). Ed. by Pietro Manzoni, p. 8870222. ISSN: 1530-8669, 1530-8677. DOI: 10.1155/2021/8870222. URL: <https://onlinelibrary.wiley.com/doi/10.1155/2021/8870222> (visited on 03/16/2025).
- [98] Muneer Bani Yassein and “Nour Alhuda” Damer. “Flying Ad-Hoc Networks: Routing Protocols, Mobility Models, Issues”. en. In: *International Journal of Advanced Computer Science and Applications (ijacsa)* 7.6 (2016). Number: 6 Publisher: The Science and Information (SAI) Organization Limited. ISSN: 2156-5570. DOI: 10.14569/IJACSA.2016.070621. URL: <https://thesai.org/Publications/ViewPaper?Volume=7&Issue=6&Code=ijacsa&SerialNo=21> (visited on 04/10/2025).
- [99] Haitao Zhao et al. “Deployment Algorithms for UAV Airborne Networks Toward On-Demand Coverage”. In: *IEEE Journal on Selected Areas in Communications* 36.9 (Sept. 2018), pp. 2015–2031. ISSN: 1558-0008. DOI: 10.1109/JSAC.2018.2864376. URL: <https://ieeexplore.ieee.org/document/8432396> (visited on 04/10/2025).

6 Appendix

6.1 Raw Testing Results : Longreef

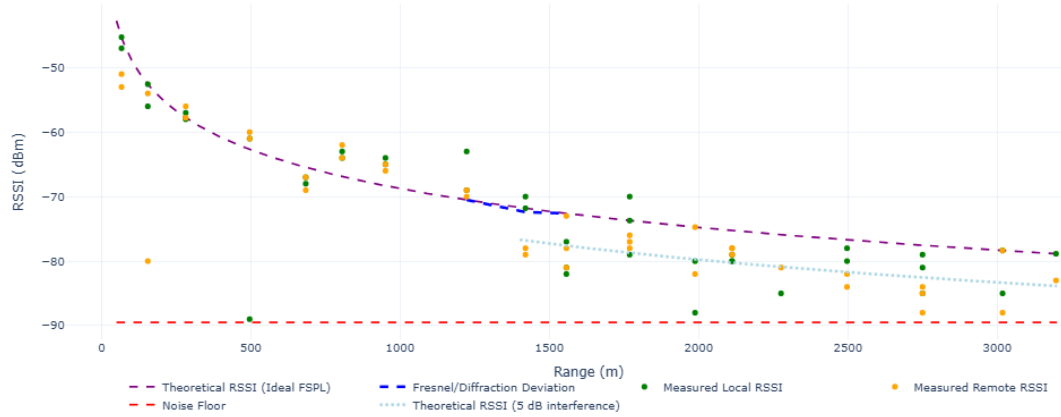


Figure 45: Long Reef G2G measurements: RSSI as a function of range.

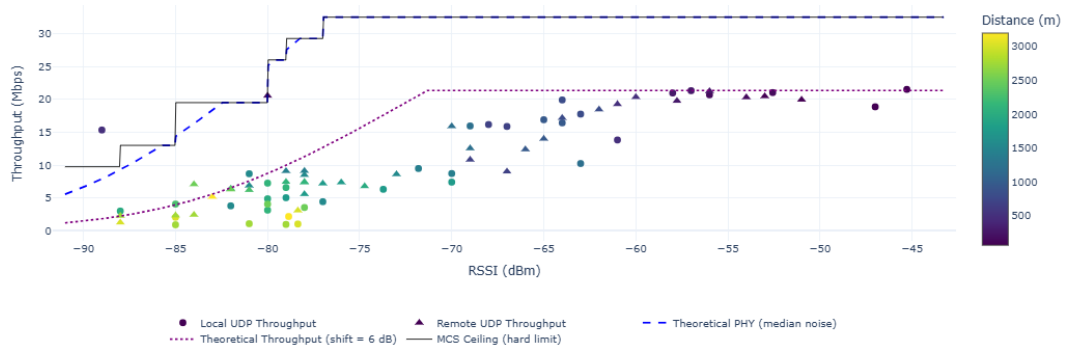


Figure 46: Long Reef G2G measurements: RSSI versus throughput.

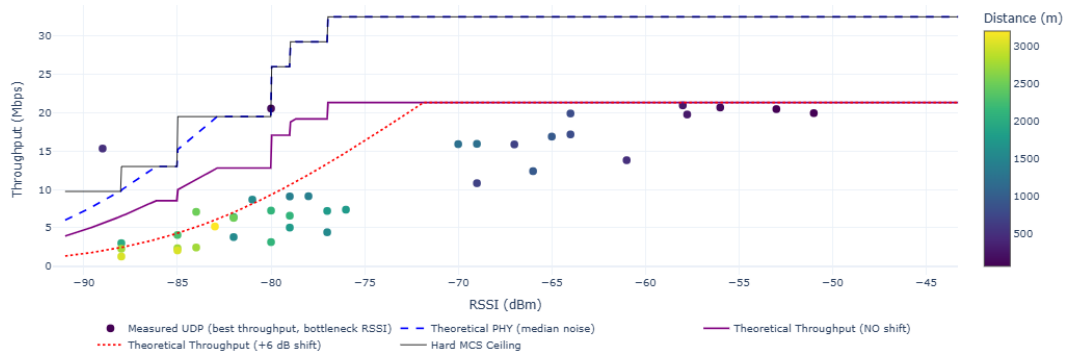


Figure 47: Long Reef G2G measurements: RSSI (bottleneck) versus throughput.

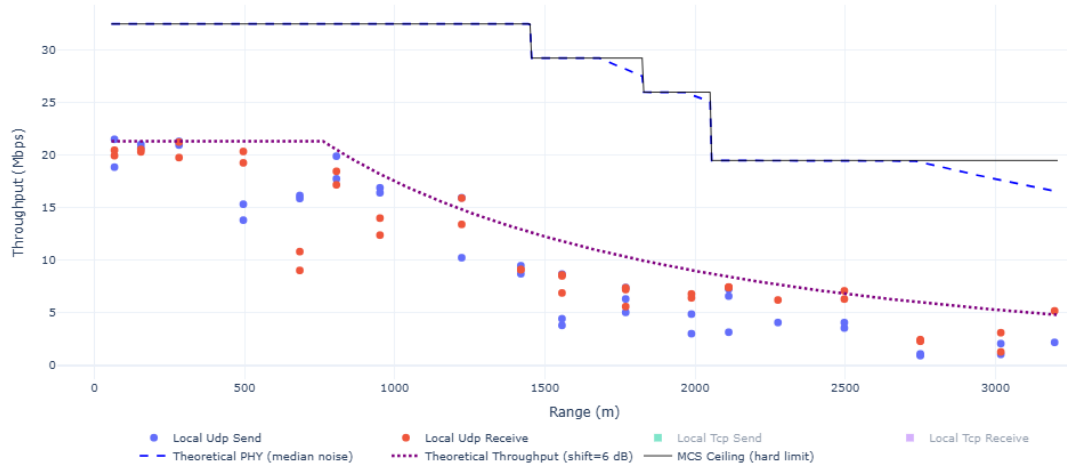


Figure 48: Long Reef G2G measurements: UDP Throughput as a function of range.

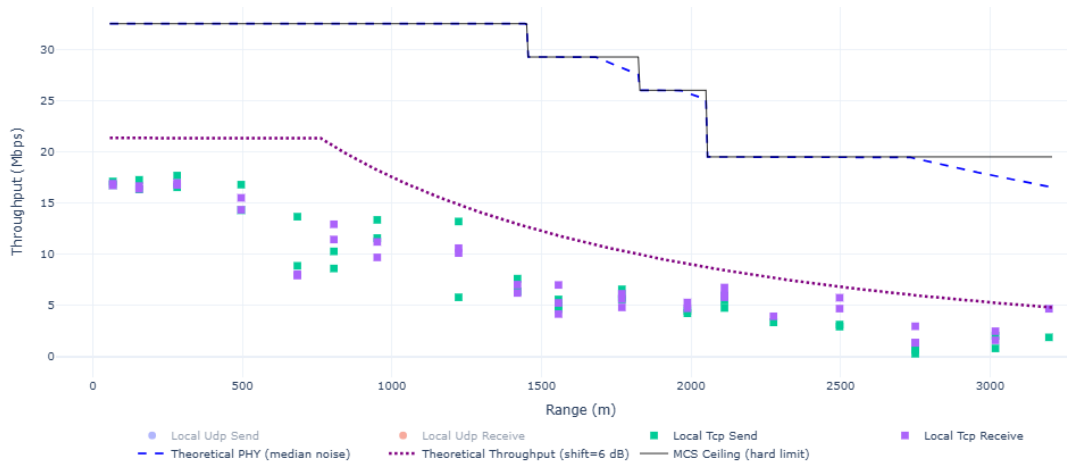


Figure 49: Long Reef G2G measurements: TCP Throughput as a function of range.

6.2 Raw Testing Results : Centennial

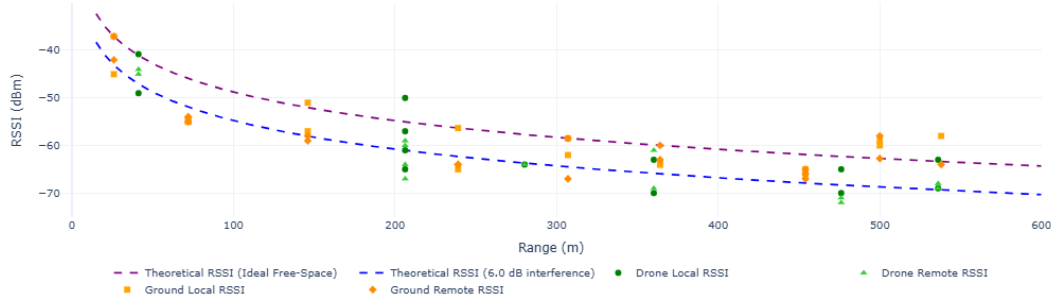


Figure 50: Centennial Park G2A and G2G comparison: RSSI as a function of range.

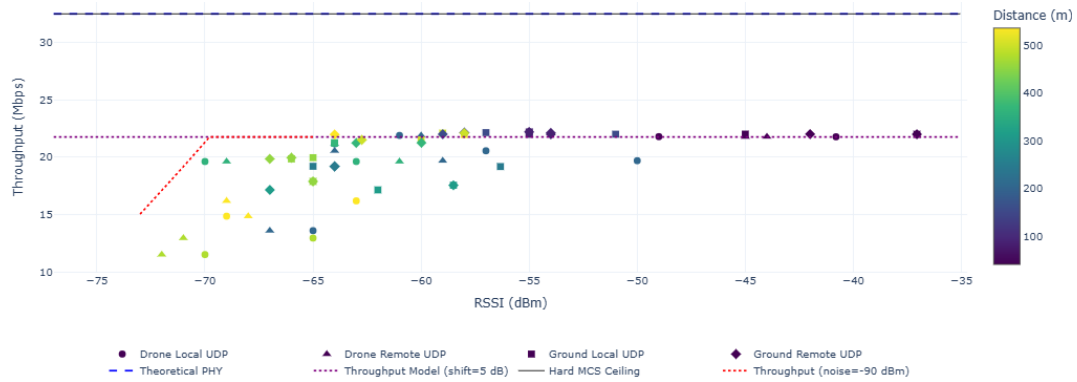


Figure 51: Centennial Park G2A and G2G comparison: RSSI versus throughput.

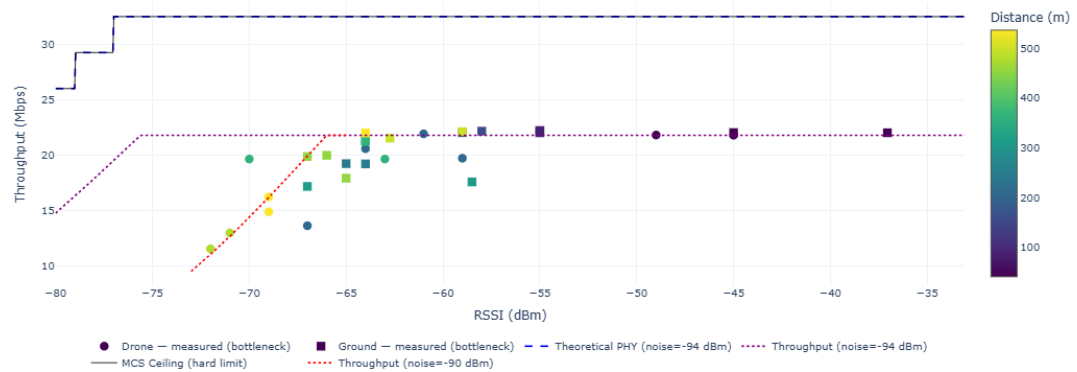


Figure 52: Centennial Park G2A and G2G comparison: RSSI (bottleneck) versus throughput

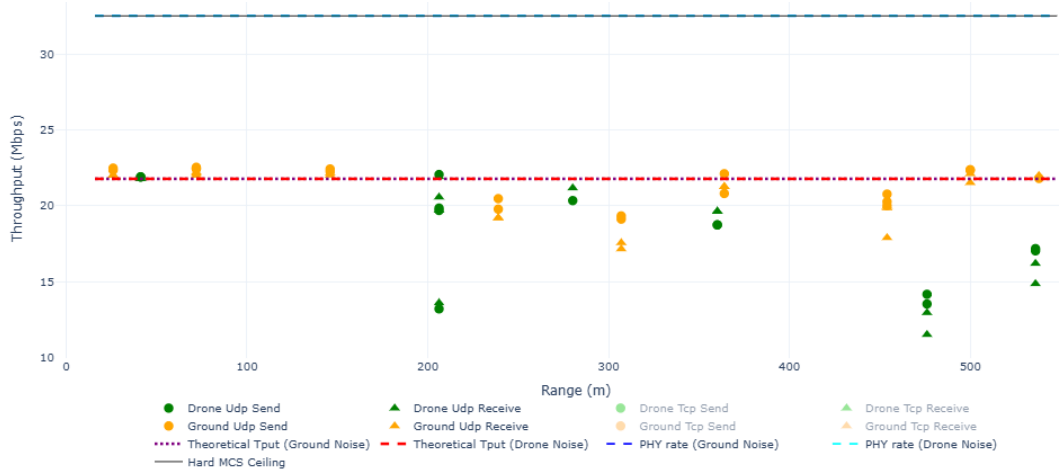


Figure 53: Centennial Park G2A and G2G comparison: UDP Throughput as a function of range .

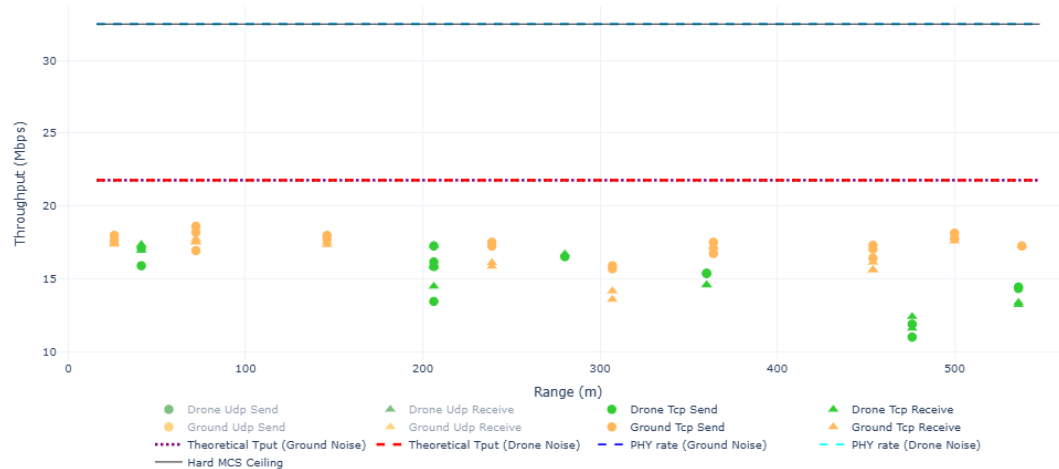


Figure 54: Centennial Park G2A and G2G comparison: TCP Throughput as a function of range .